To the Graduate Council:
I am submitting herewith a thesis written by Forrest J. Mobley entitled "Analysis of Turbulent Flow Behavior in Helicopter Rotor Hub Wake Predictions." I have examined the final paper copy of this thesis for form and content and recommend that it be accepted in partial fulfillment of the requirements for the degree of Master of Science, with a major in Aerospace Engineering.

James G. Coder, Major Professor

We have read this thesis
and recommend its acceptance:

Andrew K. Dickerson

Devina P. Sanjaya

Accepted for the Council:

Dixie Thompson

Vice Provost and Dean of the Graduate School

To the Graduate Council:
I am submitting herewith a thesis written by Forrest J. Mobley entitled "Analysis of Turbulent Flow Behavior in Helicopter Rotor Hub Wake Predictions." I have examined the final electronic copy of this thesis for form and content and recommend that it be accepted in partial fulfillment of the requirements for the degree of Master of Science, with a major in Aerospace Engineering.

James G. Coder, Major Professor

We have read this thesis
and recommend its acceptance:

Andrew K. Dickerson

Devina P. Sanjaya

Accepted for the Council:

Dixie Thompson

Vice Provost and Dean of the Graduate School

(Original signatures are on file with official student records.)

Analysis of Turbulent Flow Behavior in Helicopter Rotor Hub Wake Predictions

A Thesis Presented for the

Master of Science

Degree

The University of Tennessee, Knoxville

Forrest J. Mobley

August 2022

© by Forrest J. Mobley, 2022
All Rights Reserved.

To Geena, whose unceasing love and support gave me the motivation and determination to continue in my most difficult moments.

To my father who, through many experiences which could only be categorized under the third kind of fun, gave me the confidence to accomplish more.

To Dr. Shigeo Hayashibara, who gave me the opportunity that started this journey.

Acknowledgements

I would like to thank Dr. James Coder, Jared Carnes, and my other colleagues in the VolAIR lab for their willingness and patience to work with me and answer my questions. Their help with developing codes, using simulation software correctly, and understanding and interpreting results has been invaluable to the development of this document.

I would also like to thank Dr. Sven Schmitz, Charles Tierney, and others from the University of Pennsylvania and the Vertical Lift Research Center of Excellence for providing geometry and/or grids for this work. Their dedication to producing experimental data for this work is also much appreciated.

This research was partially funded by the US Army's National Rotorcraft Technology Center program, effort sponsored by the US Government under Other Transaction number W15QKN-10-9-0003 between Vertical Lift Consortium, Inc. and the Government, and by the Government under Agreement No. W911W6-17-2-0003. The US Government is authorized to reproduce and distribute reprints for Governmental purposes notwithstanding any copyright notation thereon. The views and conclusions contained herein are those of the authors and should not be interpreted as necessarily representing the official policies or endorsements, either expressed or implied, of the US Government. Some images in this paper were created using FieldView, licenses for which were provided through the FieldView University Partners Program.

Abstract

The rotor hub is one of the most important features of all helicopters, as it provides the pilot a means for controlling the vehicle by changing the characteristics of the main and tail rotors. The hub also provides a structural foundation for the rotors and allows for the rotor blades to respond to aerodynamic forces while maintaining controllability and stability. Due to the inherent geometry and high rate of rotation, the rotor hub in its current form acts a large bluff body and is the primary source of parasite drag on the helicopter, despite its relatively small size. The rotor hub also produces a highly turbulent wake which can affect the performance of the vehicle's empennage and tail rotor. Much of the characteristics and behaviors of this wake are still difficult to predict and analyze, but the application of numerical simulations makes this task easier and more efficient. The turbulent and frequency content characteristics were examined in the wakes of four helicopter rotor hub geometries in forward flight. Computational fluid dynamics (CFD) simulations were performed using NASA's OVERFLOW 2.2n Reynolds-averaged Navier Stokes solver, and the simulations imposed flow conditions based on previous and current experimental and numerical studies. Surface force and velocity harmonics for several frequencies were computed and qualitatively compared against available experimental results. Components of the Reynolds stress tensor were computed and examined. Production and transport of the turbulent kinetic energy are examined through the rotor hub wakes at six stream-wise coordinates. Frequency content was found to be concentrated towards the retreating side of all hubs in most of the frequencies examined, and certain geometrical features of the hubs were found to contribute significantly greater portions of this frequency content than others. Reynolds stresses showed similar concentrations as the mean velocity contours, which displayed a general bias towards the advancing side due to the increased relative velocity. Modal analysis of the instantaneous

Reynolds stresses showed that perturbations directly behind the advancing side could only be captured with a large set of modes. Integrations of a turbulent kinetic energy flux and the stream-wise third-order moment showed a nearly-linear relation between the frontal area of the hubs and the magnitudes of these quantities.

Table of Contents

1 Introduction **1**

1.1 Research Goals 4

2 Background **5**

2.1 Modern Rotor Hubs and Their Role 5

2.2 Aerodynamic Concerns 9

2.2.1 Drag 9

2.2.2 Wake Behavior 16

2.3 Recent Research and Developments 19

3 Analysis Methodologies **22**

3.1 Rotor Hub Geometries 22

3.2 Computational Methodology 23

3.2.1 Governing Equations and Solving Methods 23

3.2.2 Grid Generation and Connectivity 33

3.2.3 Simulation Inputs and Boundary Conditions 35

3.3 Post-processing Background and Methods 35

3.3.1 Turbulent Kinetic Energy and Reynolds Stresses 36

3.3.2 Proper Orthogonal Decomposition 38

4 Results **41**

4.1 Instantaneous Wake Capture and Surface Forces 41

4.2 Time-Averaged Velocity Profiles 43

4.3 Frequency Content of Velocity Profiles 45
4.4 Turbulent Kinetic Energy 47
4.4.1 Reynolds Stresses 47
4.4.2 Third-Order Moments 51
4.4.3 Turbulent Kinetic Energy Fluxes 52
4.4.4 Modal Decomposition of Reynolds Stresses 53

5 Conclusions **56**

References **60**

Appendix **73**

A Chapter 1 Figures and Tables 73
B Chapter 2 Figures and Tables 77
C Chapter 3 Figures and Tables 84
D Chapter 4 Figures and Tables 88

Vita **113**

Nomenclature

A_{ref}	reference area
D_{hub}	rotor hub diameter
e_0	total energy
$f_e, \frac{L}{q}, \frac{D}{q}$	effective flat plate area
k	incompressible turbulent kinetic energy
P, p	pressure
Re_{hub}	Reynolds number based on rotor hub diameter
u_i	velocity component
$\overline{u_i}$	time-averaged velocity component
u_i'	velocity component perturbation
x, y, z	Cartesian coordinate components
y^+	wall-normal non-dimensional grid spacing
κ	coefficient of thermal conductivity, Kármán constant
λ	Stokes' hypothesis
μ	rotor advance ratio
μ_{hub}	hub advance ratio

ν	kinematic viscosity
ν_t	eddy viscosity
$\tilde{\nu}$	Spalart-Allmaras working variable
Ψ	hub azimuth angle
ρ	air density
τ	shear stress

Chapter 1: Introduction

The helicopter is a type of aircraft which uses an open-air rotor as its main source of lift and control, and is capable of vertical take-off and landing (VTOL) and hovering flight [1, 2]. An example of a helicopter is pictured in Fig. 1*. The controls afforded to the pilot provide a full range of motion, allowing for longitudinal and lateral movement as well as climbing and descending. Longitudinal and lateral movement is accomplished by tilting the main rotor in the desired direction via the cyclic pitch, which changes how much lift each rotor blade is producing depending on its azimuthal position. Vertical climb and descent is done by altering the collective pitch of the main rotor, which changes the amount of lift being produced by the rotor blades evenly. Yaw control is generally attained through the use of a separate, smaller rotor which is oriented in a perpendicular fashion with respect to the main rotor and located aft of the main rotor as part of the empennage. This secondary rotor also acts to counteract the resultant torque produced by the main rotor. The helicopter configuration described and pictured in Fig. 1 is the most common type of helicopter in use and is thus considered the conventional configuration [1]. For their VTOL capabilities, helicopters have proven useful in a myriad of applications, ranging from search-and-rescue to logistics. They are also the predominant type of VTOL-capable aircraft due to their lower energy consumption and relatively lower produced downwash, compared with other types of VTOL-capable aircraft [1].

One of the most fundamental characteristics of any aircraft is its controllability, as this is required to function as needed and to accomplish its intended task safely. For helicopters, this has proven to be a challenge for multiple reasons. In the early development of helicopters, the first problem tackled was the torque reaction on the vehicle from the large main rotor. In the early development of helicopters, it was common to change the configuration and number of lifting rotors in order to solve this issue. Some examples of early rotorcraft configurations are shown in Fig. 2. Although multi-rotor configurations such as quad-copters (Fig. 2a), tandem helicopters (Fig. 2b), and coaxial helicopters (Figs. 2c, 2d) were the common

*All figures and tables referenced are included in appendices at the end of this document.

variations among the early pioneers, the single rotor with perpendicular tail rotor that is common today was also seen [3]. Pascara's design was groundbreaking for the time for not only setting a world record in forward flight, it was also one of the first examples of a rotorcraft's use of modulated cyclic and collective pitch for control, instead of attaching additional rotors [3]. This method of control would later become the standard for modern helicopters as the technology progressed.

Other issues with controllability were also discovered soon in the helicopter's development. In forward flight, an uneven lift distribution on the main rotor is created due to the difference in relative velocities on the advancing and retreating sides of the rotor as illustrated in Fig. 3. This dissymmetry of lift would cause the craft to roll strongly towards the retreating side of the rotor. It was discovered that this issue could be solved by allowing the rotor blades to independently flap, which would change the effective angle of attack of each blade and thus change the amount of lift produced. Juan de la Cierva is credited with first incorporating this solution into a successful vehicle with his Autogyros [2]. This flapping motion in turn induces a Coriolis acceleration on the rotor blades, which can fatigue the blades [1], necessitating the freedom to 'lead' and 'lag' horizontally [2]. The incorporation of the flapping hinges, lead-lag hinges, and the mechanics required for control of the collective and cyclic pitch onto the helicopter eventually led to the modern day rotor hub.

Modern rotor hubs are generally organized into four basic configurations, which are known as the teetering, the fully articulated, the hingeless, and the bearingless [4]. The early design of functional rotor hubs, consisting of many hinges, bearings, and linkages, is known as a fully articulated hub and is still in use today, such as on the Boeing CH-46 pictured in Fig. 5. Although this configuration is mechanically complicated and has proven to have high maintenance costs, it is reliable and is used on many helicopters [2]. The teetering design, which is shown in Fig. 4, is a strictly a two-bladed design and incorporates a single hinge located at the axis of rotation which allows the blades to move freely but dependently; as one blade flaps upwards, the other blade flaps downwards. A stabilizer bar is also included to increase gyroscopic stability. This design is in general more mechanically simple and is easy to maintain due to the low number of parts [2]. The hingeless and bearingless configurations (also referred to as rigid rotor hubs [5]) are similar to the fully articulated hub, except that

instead of hinges to account for operating loads and functionality, the structure itself allows for bending. Examples of these types of hubs are pictured in Figs. 6-7. These systems are more mechanically simple in their design but are structurally complex, and modern composites are needed in their construction. These hubs are also relatively stiff, giving the pilot a quick and firm response [2] but are susceptible to increased vibrational loads [5].

Due to their mechanical, structural, and operational importance, rotor hubs have never particularly been designed with drag reduction or aerodynamics first. Rather, the focus of rotor hub design has been mainly to prevent failure, increase reliability and decrease maintenance and cost [4]. Despite this, much work has been done to study the drag contributed from rotor hubs dating back to 1959 [6], and it was found early on that rotor hubs typically contributed a majority of the vehicle drag, followed closely by landing gear [7, 8]. Unlike landing gear, which can be retracted completely into the fuselage, the rotor hub must stay exposed due to its rotation. Although various techniques have been developed to reduce this drag, such as reducing the projected frontal area or hub fairings, it can be expected that the rotor hub will contribute anywhere from 20% to 50% of the total vehicle drag [4, 8, 9]. This problem has been exacerbated as rotorcraft forward flight speeds have increased [8].

Another issue that was discovered as certain design choices were implemented, such as increased disk loading and decreased vehicle size, is interactional aerodynamics [10]. There are many different types of interactional aerodynamics present in rotorcraft flight, and one of them is between the rotor hub wake and the empennage, including the tail rotor. This can impose vibratory loads onto the empennage which increases the cost and frequency of maintenance. It can also decrease the effectiveness of the tail rotor, decreasing the overall controllability of the helicopter. The aerodynamic phenomena produced in the wake of the rotor hub are so complex that for many years it has been, generally, entirely unfeasible to address them with anything but flight testing [9]. With the advent of modern high-performance computing and increasingly accurate computational fluid dynamics (CFD), the prediction and study of rotor hub wakes can be undertaken with increased productivity. This includes identifying the spatial locations and sources of high-energy turbulent flow in the wakes, the knowledge of which can help with improving rotorcraft designs and efficiency.

1.1 Research Goals

The primary focus of this work is to identify and characterize high-energy flow phenomena in rotor hub wakes. Several rotor hub geometries are simulated and flow field characteristics such as instantaneous velocity components and Reynolds stresses are computed and analyzed. Fast Fourier Transform and Proper Orthogonal Decomposition (POD) are used to try and uncover characteristic behaviors in the wakes. The primary objectives of this work are summarized as,

1. Complete the domain discretization and simulation of four rotor hub geometries for comparison.

2. Compute the Reynolds stress components and third-order moments from instantaneous flow quantities at several planes positioned normally to the flow and at evenly-spaced coordinates downstream of each hub.

3. Quantify frequency content in the wake by computing the discrete Fourier transform. Perform a qualitative comparison against experimental results as appropriate. Spatially locate and analyze the high-energy flow phenomena captured within the frequency content.

4. Analyze the Reynolds stresses, third-order moments, and turbulent kinetic energy in the wake. Assess their capture by the computational grid using Reynolds stress profiles and the power spectral density.

5. Perform principle component analysis through the Identification of the dominant POD modes of the Reynolds stresses.

Chapter 2: Background

2.1 Modern Rotor Hubs and Their Role

There are many different types of effective helicopter designs, each with specific advantages and disadvantages. These designs are generally distinguished by their role and their main rotor configuration, which can be installed into a singular configuration with a tail rotor or into a multiple rotor configuration, also known as a compound helicopter. There are several different types of compound helicopter configurations known as coaxial, tandem, and intermeshing [5], and these are pictured in Figs. 8-10. Each rotor on a helicopter is centered around a rotor hub, which controls the angle of attack of the rotor blades both individually (cyclic pitch) and en masse (collective pitch); this control allows the pilot to modulate the helicopter's lifting thrust as well as the orientation of the main rotor(s) for longitudinal and horizontal movement [2]. The rotor hubs must also account for aerodynamic forces acting on the rotor blades which causes them to flap as they move azimuthally. Coriolis accelerations and drag forces cause the rotor blades to lag in the in-plane direction [2], requiring mechanisms to reduce the resultant stress and fatigue. The various types of movements also make the rotor hub structurally complex, as it needs to also withstand large centrifugal forces acting on the rotor blades and keep the rotor blades attached to the vehicle. These functions are accomplished in a variety of ways depending on the kind of rotor hub, and each kind has its own advantages and disadvantages. What follows is a summary of the structural function of the rotor hub and its components; for a discussion on the history of the development of rotor hubs, see Wall [11].

Arguably one of the most important and challenging functions of the rotor hub is the control over the pitch of the rotor blades. This is difficult because control must be translated from a non-rotating structure (the helicopter fuselage) to a highly-rotational one (the rotor). For a majority of rotorcraft in use, this control transition is facilitated through the use of a swashplate as seen in Fig. 11. The swashplate is made up of three components: a non-rotating disk and a rotating disk [12]. The disks have a set of bearings between them

to allow for rotation of the upper disk, and the rotating disk has connections for linkages which connect to the rotor blades. These components are placed concentric to the rotor shaft. Control links are connected to the non-rotating disk, and these vertically translate or tilt the non-rotating disk based on inputs from the pilot. These inputs in turn affect the rotating disk accordingly, which changes the vertical position of the attached linkages. These linkages are attached to pitch horns connected to the rotor blades, and the change in vertical position of the pitch horns causes a moment on the rotor blades, rotating them and changing their pitch or angle of attack. An equal, vertical input from the control links onto the swashplate will result in an equal change in angle of attack of the rotor blades; this is known as collective pitch. An unequal, tilted input from the control links will result in an unequal change in angle of attack of the rotor blades, which depends on the azimuthal position of the rotor blades; this is called cyclic pitch. Each disk of the swashplate also has an additional link known as a drive/anti-drive link or scissor link to ensure they are rotating properly. The rotating disk has a scissor link attached to the drive shaft to ensure it rotates with the blades, and the non-rotating disk has a similar scissor link attached to the fuselage [5]. Other mechanisms to accomplish collective and cyclic pitch exist and have been developed in the past, such as the Westland Helicopters spider system [12] or the Kaman servo-tab [13], but the swashplate remains one of the most common implementations on modern helicopters. In general, hubs will have this swashplate feature in common despite how they accomplish their other functions.

Another feature common on helicopters are fairings, which can be used to cover the pylon (lower portion of the rotor hub) or the hub itself as shown in Fig. 12. The pylon fairing is much more common with modern rotorcraft, with every modern helicopter in production having one incorporated into its design [4]. These pylon fairings in general will reduce hub parasite drag significantly, as well as provide opportunities to modify the rotor wake [14]. Rotor hub fairings are less popular than pylon fairings, although partial fairings such as the so-called "beanie" fairing, which is pictured in Fig. 13, have become common in helicopter rotor hub design. The lower usage of hub fairings is due mostly to the increased weight, structural complexity, and maintenance requirements outweighing any benefits from drag reduction [4].

The first type of functional rotor hub to be developed was the fully articulated hub, and is still a very common model used on helicopters today [2]. This hub, being the direct result of early experimentation, is conceptually simple but mechanically complex. The complexity of this type of hub is illustrated in Fig. 5. The fully articulated rotor hub's distinguishing feature is its use of several hinges to facilitate the three degrees of freedom needed by the blades. Flapping is allowed through a horizontally-orientated hinge (known as the flap hinge), and the lead-lag motion is similarly allowed through a vertically-orientated hinge known as the lead-lag hinge or lag hinge. The geometry which allows the pitch of the blades to vary is labeled as the feather hinge in Fig. 5, which is controlled by a pitch horn attached by a pushrod to the swashplate. A damper is also generally attached to dampen the lead-lag motion of the blades in order to prevent aeromechanical instabilities such as ground or air resonance [2, 15]. Moving outwards from the rotor's center of rotation, the order which the various hinges appear in varies depending on the manufacturer and helicopter model, as well as the form which the hinges take on. Examples of comparisons include the Aerospatiale SA 342 (flap-pitch-lag) versus the SA 330 (flap/lag-pitch) hubs (Figs. 14-15) and the Boeing CH-46 (flap-lag-pitch) versus the CH-47 (flap-pitch-lag) hubs (Fig 5 and Fig. 16) [4]. This rotor hub type is plagued by its high part count and required maintenance, as well as increased vehicle drag due to its complicated geometry. The fully articulated rotor hub's manufacturing costs are also generally higher due to the increased part count compared with other rotor hub designs [16]. Despite this, it has proven its worth by providing good control of the helicopter and being reliable [2].

In 1943, Arthur Young flew a two-bladed single rotor helicopter, which was fitted with a mechanical gyroscope of his own design. This device partially controlled the feathering motion of the rotor, and acted as a stabilizer bar; this gave the helicopter greatly increased stability and was much easier to control. Young later collaborated with Bell Aircraft Company which resulted in the Bell Model 47 pictured in Fig. 17, which was the first helicopter to receive a civil certificate. The rotor hub incorporated onto this helicopter and the ones that followed its design philosophy are known as teetering, seesaw, or semi-rigid rotor hubs. This type of hub was ground breaking at the time for a few reasons. Unlike the fully-articulated hub, the teetering hub has no lead-lag hinge, instead being

strengthened in the in-plane direction. The flapping motion required to balance the rotor's lift in forward flight is handled by a single hinge centered on the hub as shown in Fig. 4. By design it also provides greater stability through the stabilizer bar, while still maintaining a relatively low part count. The removal of the lead-lag hinge also reduces the probability of ground resonance by uncoupling the lead-lag motion of the rotor blades from the landing gear motion [4]. Although the teetering rotor hub is limited to two-bladed rotors and does not as reactive as controls as an articulated hub [5], the benefits of low weight, mechanical simplicity, and greatly increased stability have made it the most popular rotor hub incorporated onto helicopters [4].

Starting in the mid 1960s, efforts began to innovate on rotor hubs in order to reduce rotor hub drag and simultaneously reduce mechanical complexity and maintenance costs. This effort led to the advent of the class of hubs known as rigid rotor hubs. Physically similar to the rotor hubs found on the helicopters of the early 20th century such as the aforementioned Bréguet-Richet Gyroplane No. 1 shown in Fig. 2a, these rigid rotor hubs are much more structurally advanced. The basic premise of these rotor hubs is to replace mechanisms required to compensate for the various forces on the rotor hubs blades with solid structures that bend and react, effectively acting like the hinges they replaced. Rigid rotors, like the ones pictured in Figs. 6-7, incorporate composite materials such as fiberglass or carbon fiber that allow for portions of the rotor hub and rotor blade root to flex in response to the forces applied to them in flight [17]. Specifically, hingeless rotor hubs like the one on the BO-105 replace the flapping and lead-lag hinges, but keep the feathering hinge (cf. Weiland [18] for a developmental history of this rotor hub). Bearingless hubs take a similar approach as the hingeless rotor hubs, but also do away with the feathering hinge. These rotor hubs, which first showed up in 1966 [19], apply a torsion to the rotor blade root in order to feather the rotor. These hubs are advantageous when considering part count, maintenance costs, and weight. However, their design is challenging due to the use of composites, and have been in general to be susceptible to increased vibrational loads [5, 20, 21]. The drag from these rotor hubs is also not in general any less than that of fully articulated rotor hubs [4].

2.2 Aerodynamic Concerns

2.2.1 Drag

It was in the 1950s that drag began to be a more important aspect of helicopter design, as helicopters were to be considered for roles requiring higher top speeds and greater flight ranges; a decrease in drag could result in a significant increase in performance at those speeds and ranges. Harrington [22] was the first to emphasize parasite drag as an important topic for the future development of helicopters, and discussed the confirmed and possible major contributors to parasite drag on helicopters: landing gear, engine exhaust stacks, cooling-air systems, various aspects of the fuselage such as gaps and external protuberances, and rotor hubs. Preliminary estimations made by Harrington showed that a 50% reduction in parasite drag could result in a 25% increase in maximum range and similar improvements to top speed and best speed for range. Concerning rotor hubs, Harrington pointed out that although much was unknown about their contribution to parasite drag, it was known that rotor hub fairings could significantly reduce their effective flat plate areas [22]. In 1959 Churchill and Harrington [6] conducted wind tunnel tests on 5 rotor hubs in production at the time to determine the parasite drag, as well as to begin testing the effectiveness of rotor hub and blade shank fairings. The hub geometries they tested were variations of the teetering and fully articulated rotor hub types. They found that factors such as angle of attack, hub rotational speed, and forward velocity had an inconsequential effect on the effective flat plate area (Δf in Ref. [6], and f_e in the current work) of the hubs. They also noted that the rotor hubs' drag coefficients tended to rise with projected frontal areas. Sweet and Jenkins [23] continued with wind tunnel tests of several helicopter fuselages including several rotor hub and pylon configurations, as well as landing gear. The two rotor hubs tested were both fully articulated, with one being faired and having a 66% greater projected frontal area. The pylons tested varied the distance between the rotor disk and the fuselage. They found that besides the landing gear, the rotor hub and pylon installation contributed the most to total vehicle parasite drag, estimating its contribution to be approximately 20 to 30%. They also found, for their particular geometries, that the faired hub had no particular advantage over

the unfaired hub, as the effects of streamlining the rotor hub were offset by the increase in projected frontal area. Linville [24] performed wind tunnel tests of two hub and pylon fairing configurations with a representative 4-bladed fully-articulated rotor hub, and compared them to an unfaired rotor hub. The two hub configurations consisted of a rigid fairing, which was a fitted, sealed cover for the rotor hub, and a floating fairing, which was an ellipsoidal fairing. The rigid configuration also sat against the pylon, whereas the floating configuration was vertically spaced away from the pylon. Their results showed that the floating rotor hub configuration resulted in the greatest decrease in drag in comparison with the unfaired rotor hub at Mach numbers up to 0.4. However, the reductions in drag for both the rigid and floating configurations were significantly reduced (or completely negated, as was the case for the floating configuration due to its relatively large projected frontal area) when the free-stream Mach number approached and exceeded 0.6. They also concluded that reduction of the projected frontal area of the rotor hub was particularly important for reducing parasite drag. With the work being done and data being compiled, the rotor hub's contribution to parasite drag was now understood to be significant, and efforts would continue to understand and reduce it.

As these efforts continued, several researchers and engineers worked to compile these findings and shed light on the independent, controllable factors influencing rotor hub drag. In 1975, Keys and Wiesner [7] compiled a summary of methods for reducing the parasite drag of helicopters through the design and/or modification of fuselage components like the landing gear, engine nacelles, and rotor hub. As noted in their paper, it was now known that the main rotor hub and landing gear accounted for more than 50% of the total aircraft drag. The contributions to parasite drag made by the landing gear could be reduced completely by incorporating retractable landing gear, but the contributions from the main rotor hub were not as easily diminished. Using hub drag trends, they estimated that hingeless rotors had approximately 30% less parasite drag than fully articulated configurations, due to the lack of the flapping and lag hinges as well as the lag dampers. They also noted that, if using the hingeless rotor as a baseline, parasite drag could be reduced a further 30% by incorporating a rotor hub fairing. For fully articulated hubs, they concluded that rotor hub fairings were not as successful due to the resulting significant increase in projected frontal

area. Boundary layer control (BLC) was also discussed, as it had been used in the past to reduce rotor hub drag [24]; it was concluded to provide minimal benefit as the extra power required would offset any power savings made by reducing drag. Another factor discussed was the effects of interference drag between the rotor hub and the fuselage, which could be reduced by increasing the spacing between the rotor hub and fuselage (pylon). However, this must be balanced as increasing the exposure of the rotor shaft would inevitably increase the overall parasite drag.

In 1976, Sheehy and Clark [25] used rotor hub drag data to produce semi-empirical methods for predicting the drag of unfaired, ellipsoidal faired, and rigid faired rotor hubs. This method was most significantly influenced by the projected frontal area of the rotor hubs, but also took into account the amount of exposed rotor shaft as well as estimations of interference drag. With wind tunnel testing this method proved to correlate within $\pm 14\%$ for a large set of rotor hub configurations. The next year, Sheehy [8] conducted a similar data review as what was done in Keys and Wiesner [7], but identified aspects which affected parasite drag directly related to rotor hub design. The rotor hub frontal area, the use of rotor hub fairings, pylon shape, hub/pylon spacing, the fuselage angle of attack, rotor hub rotation, aerodynamic sealing, Mach number, and scaling effects and Reynolds number were all discussed at length. As had been discussed in earlier works, the projected frontal area of the rotor hub was shown to be the most influential aspect affecting parasite drag, and remained the most important feature which future designs should take into account. Sheehy also was able to quantify the balance needed for the clearance between the rotor hub and pylon, as mentioned in Keys and Wiesner [7]. In 1981, Logan et al. [26] published their studies of the YAH-64 and UH-60A helicopter configurations, which included both experimental and analytical research, with a focus on rotor hub and pylon drag. The analytical analysis which they performed used a fully viscous panel method for a majority of the helicopter geometries, however the rotor hubs themselves were approximated using a momentum model based on the correlation published by Sheehy [8]. This was due to the number of panels that would have been needed to approximate the rotor hub's complex geometry being much too large for the program to sufficiently handle along with the rest of the helicopters' geometries. Based on the analytical analysis, wind tunnel models of the YAH-64 were made at approximately

25% and 80% scale and tested, and results of the wind tunnel tests were compared with the analytical results to find areas of agreement. Authors found, in agreement with previous works, that fairings tended to reduce parasite drag and that hub rotation had a minimal effect. During their analytical analysis, they were able to simulate engine airflow and found that it had a noticeable effect on the helicopter parasite drag, particularly due to the inflow. Scaling effects were also considered, and it was concluded for studies of the YAH-64 that a Reynolds number based on rotor hub diameter (Re_{hub}) of 300,000 or greater must be achieved in order to simulate full-scale conditions.

Starting in 1985 and continuing until 1989, a series of experiments to study rotor hub drag as well as rotor hub fairing designs and hub/pylon interactions were performed at NASA using the XH-59A Advancing Blade Concept helicopter pictured in Fig. 18 [27–31]. Felker [27] tested both 1/5- and full-scale models of the XH-59A and studied the effects of angle of attack, Mach and Reynolds number, hub rotation, and hub fairing geometry on rotor hub drag. Models were tested at Mach numbers ranging from 0.2 to 0.5, and Reynolds numbers of 1.1×10^6 - 2.3×10^6 (sub-scale) and 4.9×10^6 - 7×10^6 (full-scale). The hub fairings tested included included minimum projected frontal area fairings for the individual hubs as well as fairings for the rotor shaft exposed between each rotor hub. The best-performing configuration reduced rotor hub drag by 21% compared with the unfaired configuration. Their testing also found that, like the hub-pylon distance, the distance between the counter-rotating hubs to be important for controlling interference drag. Young et al. [28] continued testing with the $\frac{1}{5}$-scale model of the XH-59A, and included a more standard single rotor hub. This work focused on testing various hub and shaft fairings for both rotor hub types, and these geometries are shown in Fig. 19. The planform shape of the shaft fairings shown in Fig. 19d was found to influence parasite drag, as sloping the trailing edge resulted in a significant drag reduction when compared with a rectangular planform. A reduction in the thickness-to-chord ratio of the intermediate shaft fairing of the coaxial configuration was also found to be helpful, however the authors noted that it was only beneficial to achieve this reduction by increasing the chord of the shaft fairing, as increasing the fairing thickness would result in a larger projected frontal area and most likely increase drag. For coaxial hubs, they also found that flat surfaces on the lower sides of the elliptical fairings resulted in a reduction in

interference drag. The benefits of a flat-bottomed elliptical hub fairing, as noted in Stroub et al. [29], are only beneficial for a single rotor hub configuration when used in conjunction with a pylon fairing, and the rotor hub and pylon fairings are flush together. This eliminates any separated flow between the hub fairing and the pylon as well as eddies shed from the corners of the pylon. Graham et al. [30] and Sung et al. [31] performed continuation studies on hub-pylon interference drag and the characteristics of rotor hub drag, respectively, and studied these topics in more detail. In 1993, similar work by Martin et al. [32] studied the drag characteristics of a bearingless rotor hub on the Bell Helicopter Textron Model 222 pictured in Fig. 20, along with several hub and pylon fairing configurations. Success in reducing drag was achieved with the hub and pylon configurations, with the best geometry having a total drag nearly 21% lower than the unfaired geometry. This work also studied longitudinal and lateral forces and moments on the aircraft, which affect stability and controllability. They found that very large hub fairings, which increased parasite drag, also produced a decrease in longitudinal stability. The pylon fairings tested were found in general to increase horizontal tail effectiveness, but also decreased static directional stability due to the pylon planform area and the affected sidewash on the vertical tail.

As computational power increased, numerical methods like CFD were evaluated for their ability to accurately predict rotor hub surface forces as well as flow field characteristics. In 2008, Potsdam and le Pape [33], under the US/France Memorandum of Agreement on Helicopter Aeromechanics, performed CFD simulations of a NACA 0036 airfoil and planform with the same cross-section to evaluate the abilities of current CFD methods to capture the behavior of flow around helicopter engine pylons. Comparisons against wind tunnel test results were made, and the authors evaluated the capabilities of RANS, turbulence, and transition modeling. In general, the CFD methods were found to be sensitive to the particular numerical modeling schemes and dissipation associated with them. The turbulence models used varied widely and showed discrepancies between each other, and varied in terms of general performance. The CFD cases were also sensitive to chordwise transition locations, which were controlled with inputs to the transition models. Consensus between the CFD simulations and the experimental measurements of forces and surface pressure distributions was enhanced by including the wind tunnel walls, however the flow

visualization, qualitative behavior, and 3D effects did not compare as well. As the flow was massively separated, the authors concluded that the present CFD methods were not adequate for flow prediction, partially due to a lack of knowledge of some of the flow field phenomena occurring. Renaud et al. [34] simulated the Dauphin 365N helicopter and focused on fuselage performance and rotor-fuselage interaction prediction. Three RANS solvers were evaluated using both unstructured and structured grids, and a nonuniform actuator disk was used to approximate the rotor disk. Discrepancies were found between the CFD and experimental data, however results were fairly consistent between solvers. The actuator disk model used also correctly captured the fuselage pressures and qualitatively modeled the time-averaged rotor and fuselage vorticity flow field. Smith et al. [35] also assessed state-of-the-art methods for predicting rotor-fuselage interaction. The NASA-Langley ROtor Body INteraction (ROBIN) experiments [36, 37] were used for comparison, and the authors used unstructured and vorticity-transport-based Navier-Stokes solvers. Comparing against steady and unsteady surface pressure solutions and wake geometry, it was found that frequency content of the surface pressures were under-predicted but tended to match well between the unstructured and vorticity methods. As viscous effects were not included in the solvers used, characteristics of the surface pressures dominated by viscous effects were not captured well. Antoniadis et al. [38] simulated a generic full helicopter geometry to evaluate several grid types and RANS turbulence models as part of the GOAHEAD project. The greatest discrepancies between the experiments and the simulation data were found downstream of the main rotor hub and in areas of large separation. The authors note that some of the details of the flow field in the rotor wake were not fully captured by any of the numerical methods used. Agreement between the numerical and experimental results were adequate in other areas of the flow field.

Shenoy and Smith [39–42] of the Georgia Institute of Technology (GIT) conducted a thorough study of rotor hub drag using a variety of numerical methods. In 2011, Shenoy et al. [39] used an unstructured code to identify sources of hub drag on a complex rotor hub geometry, pictured in Fig. 21, in both model- and full-scale conditions. Scaling issues were found, meaning that grids developed for the model-scale analysis could not be applied to a full-scale analysis. Evaluation of the Reynolds number for each component when identifying

sources of drag and interference effects was found to be required when scaling results from model to full-scale, even for non-rotating configurations. Bluff body components of the rotor hub were found to lead to nonlinear scaling of the drag, through changes in interference effects as well as Reynolds number scaling. For rotating cases, the Magnus effect was identified to play a role in the determination of the interference drag. Shenoy et al. [40] performed CFD simulations of the same rotor hub, with both static and rotating cases. The rotor hub geometry was broken down into basic components such as the driveshaft, hub plates, pitchlinks, blade shanks, and swashplate; this enabled an analysis of each components' drag individually. Components of the hub where theoretical approximations were applicable were identified as ones which stayed clear of the shed wake, such as the swashplate. Due to interference and Reynolds number scaling effects, static analysis was found to be inadequate for predicting drag and side forces on the rotor hub. In Shenoy and Smith [41], scaling effects were studied by scaling the rotor hub to full-scale size. Components of the rotor hub which were bluff bodies tended to contribute to drag nonlinearly, which was caused through a combination of Reynolds number scaling and changes in the interference drag. Drag of components with rectangular cross sections tended to not vary much with Reynolds number, but this was not the case with cylindrical components. This was due to Reynolds numbers on these components, particularly for the drive shaft and blade shanks, transitioning from subcritical to supercritical values, which resulted in a 50%-67% drop in drag. Forbes et al. [43] studied the effects of rotation on the drag, side force, and torque of this same rotor hub using experimental methods. Drag was found to be affected insignificantly with increases in rotation speed, which agreed with past literature. Scissor arms with a 2/rev symmetry, when added to the rotor hub geometry, resulted in a 10% increase in drag but also reduced the periodic drag variation amplitude. The side force experienced by the hub was highly unsteady, with azimuth-resolved values changing sign within the time of one revolution. During this work, and outlined in detail in Shenoy et al. [42], a new method for overset unsteady grid feature-based adaptation was also developed. As a featured-based method, this method involved choosing an indicator by which the computational grid could be adapted. Although this method performed very well overall and was able to capture rotor vortex-fuselage interactions which had before then not been captured numerically,

uncertainty associated with the choice of adaptation indicator and the number of adaptation cycles indicated that a better method was desired.

Khier [44] in 2014 performed a numerical study of various rotor hub fairings in order to find methods for reducing drag, under the Clean Sky initiative in Europe. The geometries were simulated using an unstructured code and a k-ω RANS turbulence model. The drag of individual components of the rotor hubs, such as the blade stubs, blade attachments, and dampeners, was computed. It was found that the blade stubs and attachments contributed significantly to the hub drag, resulting in approximately 70% of the total hub drag. The authors discussed that proper design of the hub fairings, coupled with streamlining the bluff parts of the stubs, could result in a 17%-19% reduction in drag. Improvements in the fairings themselves resulted in a 6% drag reduction at constant lift conditions.

2.2.2 Wake Behavior

In the 1970s, the wake behavior of the rotor hub and the subsequent interactional aerodynamics started to be of interest to rotorcraft engineers. During the development of the YUH-61A, extensive experimental research was performed in order to understand the issues that had arisen from these phenomena and remove them. This analysis was mostly focused on harmonic analyses, and the experiments included studies of the harmonic content of fuselage surface pressures and velocity profiles of various parts of the helicopter. A portion of this report was also dedicated to the study of rotor hub wakes [45]. As part of the same program, Blake and Alansky [46] studied the downwash on the horizontal stabilizer from the rotor wake, which was exasperated by the increased horizontal stabilizer size. The larger stabilizer was incorporated in order to mitigate unsteadiness from the rotor hub wake. To balance the need for a larger horizontal stabilizer and the increase in downwash from the rotor wake, a movable horizontal stabilizer was incorporated, which reduced the downwash by pitching during flight. In 1980, Sheridan and Smith [10] discussed interactional aerodynamics and summarized the sources and issues identified in helicopter design. Wind tunnel testing was also performed and analyses of several interactional aerodynamics sources were presented, including a discussion on the interaction between the rotor, rotor hub, fuselage, and empennage. Lateral disturbances were recorded in their

wind tunnel experiments at speeds between 60 and 80 knots, and the author notes that these disturbances suggested an unstable interaction between the low pressure from the hub wake and the flow near the top of the fuselage.

With this new focus, engineers and scientists began studying the unsteady rotor hub wake in detail in the 1980s. As part of their analysis of rotor hubs and pylons mentioned previously, Logan et al. [26] also studied the aerodynamics near the empennage to study the rotor hub wake. They found that the asymmetric characteristics of the wake were significant even at low speeds. Higher wake velocities and downwash angles were found behind the advancing side of the rotor disk, and a strong sidewash towards the advancing side was attributed to the swirl effect in the wake from the rotor hub. In Roesch [14], the aerodynamic design considerations and challenges for the Aerospatiale SA 365N helicopter were summarized. During the flight testing stage of development, tail shake problems were encountered and found to be an excitation from the main rotor hub wake. This issue was particularly exasperated in descent, which caused the wake to move directly over the vertical tail. A comprehensive experimental research program was established to develop a solution to this problem, and a new pylon fairing was designed to move the rotor hub wake downwards and reduced its turbulence. This pylon fairing, coupled with a hub cap pylon, reduced dynamic pressure loss at the empennage by 11% and reduced the drag area of the hub by approximately 23%. In 1985 Roesch and Dequin [47] performed various experiments to visualize and analyze the rotor hub wake, with both model- and full-scale geometries. Large vortex structures were found in the wake of rotor hubs without blades, and these structures had a strong interaction with the flow over the fuselage based on the hub/fuselage spacing. This interaction, which caused the vortices to be shed with the blade passage frequency, was significantly decreased the an increased hub/fuselage spacing. Energies in the wake were also analyzed, and a spatial bias was found where the turbulent velocity fluctuations were concentrated more on the advancing side of the rotor hub, while the periodic velocity fluctuations (fluctuations with discrete frequencies associated with the hub geometry and blade passage) were concentrated on the retreating side of the rotor hub. The scissor arms were also found to a be a large source of velocity fluctuations with harmonic frequencies corresponding to the rotor hub rotation, particularly in the 1/rev and 2/rev frequencies.

From 1996 to 2002, Gorton et al. [48, 49, 50] studied the flow near the empennage of a 15%-scale model of the RAH-66 Comanche helicopter with the US Army 2-Meter Rotor Test System (2MRTS), as the aircraft had experienced high buffet loads on the empennage during testing. The experiments, which were performed in the NASA Langley 14.5 ft $\times$ 21.75 ft wind tunnel, found the horizontal tail sustained large changes in the unsteady sidewash and downwash angles due to the rotor wake. These effects also worsened with increasing advance ratio, as this caused the rotor wake to impinge more fully on the horizontal tail. At an advance ratio of 0.15, increased 2/rev frequency content of the vertical velocity was recorded near the horizontal tail, however its cause was not discussed. As part of the same project, Mason [51] performed an extensive analysis of the aerodynamic loads impinging on the empennage, and focused on identifying these loads using spectral methods. Data from structural frequency simulations performed using NASTRAN as well as flight-test data were used to estimate loads on the empennage. The flow around the main rotor hub and pylon and how it affected the flow near the empennage was investigated, however only general recommendations for improvement were provided.

Berry [52] performed experimental investigations of the unsteady wake behind the same rotor hub used in Gorton et al. [48, 49, 50], but with a generic helicopter fuselage which was analytically designed. Periodic and turbulent velocity fluctuations were analyzed at many points within the wake, starting from a streamwise coordinate corresponding to the rotor blade root and extending to just beyond the blade tip, and approximately 1 rotor hub diameter (D_{hub}) in both spanwise directions. Average turbulence intensities were presented, and it was found that the levels of this quantity were substantially greater on the retreating side of the hub than the advancing side. Moving downstream, the levels of mean turbulence also showed a lower decay rate when positioned directly behind the rotor hub. Unexpectedly, the streamwise velocity component also exhibited increased 2/rev content as the measuring coordinate moved downstream, until a point corresponding to approximately 50% of the blade where the 4/rev content becomes larger. The author explained that the load on the blades, which became significant near this point, could have been a possible explanation for the switch in dominant frequency.

At the turn of the century, engineers began applying CFD methods to rotorcraft prediction and evaluating their capabilities. However, due to the complex nature of the subject, most geometries used for simulation were simplified including the removal of the rotor hub (cf. [53–58]). In 2013, Raghav et al. [59] one of the first extensive numerical analyses of the rotor hub wake, as part of the work mentioned previously by Shenoy and Smith [39–42]. A 1/4-scale four-bladed rotor hub model with $D_{hub} = 0.44m$, pictured in Fig. 21, was used for analysis. An unstructured, overset grid was used in conjunction with a hybrid RANS and large eddy simulation (LES) turbulence model was used to simulate a baseline geometry as well as several increasingly simplified geometries to deconstruct the drag. Both static and rotating conditions were simulated. Velocity characterization of the near wake ($x = 0.5D_{hub}$) showed good agreement with experimental work, particularly for the rotating case. The wake offset due to the hub's rotation was clearly captured, and vorticity magnitude contours seemed to show better wake capture with the adapted grids than with the initial ones. Power spectral density (PSD) of unsteady velocity data also showed good agreement with experimental data with respect to behavior, and displayed the expected $-5/3$ slope in most cases. Forbes et al. [43] used the PSD of velocity measurements in the near wake $x = D_{hub}$ showed an asymmetry in the 4/rev energy content, with higher content being focused on the retreating side of the rotor hub.

2.3 Recent Research and Developments

From 2012, the US Army, Penn State University (PSU), the Georgia Institute of Technology (GIT), and the University of Tennessee Knoxville (UTK) have been working together under a National Rotorcraft Technology Center (NRTC) / Vertical Lift Consortium (VLC) Other Transactional Agreement (OTA) to facilitate the development of Future Vertical Lift (FVL) rotorcraft. This work was the first modern, high-quality work in the United States including CFD and experimental studies of rotor hub drag, interactional aerodynamics, and rotor hub wakes at full-scale Reynolds numbers. Experimental works at PSU and GIT were performed under their Vertical Lift Research Center of Excellence (VLRCOE) chapter. In 2014, Reich et al. [60] performed CFD simulations and experimental studies of a model-scale notional

rotor hub geometry (known as the Baseline hub) at PSU. The CFD simulations were carried out using an unsteady RANS (URANS) simulation routine with $Re_{hub} = 4.9 \times 10^6$, and the realizable $k - \epsilon$ turbulence model was used for closure. Experiments were carried out in the 48-inch Garfield Thomas Water Tunnel using a 1:4.25-scale model at $Re_{hub} = 2.45 \times 10^6$ and $Re_{hub} = 4.9 \times 10^6$. Harmonic behaviors of the vertical velocity in the wake were measured, with the 2- and 4-per-revolution (2/rev and 4/rev) harmonics dominating due to the rotor hub geometry. Far wake ($x = 3.5D_{hub}$) results agreed very well between the experimental and numerical results. Results in the near wake ($x = D_{hub}$) did not agree as well as the far wake results due to small differences between the CFD and tunnel model geometries such as surface roughness and corner sharpness. In 2018, Reich et al. [61] performed similar experimental studies of the Baseline hub as well as a representative near-future, low-drag hub called the Low Drag hub. The hub models were 1:17 scale, and the focus of the study was to investigate interactional aerodynamics between the rotor hubs and engine pylon surfaces and visualize the near wake. A frequency analysis of the velocity field of the wake generated by these hubs, within a plane located at $x = D_{hub}$, found distinct behavior in the 2/rev and 4/rev frequencies which highlighted a general bias of velocity fluctuations towards the retreating side of the hub. This trend was opposite to the trend seen in the mean velocity field in the same plane, and the cause for both trends was attributed to the increased relative velocity on the advancing side and the Magnus effect. These results exhibit similar behavior to what was reported in Roesch and Dequin [47].

Potsdam and Cross [62] performed CFD simulations using the Baseline hub geometry. This work was primarily to assess the abilities of the DoD HPCMP CREATE-AV Helios [63] for predicting rotor hub performance and wakes. The near-body turbulence closure was accomplished using the Spalart-Allmaras Detached Eddy Simulation (SA-DES) model, and various off-body treatments were used and compared. Direct comparisons against the results from PSU were also used for this work. It was found that drag hub was predicted reasonably well, with differences between the CFD and experimental results staying with 6.5%. The wake deficit was found to be under-predicted, the authors observed that the wake frequency content in general, particularly in the near wake ($x = D_{hub}$, was not well-captured. Potsdam and Sitaraman [64] similarly assessed CREATE-AV Helios using both

the Baseline geometry and the Low Drag hub. Along with drag, rotor hub wake impingement on a horizontal stabilizer was studied and results were compared with experimental data [65]. The horizontal stabilizer was installed at $x = 3.5D_{hub}$, which was equivalently scaled from a heavy-lift commercial helicopter. Total hub drag compared well against the experimental work, and the drag reduction between the Baseline and Low Drag hubs was captured very accurately. Lift harmonics of the horizontal stabilizer were found to not agree well with experimental data, and convergence of lift statistics was found to require 15-20 rotor hub revolutions. Coder [66] studied the effects of employing transition modeling to rotor hub simulations, but found no appreciable difference between transition modeling and simulating the system as fully turbulent. The author notes that any significant improvement in hub drag would most likely be found through a reduction in flow separation. Wall and Coder [67] performed modal decomposition analysis on the same rotor hub geometries in addition to a third hub, which was the same geometrically as the Baseline hub but was defeatured by removing the scissor arms and swashplate. This configuration is hereafter referred to as the Defeatured Hub. This study included proper orthogonal decomposition and various other system decomposition results and identified coherent behaviors within fixed frequencies, such as 2/rev and 4/rev, in the rotor hub wakes; it also showed a lack of coherence in the cycle-to-cycle variations. Spectral proper orthogonal decomposition revealed coherent structures in the frequency content of the streamwise momentum, but modal energy proved to be invaluable for identifying which modes contained these coherent structures.

Throughout this work, several Rotor Hub Workshops were convened to compile together the data and results from these works, and to discuss and compare results. These workshops, which took place in 2016, 2018, and 2020, are summarized in Schmitz et al. [68, 69, 70]. The work discussed in this document is a continuation of the work summarized in these Rotor Hub Workshops under the OTA mentioned.

Chapter 3: Analysis Methodologies

3.1 Rotor Hub Geometries

Four rotor hub configurations were simulated in this study and are based on those used in Schmitz et al. [68, 69, 70]. Previous numerical work with three of these rotor hub geometries is documented in Coder [66] and Wall [11], Wall and Coder [67]. One of the water tunnel models used in the experimental work is shown in Fig. 22 with components labeled, and all of the geometries used in this study have some or all of the components shown. This model, known as the Phase III hub, is a model-scale simplified geometry of a present industry standard rotor hub, and was provided to VLRCOE by Sikorsky Aircraft Corporation [60]. The four geometries are designated as the Baseline hub, the Defeatured hub, the Low Drag hub, and the Phase III hub, respectively (Fig. 23). The Baseline hub (Fig. 23a), represented what was considered a standard rotor hub common in use, with rotor blade arms, upper and lower spiders, scissor arms, and a swashplate. The Defeatured hub, (Fig. 23b), was based on the Baseline hub, but the scissor arms and swashplate were removed. This model was inspired by Potsdam and Cross [62], where it was found that the blade arms were the greatest contributors to drag, followed by the swashplate and scissor arms. The swashplate and scissor arms were also found to be significant sources of frequency content in the wake. The Low Drag hub (Fig. 23c), was also based on the Baseline hub and featured aerodynamically optimized rotor blade arms and only the lower spider. It should be noted, as per Wall [11], the Defeatured and Low Drag hubs have the same frontal projected area. Lastly, the Phase III hub (Fig. 23d), contained all the features as the Baseline hub, as well as a circular indent on the top spider. This hub geometry was included as it fully mimics the water-tunnel model (Fig. 22) used in Schmitz et al. [68, 69, 70]) and is thus a direct comparison to those results, as well as the current experimental results shown in this work. Notably, the pitch links were removed from the Baseline and Phase III models, as they were for the experimental work. Past works have shown that the pitch links do not appreciably affect the drag characteristics of rotor hubs [41, 60]. For this study the hubs were simulated in

free air and were isolated from all other geometry including the wind tunnel pylons used in experimental works. Prior experimental and numerical studies with the Phase III hub installed in the tunnel are documented in Potsdam and Cross [62], Potsdam and Sitaraman [64], Coder [66], and Wall and Coder [67].

3.2 Computational Methodology

3.2.1 Governing Equations and Solving Methods

The simulations for the four hub geometries were performed using the structured, overset Reynolds-averaged Navier-Stokes (RANS) solver OVERFLOW 2.2n code [71], which is a density-based, node-centered, finite-difference code. This solver was developed and is maintained by NASA. OVERFLOW is capable of simulating axisymmetric, two-dimensional, and three-dimensional geometries, and supports six degree-of-freedom motion. This solver solves the Navier-Stokes equations implicitly, using a generalized form in curvilinear coordinates which is given as [72],

$$\frac{\partial \vec{q}}{\partial t} + \frac{\partial}{\partial \xi}\left(\vec{E} - \vec{E}_\nu\right) + \frac{\partial}{\partial \eta}\left(\vec{F} - \vec{F}_\nu\right) + \frac{\partial}{\partial \zeta}\left(\vec{G} - \vec{G}_\nu\right) = 0 \tag{3.1}$$

where $\vec{q}$ is the vector of conserved variables and $\vec{E}$, $\vec{F}$, and $\vec{G}$ are the inviscid fluxes which are

$$\vec{q} = J^{-1}\begin{bmatrix}\rho\\ \rho u\\ \rho v\\ \rho w\\ \rho e_0\end{bmatrix}, \quad \vec{E} = J^{-1}\begin{bmatrix}\rho U\\ \rho u U + \xi_x P\\ \rho v U + \xi_y P\\ \rho w U + \xi_z P\\ U(\rho e_o + P) - \xi_t P\end{bmatrix}, \quad \vec{F} = J^{-1}\begin{bmatrix}\rho V\\ \rho u V + \eta_x P\\ \rho v V + \eta_y P\\ \rho w V + \eta_z P\\ V(\rho e_o + P) - \eta_t P\end{bmatrix},$$
$$\vec{G} = J^{-1}\begin{bmatrix}\rho W\\ \rho u W + \zeta_x P\\ \rho v W + \zeta_y P\\ \rho w W + \zeta_z P\\ V(\rho e_o + P) - \zeta_z P\end{bmatrix} \tag{3.2}$$

The contravariant velocities U, V, and W in Eq. 3.2 are

$$\begin{aligned} U &= \xi_t + \xi_x u + \xi_y v + \xi_z w \\ V &= \eta_t + \eta_x u + \eta_y v + \eta_z w \\ W &= \zeta_t + \zeta_x u + \zeta_y v + \zeta_z w \end{aligned} \tag{3.3}$$

The viscous flux terms, denoted by the kinematic viscosity ν subscript, are given as

$$\vec{E}_\nu = J^{-1}\begin{bmatrix} 0 \\ \xi_x\tau_{xx} + \xi_y\tau_{xy} + \xi_z\tau_{xz} \\ \xi_x\tau_{yx} + \xi_y\tau_{yy} + \xi_z\tau_{yz} \\ \xi_x\tau_{zx} + \xi_y\tau_{zy} + \xi_z\tau_{zz} \\ \xi_x\beta_x + \xi_y\beta_y + \xi_z\beta_z \end{bmatrix}, \quad \vec{F}_\nu = J^{-1}\begin{bmatrix} 0 \\ \eta_x\tau_{xx} + \eta_y\tau_{xy} + \eta_z\tau_{xz} \\ \eta_x\tau_{yx} + \eta_y\tau_{yy} + \eta_z\tau_{yz} \\ \eta_x\tau_{zx} + \eta_y\tau_{zy} + \eta_z\tau_{zz} \\ \eta_x\beta_x + \eta_y\beta_y + \eta_z\beta_z \end{bmatrix},$$
$$\vec{G}_\nu = J^{-1}\begin{bmatrix} 0 \\ \zeta_x\tau_{xx} + \zeta_y\tau_{xy} + \zeta_z\tau_{xz} \\ \zeta_x\tau_{yx} + \zeta_y\tau_{yy} + \zeta_z\tau_{yz} \\ \zeta_x\tau_{zx} + \zeta_y\tau_{zy} + \zeta_z\tau_{zz} \\ \zeta_x\beta_x + \zeta_y\beta_y + \zeta_z\beta_z \end{bmatrix} \tag{3.4}$$

where

$$\tau_{xx} = \lambda\left(u_x + v_y + w_z\right) + 2\mu u_x \qquad \tau_{xy} = \tau_{yx} = \mu\left(u_y + v_x\right)$$
$$\tau_{yy} = \lambda\left(u_x + v_y + w_z\right) + 2\mu v_y \qquad \tau_{yz} = \tau_{zy} = \mu\left(v_z + w_y\right)$$
$$\tau_{zz} = \lambda\left(u_x + v_y + w_z\right) + 2\mu w_z \qquad \tau_{xz} = \tau_{zx} = \mu\left(u_z + w_x\right)$$
$$\beta_x = \gamma\kappa Pr^{-1}\partial_x e_1 + u\tau_{xx} + v\tau_{xy} + w\tau_{xz} \qquad \beta_y = \gamma\kappa Pr^{-1}\partial_y e_1 + u\tau_{yx} + v\tau_{yy} + w\tau_{yz}$$
$$\beta_z = \gamma\kappa Pr^{-1}\partial_z e_1 + u\tau_{zx} + v\tau_{zy} + w\tau_{zz} \qquad e_1 = e\rho^{-1} - 0.5\left(u^2 + v^2 + w^2\right)$$

and λ is from Stokes' hypothesis and is $-2/3\mu$, $\mu = \nu/\rho$ is the dynamic viscosity, γ is the ratio of specific heats, κ is the coefficient of thermal conductivity, and Pr is the Prandtl number. The terms u, v, and w are the traditional Cartesian velocity components. As noted in Pulliam and Steger [72], it is understood that the Cartesian derivatives (u_x, v_y, w_z, etc.) are expanded in the curvilinear coordinates using the chain rule as, for example,

$$u_x = \xi_x u_\xi + \eta_x u_\eta + \zeta_x u_\zeta$$

The pressure P term in Eq. 3.2 is defined using the ideal gas law as

$$P = (\gamma - 1)\left[e - 0.5\rho\left(u^2 + v^2 + w^2\right)\right]$$

The transformation derivatives in Eq. 3.3 and Eq. 3.4 are

$$\begin{aligned}
\xi_x &= J\left(y_\eta z_\zeta - y_\zeta z_\eta\right) & \eta_x &= J\left(z_\xi y_\zeta - y_\xi z_\zeta\right) \\
\xi_y &= J\left(z_\eta x_\zeta - x_\eta z_\zeta\right) & \eta_y &= J\left(x_\xi z_\zeta - x_\zeta z_\xi\right) \\
\xi_z &= J\left(x_\eta y_\zeta - y_\eta x_\zeta\right) & \eta_z &= J\left(y_\xi x_\zeta - x_\xi y_\zeta\right) \\
\eta_x &= J\left(y_\xi z_\eta - z_\xi y_\eta\right) & \xi_t &= -x_t\xi_x - y_t\xi_y - z_t\xi_z \\
\eta_y &= J\left(x_\eta z_\xi - x_\xi z_\eta\right) & \eta_t &= -x_t\eta_x - y_t\eta_y - z_t\eta_z \\
\eta_z &= J\left(x_\xi z_\eta - y_\xi x_\eta\right) & \zeta_t &= -x_t\zeta_x - y_t\zeta_y - z_t\zeta_z
\end{aligned}$$

and the Jacobian J from Eq. 3.2 and Eq. 3.4, as well as the spatial transformation derivatives, is given as

$$J^{-1} = x_\xi y_\eta z_\zeta + x_\zeta y_\xi z_\eta + x_\eta y_\zeta z_\xi - x_\xi y_\zeta z_\eta - x_\eta y_\xi z_\zeta - x_\zeta y_\eta z_\xi$$

Flux Calculations

A 5th-order weighted essentially non-oscillatory (WENO) reconstruction scheme [73] with Roe flux-difference splitting [74] was used in the calculations of mean-flow convective fluxes at the computational cell interfaces from Eq. 3.1, which is necessary to develop a continuous flowfield solution using the discontinuous, piecewise data available. Waves running in both directions from both sides of the interface combine to communicate data between the cells. In the ξ direction, Eq. 3.1 can be simplified to a hyperbolic conservation law, which is solved at every cell within the computational domain:

$$\frac{\partial \vec{q}}{\partial t} + \hat{A}\frac{\partial \vec{q}}{\partial \xi} = 0 \tag{3.5}$$

where $\hat{A}$ is the Roe-averaged inviscid flux Jacobian of the conserved variables $\vec{Q}$ and is constant at the cell interfaces. As $\hat{A}$ is solved for using the fluxes of the left- and right-running waves to the right and left of the interface, those must be solved for first using the 5th-order WENO scheme. This high-order solution is achieved by using a sum of three lower-order reconstruction stencils, which have been weighted carefully to minimize oscillations, which can plague higher-order solution techniques in regions of high gradients (e.g. shocks). Using a notation where f_j and $f_{j+\frac{1}{2}}$ indicate the flux value in the current cell and interface respectively, these three lower-order flux reconstructions for the left- and right-running waves are given as [73]

$$\begin{aligned}
\hat{f}^{L1}_{j+\frac{1}{2}} &= \frac{1}{3}f_{j-2} - \frac{7}{6}f_{j-1} + \frac{11}{6}f_j & \qquad \hat{f}^{R1}_{j+\frac{1}{2}} &= \frac{1}{3}f_{j+3} - \frac{7}{6}f_{j+2} + \frac{11}{6}f_{j+1} \\
\hat{f}^{L2}_{j+\frac{1}{2}} &= \frac{-1}{6}f_{j-1} - \frac{5}{6}f_j + \frac{1}{3}f_{j+1} & \qquad \hat{f}^{R2}_{j+\frac{1}{2}} &= \frac{-1}{6}f_{j+2} - \frac{5}{6}f_{j+1} + \frac{1}{3}f_j \\
\hat{f}^{L3}_{j+\frac{1}{2}} &= \frac{1}{3}f_j - \frac{5}{6}f_{j+1} - \frac{1}{6}f_{j+2} & \qquad \hat{f}^{R3}_{j+\frac{1}{2}} &= \frac{1}{3}f_{j+1} - \frac{5}{6}f_j - \frac{1}{6}f_{j-1}
\end{aligned}$$

The reconstruction of the left- and right-running wave fluxes are then

$$f^L_{j+\frac{1}{2}} = \sum_{k=1}^{3} \omega_k \hat{f}^{Lk}_{j+\frac{1}{2}}, \quad f^R_{j+\frac{1}{2}} = \sum_{k=1}^{3} \omega_k \hat{f}^{Rk}_{j+\frac{1}{2}} \tag{3.6}$$

The ω_k terms are normalized, modified weights which are given as

$$\omega_k = \frac{\tilde{\omega}_k}{\sum_{i=1}^{3} \tilde{\omega}_i} \tag{3.7}$$

and

$$\begin{gathered}
\tilde{\omega}_k = \frac{\gamma_k}{(\epsilon + \beta_k)^2} \\
\gamma_1 = \frac{1}{10}, \quad \gamma_2 = \frac{3}{5}, \quad \gamma_3 = \frac{3}{10}
\end{gathered} \tag{3.8}$$

The γ_k terms are the optimal weights for each stencil, and the β_k terms are smoothness indicators shown as

$$\begin{aligned}
\beta_1^L &= \frac{13}{12}\left(f_{j-2} - 2f_{j-1} + f_j\right)^2 + \frac{1}{4}\left(f_{j-2} - 4f_{j-1} + 3f_j\right)^2 \\
\beta_2^L &= \frac{13}{12}\left(f_{j-1} - 2f_j + f_{j+1}\right)^2 + \frac{1}{4}\left(f_{j-1} - f_{j+1}\right)^2 \\
\beta_3^L &= \frac{13}{12}\left(f_j - 2f_{j+1} + f_{j+2}\right)^2 + \frac{1}{4}\left(3f_j - 4f_{j+1} + f_{j+2}\right)^2 \\
\beta_1^R &= \frac{13}{12}\left(f_{j+3} - 2f_{j+2} + f_{j+1}\right)^2 + \frac{1}{4}\left(f_{j+3} - 4f_{j+1} + 3f_{j+1}\right)^2 \\
\beta_2^R &= \frac{13}{12}\left(f_{j+2} - 2f_{j+1} + f_j\right)^2 + \frac{1}{4}\left(f_{j+2} - f_j\right)^2 \\
\beta_3^R &= \frac{13}{12}\left(f_{j+1} - 2f_j + f_{j-1}\right)^2 + \frac{1}{4}\left(3f_{j+1} - 4f_j + f_{j-1}\right)^2
\end{aligned}$$

The normalized, modified weights ω_k from Eq. 3.7 are built such that stencils in smooth regions will approach the optimal weights γ_k and those in regions of large variations are minimized, and the summation of these weights always equals one. The ϵ term in Eq. 3.8 is taken as a small number to avoid dividing by zero.

Once these left- and right-running fluxes have been computed, the Roe-averaged inviscid flux Jacobian $\hat{A}$ may be constructed. This is accomplished first by taking a weighted average of the conserved variables across the interface. In one-dimension these new states are

$$\hat{q}_1 = \hat{\rho} = \sqrt{\rho_L \rho_R}, \quad \hat{q}_2 = \hat{u} = \frac{\sqrt{\rho_L}u_L + \sqrt{\rho_R}u_R}{\sqrt{\rho_L} + \sqrt{\rho_R}}, \quad \hat{q}_3 = \hat{e}_0 = \frac{\sqrt{\rho_L}e_{0_L} + \sqrt{\rho_R}e_{0_R}}{\sqrt{\rho_L} + \sqrt{\rho_R}}$$

This weighted-averaged state $\hat{q}$ is then used to construct a matrix $\hat{T}$, which is the eigenvectors of $\frac{\partial f}{\partial q}$, and $\hat{\Lambda}$, which is the corresponding eigenvalues. $\hat{A}$ is thus computed as

$$\hat{A} = \hat{T}\hat{\Lambda}\hat{T}^{-1}$$

where

$$\hat{T} = \begin{bmatrix} 1 & 1 & 1 \\ \tilde{u} - \tilde{a} & \tilde{a} & \tilde{u} + \tilde{a} \\ \tilde{h}_0 - \tilde{u}\tilde{a} & \frac{1}{2}\tilde{u}^2 & \tilde{h}_0 - \tilde{u}\tilde{a} \end{bmatrix}, \quad \hat{\Lambda} = diag\left(\begin{bmatrix} |\tilde{u} - \tilde{a}| \\ |\tilde{u}| \\ |\tilde{u} + \tilde{a}| \end{bmatrix} \right)$$

$$\tilde{u} = \frac{\hat{q}_2}{\hat{q}_1}$$

$$\tilde{a} = \sqrt{\gamma \frac{\tilde{P}}{\hat{q}_1}}$$

$$\tilde{P} = (\gamma - 1)(\hat{q}_3 - \frac{\hat{q}_2^2}{\hat{q}_1})\tilde{h}_0 = \tilde{e}_0 + \frac{\tilde{P}}{\hat{q}_1}$$

$$\tilde{e}_0 = \frac{\hat{q}_3}{\hat{q}_1}$$

Finally the interface flux can be computed using a linear combination of the left- and right-running wave fluxes about the interface point $j + \frac{1}{2}$ as

$$f^L_{j+\frac{1}{2}} = \frac{1}{2}\left(f_L + f_R\right) - \frac{1}{2}|\hat{A}|\left(q_R - q_L\right) \tag{3.9}$$

for the left interface; the same is done for the right interface. Next, the difference in the final interface fluxes from Eq. 3.9 can be used to update the conserved variables with

$$\Delta q = \frac{f^R_{j+\frac{1}{2}} - f^L_{j+\frac{1}{2}}}{\Delta x}\Delta t$$

Time Discretization

Discretizing and obtain a time-accurate solution of Eq. 3.1 involves assuming a general problem form of $Ax = b$ and solving algebraically and implicitly. The Navier-Stokes equations in Eq. 3.1 can be written implicitly using approximate Jacobians [71, 75] as

$$\left[I + \frac{\Delta t}{(1+\theta)\Delta\tau} + \frac{\Delta t}{1+\theta}\left(\frac{\partial A}{\partial \xi} + \frac{\partial B}{\partial \eta} + \frac{\partial C}{\partial \zeta}\right)\right]\Delta q^{n+1,m+1} = \\ - \left[\left(q^{n+1,m} - q^n\right) - \frac{\theta}{1+\theta}\Delta q^n + \frac{\Delta t}{1+\theta}RHS^{n+1,m}\right] \tag{3.10}$$

where Δt is the chosen time-step, τ is a pseudo time-step which allows the local time-step ($\Delta\tau$) to vary at any point in the domain, and θ is a variable that can take either a value of 0 for first-order time marching or 1/2 for second-order time marching. The second term in the brackets on the left-hand-side of Eq. 3.10 is an artificial time term added for dual time stepping [76], and is dropped when performing Newton subiterations. The RHS term is all of the flux terms of Eq. 3.1, or the right-hand-side of the Navier-Stokes equations. The $\Delta q^{n,m}$ term is the change in the conserved variables, and is computed for each time-step n and for a predetermined number of subiterations m. If dual time-stepping is used ($\Delta\tau \neq \Delta t$), the artificial time term must converge at each physical time step to ensure time accuracy.

There are several options available for solving the left-hand side of Eq. 3.10 (represented by the matrix A in the general form assumed) by approximately factoring it in space, as direct inversion for large systems is computationally expensive and time consuming. The error associated with this approximate factorization scales with the time-step cubed for three-dimensional problems, and is thus generally ignored. The method used to accomplish the factorization in this work was the diagonalized, diagonally dominant alternating direction implicit (D3ADI) scheme [77]. The inviscid flux Jacobians seen in Eq. 3.10 can first be decomposed into their eigenvalues and eigenvectors as

$$
\begin{aligned}
A &= \frac{\partial E}{\partial q} = X_A \Lambda_A X_A^{-1} \\
B &= \frac{\partial F}{\partial q} = X_B \Lambda_B X_B^{-1} \\
C &= \frac{\partial G}{\partial q} = X_C \Lambda_C X_C^{-1}
\end{aligned}
$$

The diagonal alternating direction implicit (DADI) scheme [78] then uses these to factor Eq. 3.10 as

$$X_A\left[I+\frac{\Delta t}{1+\theta}\delta_\xi\Lambda_A\right]X_A^{-1}X_B\left[I+\frac{\Delta t}{1+\theta}\delta_\eta\Lambda_B\right]X_B^{-1}X_C\left[I+\frac{\Delta t}{1+\theta}\delta_\zeta\Lambda_C\right]X_C^{-1}\Delta q^{n+1,m+1}=$$
$$-\left[\left(q^{n+1,m}-q^n\right)-\frac{\theta}{1+\theta}\Delta q^n+\frac{\Delta t}{1+\theta}RHS^{n+1,m}\right] \quad (3.11)$$

Separating Eq. 3.11 into diagonal and off-diagonal terms, factoring the scheme, then diagonalizing, the D3ADI scheme can be obtained and is given as

$$X_A\left[I+\frac{\Delta t}{1+\theta}\delta_\xi^u\Lambda_A+X_A^{-1}\left(D_\eta+D_\zeta\right)X_A\right]X_A^{-1}D^{-1}$$
$$X_B\left[I+\frac{\Delta t}{1+\theta}\delta_\eta^u\Lambda_B+X_B^{-1}\left(D_\xi+D_\zeta\right)X_B\right]X_B^{-1}D^{-1}$$
$$X_C\left[I+\frac{\Delta t}{1+\theta}\delta_\zeta^u\Lambda_C+X_C^{-1}\left(D_\xi+D_\eta\right)X_C\right]X_C^{-1}\Delta q^{n+1,m+1}=$$
$$-\left[\left(q^{n+1,m}-q^n\right)-\frac{\theta}{1+\theta}\Delta q^n+\frac{\Delta t}{1+\theta}RHS^{n+1,m}\right]$$

where D is a matrix containing all of the diagonal terms of Eq. 3.11 and δ^u is a differencing operator, which can be either forward or backward based on the sign of the eigenvalues Λ.

Turbulence Modeling

The Spalart- Allmaras (SA) model [79], specifically the SA-neg-noft2 variant [75, 80], was used for turbulence modeling with delayed, detached eddy simulation (DDES) [81] and rotation/curvature (RC) correction [82] enabled. The base Spalart-Allmaras eddy viscosity model is a one-equation turbulence model which computes the transport of the working variable $\tilde{\nu}$. The Reynolds stresses are evaluated using the Boussinesq approximation of eddy viscosity ν_t,

$$\nu_t=\tilde{\nu}f_{v1},\quad f_{v1}=\frac{\chi^3}{\chi^3+c_{v1}^3},\quad \chi\equiv\frac{\tilde{\nu}}{\nu} \quad (3.12)$$

where ν is the kinematic viscosity and χ is a turbulent Reynolds number. The SA model working variable obeys the transport equation

$$\frac{D\tilde{\nu}}{Dt} = P - D + \frac{1}{\sigma}\left[\nabla \cdot ((\nu + \tilde{\nu})\nabla\tilde{\nu}) + c_{b2}\left(\nabla\tilde{\nu}\right)^2\right] \tag{3.13}$$

where

$$P = c_{b1}\tilde{S}\tilde{\nu}, \quad D = c_{w1}f_w\left(\frac{\tilde{\nu}}{d}\right)^2 \tag{3.14}$$

are the production and wall destruction terms, respectively. $\tilde{S}$ is the modified vorticity given as

$$\tilde{S} = S + \frac{\tilde{\nu}}{\kappa^2 d^2}f_{v2}, \quad f_{v2} = 1 - \frac{\chi}{1 + \chi f_{v1}}$$

Here S is the vorticity magnitude and d is the distance to the closest wall. The function f_w from Eq. 3.14 is defined as

$$f_w = g\left[\frac{1 + c_{w3}^6}{g^6 + c_{w3}^6}\right]^{1/6}, \quad g = r + c_{w2}\left(r^6 - r\right), \quad r = min\left(\frac{\tilde{\nu}}{\tilde{S}\kappa^2 d^2}, r_{lim}\right)$$

The remaining terms are carefully calibrated constants and are defined as

$$c_{b1} = 0.1355 \qquad \sigma = \frac{2}{3}$$

$$c_{b2} = 0.622 \qquad \kappa = 0.41$$

$$c_{w1} = \frac{c_{b1}}{\kappa^2} + \frac{1 + c_{b2}}{\sigma} \qquad r_{lim} = 10$$

$$c_{w2} = 0.3 \qquad c_{w3} = 2$$

Note that κ is the Kármán constant here. To account for rotation and curvature effects, which are particularly important for rotation-dominated flows such as rotor hub wakes, the rotation/curvature correction developed by Shur et al. [82] was applied. This correction modifies the SA-neg-noft2 model by multiplying the turbulence production term P of Eq. 3.14 by

$$f_{r1} = (1 + c_{r1}) \frac{2r^*}{1 + r^*} \left[1 - c_{r3} tan^{-1} (c_{r2} \tilde{r})\right] - c_{r1}$$

where

$$r^* = \frac{S}{\omega}$$
$$\tilde{r} = \frac{2\omega_{ik} S_{ik}}{D^4} \left(\frac{\mathrm{D}S_{ij}}{\mathrm{D}t} + (\epsilon_{imn} S_{jn} + \epsilon_{jmn} S_{in}) \Omega_m \right)$$

Here the flow-field-related terms are given as

$$S = \sqrt{2 S_{ij} S_{ij}}, \quad S_{ij} = \frac{1}{2} \left(\frac{\partial u_i}{\partial x_j} + \frac{\partial u_j}{\partial x_i} \right)$$
$$\omega = \sqrt{2 \omega_{ij} \omega_{ij}}, \quad \omega_{ij} = \frac{1}{2} \left[\left(\frac{\partial u_i}{\partial x_j} - \frac{\partial u_j}{\partial x_i} \right) + 2 \epsilon_{mji} \Omega_m \right]$$
$$D = \sqrt{\frac{1}{2} (S^2 + \omega^2)}$$

where S_{ij} are the components of the mean strain tensor, ω_{ij} are the components of the vorticity tensor, ϵ_{jmn} is the Levi-Civita tensor, Ω_m are the components of the system rotational rate vector, and the $\mathrm{D}S_{ij}/\mathrm{D}t$ is the substantial derivative of S_{ij}. The calibrated constants are

$$c_{r1} = 1.0, \quad c_{r2} = 12.0, \quad c_{r3} = 1.0$$

Delayed Detached Eddy Simulation

As turbulent rotor hub wakes are intrinsically dominated by relatively small length scales, the use of turbulent models such as the SA-neg-noft2 model in the far wake tends to become ineffective due to its reliance on the length scale d. Thus it lends itself to use a hybrid system of RANS within the attached boundary layer and Large Eddy Simulation (LES) in regions of separation and areas away from the wall. LES is a filtered direct numerical solution (DNS)

of the Navier-Stokes equations, where the smallest turbulence scales are filtered using a low-pass filter to reduce computational expense. To accomplish this, DDES [81] incorporates a modified length scale $\tilde{d}$ which explicitly replaces the length scale d in the Spalart-Allmaras model:

$$\tilde{d} = d - f_d max(0, d - C_{DES}\Delta)$$

where

$$f_d = 1 - tanh\left([8r_d]^3\right), \quad r_d = \frac{\nu_t + \nu}{\sqrt{U_{i,j}U_{i,j}}\kappa^2 d^2}$$

Here $U_{i,j}$ are the velocity gradients, $C_{DES} = 0.65$, and Δ is the magnitude of the longest dimension of the current grid cell. The function f_d acts as a "shielding" function and is designed to equal 1 in LES regions of the flow, and r_d is the ratio of a characteristic turbulence model length scale to wall-distance length scale.

3.2.2 Grid Generation and Connectivity

The computational grids used in this study were structured, overset grids developed and provided by Penn State University Applied Research Laboratory (PSU-ARL), which were modified as described in Wall [11] using the Chimera Grid Tools software [83]. Overset grids consist of two groups of volume grids: near-body grids and off-body grids. Near-body grids are grids which are attached to the geometry of interest, and are extrusions of the surface grids. These grids can be developed in Chimera grid tools or in other software such as Pointwise. Off-body grids are Cartesian, layered grids which are steadily reduced in resolution as they grow further out into the far-field of the domain. In the case of OVERFLOW, these off-body grids are automatically built before the simulation is started, based on inputs describing the off-body grid closest to the geometry or area of interest. As OVERFLOW is a finite-difference solver [71], structured grids were required.

Surface grids as well as cross-sections of the near-body grids of the blade stubs and the off-body grids are shown in Figs. 24-27. As mentioned, the surface and near-body grids for the Baseline, Defeatured, and Low Drag hubs were provided by PSU-ARL. To develop

the free-air Phase III hub grid, structured surface grids of the circular indent feature were first created in Pointwise v18.3R2 then incorporated into a new copy of the Baseline hub grid using the Chimera Grid Tools software. Off-body Cartesian grids were generated using the OVERFLOW 2.2n solver [71], and for all geometries the nearest off-body grid had a constant spacing of 0.25 inches (approximately $0.01D_{hub}$) and extended approximately 4 hub diameters downstream. The off-body grid built around the Baseline hub is shown in Fig. 24c with measurements added for context; the other hubs' off-body grids had the same measurements. The nearest off-body refinement region is vertically centered 5 inches (approximately $0.21D_{hub}$) above every hub except the Low Drag hub, to ensure the entire wake content is captured. The far-field extends 1000 inches (approximately $41.65D_{hub}$) in every direction. The total grid points for each hub geometry are summarized in Table 1. Predefined cutters [84] and the XRAYS routine built into Chimera Grid Tools were used to facilitate overset domain connectivity. In order to facilitate the use of the higher-order WENO stencil and attain proper flux reconstruction, three fringe (overlap) layers were used. The Baseline, Defeatured, and Phase III hubs were positioned at $y = -5$ inches with respect to the off-body grids to ensure that the hub wake was captured adequately (Figs. 24, 25, & 27).

3.2.3 Simulation Inputs and Boundary Conditions

The simulations of the four hubs were conducted with the hub at a rotor shaft angle of 5 degrees into the flow and a Reynolds number of 4.6×10^6 using the hub diameter D_{hub} of 24 inches as the characteristic length. A free stream Mach number of 0.1 was used, and the hubs were rotated at 800 rpm based on a full rotor advance ratio μ of 0.2. The hubs were assumed to make up 15% of the full-rotor diameter, therefore the hubs' advance ratio was $\mu_{hub} \approx 1.33$. Sea-level conditions were applied for air properties. Solutions were run in three stages. First, dual-time stepping with pseudo time-steps was used for the first 4 revolutions, to setup the flow field and advect startup transients. Then, the simulations were switched to a global time stepping method with 30 Newton-type sub-iterations. All simulations were run for at least 20 rotor hub revolutions before data sampling began. For the Baseline, Defeatured, and Low Drag hubs, simulations were started from restarts provided by Tristan Wall from

previous work documented in Wall and Coder [67] and Wall [11]. The physical time step used corresponded to 0.25 degrees of hub rotation in the azimuthal plane. The free-stream Spalart-Allmaras variable $\tilde{\nu}$ was set to 0.1. This value is lower than the "standard" value of 3 for fully turbulent flows [85], but has been found to be well-suited from previous work with these rotor hubs [11].

The rotor hubs' surface boundary conditions were set to a viscous, adiabatic no-slip condition, and the far-field boundary conditions were set to the default Riemann characteristic inflow/outflow [71]. Force and moment calculations were handled using USURP [86], which is an algorithm capable of computing accurate force and moments from cell-centered, overset grid simulations.

3.3 Post-processing Background and Methods

Data of residual and force time histories were exported from the simulation output files using Chimera Grid Tools [83], and plots of these histories were made using MATLAB [87]. Data manipulation, processing, and field visualization were handled with a combination of MATLAB and FieldView 21 [88].

3.3.1 Turbulent Kinetic Energy and Reynolds Stresses

An analysis of the turbulent kinetic energy (TKE) and associated Reynolds stress terms was used in this work to gain a better understanding of the turbulent behavior of the rotor hub wakes. A derivation of the Reynolds averaged Navier-Stokes equations is helpful for understanding these quantities and is provided here. Another way to write the incompressible Navier-Stokes equations shown in Eq. 3.1 is

$$\frac{\partial u_i}{\partial t} + u_j \frac{\partial u_i}{\partial x_j} = -\frac{1}{\rho}\frac{\partial p}{\partial x_i} + \nu \frac{\partial u_i}{\partial x_j \partial x_j} \tag{3.15}$$

The continuity equation is similarly

$$\frac{\partial u_j}{\partial x_j} = 0 \tag{3.16}$$

The Reynolds decomposition [89] represents the velocity vector component $u_i(x_i, t)$ as a sum of the mean of the velocity component and a perturbation of that velocity component about the mean:

$$u_i(x_i, t) = \overline{u}_i(x_i) + u'_i(x_i, t)$$

Note that the mean of the velocity is the time-averaged velocity component which is written as

$$\overline{u}_i(x_i) = \lim_{T\to\infty} \frac{1}{T} \int_0^T u_i(x_i, t)\mathrm{d}t \tag{3.17}$$

where T is the time interval over which the velocity is averaged, and must be much greater than the typical time scale of the perturbation term. It then follows that by averaging the velocity, the perturbation term goes to 0. Applying this Reynolds averaging to the continuity equation (Eq. 3.16) gives [90, 91]

$$\frac{\partial \overline{u}_j}{\partial x_j}$$

Taking the Reynolds average of the momentum equations and applying some simplifications using decomposition [91] yields the Reynolds averaged Navier-Stokes equations,

$$\frac{\partial \overline{u}_i}{\partial t} + \overline{u}_j \frac{\partial \overline{u}_i}{\partial x_j} = -\frac{1}{\rho}\frac{\partial \overline{p}}{\partial x_i} + \nu \frac{\partial \overline{u}_i}{\partial x_j \partial x_j} - \frac{\partial \overline{u'_i u'_j}}{\partial x_j} \tag{3.18}$$

Note the additional term which has appeared on the right hand side. Equation 3.18 can be rewritten as

$$\rho\left(\frac{\partial \overline{u}_i}{\partial t} + \overline{u}_j \frac{\partial \overline{u}_i}{\partial x_j}\right) = \frac{\partial}{\partial x_j}\left[-\overline{p}\delta_{ij} + \mu\left(\frac{\partial \overline{u}_i}{\partial x_j} + \frac{\partial \overline{u}_j}{\partial x_i}\right) - \rho\overline{u'_i u'_j}\right]$$

where δ_{ij} is the Kronecker delta, and the terms in the square brackets are the stresses from pressure, viscosity, and the velocity perturbations. The $-\rho\overline{u'_i u'_j}$ term is known as the Reynolds stresses (for this work, this term will be simplified to $\overline{u'_i u'_j}$). The Reynolds stress term is a symmetric second-order tensor with normal stresses occupying the diagonal and shear stresses occupying the off-diagonal components. Turbulent kinetic energy k is half of

the trace of the Reynolds stress tensor (taking into account the simplification to the Reynolds stresses mentioned),

$$k = \frac{1}{2}\overline{u_i' u_i'} \tag{3.19}$$

An equation describing the evolution of k can be derived [91] by first multiplying Eq. 3.15 by u_i and taking the average of the resulting equation,

$$\overline{\frac{\partial u_i}{\partial t} u_i} + \overline{u_j \frac{\partial u_i}{\partial x_j} u_i} = -\frac{1}{\rho}\overline{\frac{\partial p}{\partial x_i} u_i} + \nu \overline{u_i \nabla^2 u_i} \tag{3.20}$$

Subsequently multiplying Eq. 3.18 by $\overline{u}_i$ provides

$$\frac{\partial \overline{u}_i}{\partial t}\overline{u}_i + \overline{u}_j \frac{\partial \overline{u}_i}{\partial x_j}\overline{u}_i = -\frac{\partial \overline{u_i' u_j'}}{\partial x_j}\overline{u}_i - \frac{1}{\rho}\frac{\partial \overline{p}}{\partial x_i}\overline{u}_i + \nu \overline{u}_i \overline{\nabla^2 u_i} \tag{3.21}$$

Subtracting Eq. 3.21 from Eq. 3.20 gives

$$\rho \overline{\frac{\partial u_i'}{\partial t} u_i'} + \rho\left(\overline{u}_j \frac{\partial \overline{u}_i}{\partial x_j} - \overline{u}_j \frac{\partial \overline{u}_i}{\partial x_j}\overline{u}_i\right) = -\overline{\frac{\partial p'}{\partial x_i} u_i'} + \nu \overline{u_i' \nabla^2 u_i'} + \rho \frac{\partial \overline{u_i' u_j'}}{\partial x_j}\overline{u}_i \tag{3.22}$$

Through averaging rules, simplifications, and substituting the definition of k in Eq. 3.19, the equation for TKE in an incompressible flow can be shown to be [91],

$$\frac{\partial k}{\partial t} + \overline{u}_j \frac{\partial k}{\partial x_j} = -\frac{\partial}{\partial x_j}\left(\frac{1}{2}\overline{u_i' u_i' u_j'} + \frac{1}{\rho}\overline{u_j' p'} - \nu \frac{\partial k}{\partial x_j}\right) - \overline{u_j' u_i'}\frac{\partial \overline{u_j}}{\partial x_i} - \nu \overline{\frac{\partial u_i'}{\partial x_j}\frac{\partial u_i'}{\partial x_j}} \tag{3.23}$$

where the left hand side of the equation is the material derivative of k. The first term on the right hand side is the total transport of TKE, and consists of three parts. The first term in the transport term is the turbulent transport, signifying the transport of TKE via velocity fluctuations. The second and third terms are the pressure diffusion and viscous diffusion terms, respectively. The second term on the right hand side is the production term, signifying the transfer of energy from the mean flow into the turbulent flow. The last term on the right hand side is the dissipation rate of TKE, and is generally denoted as ϵ. For this

work, a focus was put on the turbulent transport and production terms on the right hand side.

3.3.2 Proper Orthogonal Decomposition

Proper orthogonal decomposition (POD) was also used to analyze the modal behavior of the instantaneous Reynolds stresses in the rotor hub wake. POD is a method which seeks to optimize the mean square of the flow-field variable it is being applied to and find the optimal basis, and represents that variable as a set of orthogonal modes. These modes can then be examined individually or combined with the mean of the data set to perform a flow-field reconstruction. POD and other decomposition methods have been applied to rotor hub wake flows in the past [11] to reveal coherent structures in the wake. The modern POD process is summarized here, and this discussion is based on the work in Taira et al. [92]. Starting with a given set of snapshots (time steps) of a vector field $q(\xi, t)$, where ξ represents a generic spatial coordinate system, the time-averaged mean $\overline{q}(\xi)$ is first subtracted. The perturbation component is then assumed to be decomposable as,

$$q(\xi, t) - \overline{q}(\xi) = \sum_j a_j(t)\phi_j(\xi)$$

where $a_j(t)$ and $\phi_j(\xi)$ are the expansion coefficients and the orthogonal modes, respectively. To solve this problem, the left hand side of this equation is first represented as,

$$x(t_i) = q(\xi, t) - \overline{q}(\xi) \in \mathbb{R}^n, \quad i = 1, 2, 3, \ldots, m$$

where $x(t_i)$ represents the entire spatial domain of a single time step t_i. An eigenvalue problem can then be constructed using the covariance matrix R of $x(t_i)$:

$$R\phi_j = \lambda_j \phi_j$$
$$R = \sum_{i=1}^{m} x(t_i)x^T(t_i) = XX^T \in \mathbb{R}^{n \times n}$$

Here λ_j and ϕ_j are the eigenvalues and eigenvectors, respectively. The matrix X is the set of m snapshots combined into a matrix, and each of these time steps has n spatial degrees of freedom. The eigenvectors ϕ_j solved in this problem are the POD modes, and the eigenvalues represent how well each eigenvector captures the original data set. Larger eigenvalues correspond to the eigenvector or mode capturing a greater portion of the data set's behavior.

With large fluid simulations, the spatial degrees of freedom n can become prohibitively large, making the covariance matrix and subsequent eigenvalue problem computationally expensive or not feasible. Fortunately, a method of avoiding this cost exists in the use of the temporal correlation matrix defined as $X^T X \in \mathbb{R}^{m \times m}$, and the eigenvalue problem can be rewritten as

$$X^T X \psi_j = \lambda \psi_j, \quad \psi_j \in \mathbb{R}^m, \quad m \ll n$$

and the original POD modes can be recovered through

$$\phi_j = X \psi_j \frac{1}{\sqrt{\lambda_j}}, \quad j = 1, 2, \ldots, m$$

To solve this eigenvalue problem, it is convenient to employ the singular value decomposition (SVD). The data matrix X can be decomposed using SVD into the left and right singular matrices:

$$X = \Phi \Sigma \Psi^T$$

where $\Phi \in \mathbb{R}^{n \times n}$, $\Sigma \in \mathbb{R}^{n \times m}$, and $\Psi \in \mathbb{R}^{m \times m}$. The Φ and Ψ matrices contain the eigenvectors of XX^T and $X^T X$, respectively, and the singular values σ_j contained in the diagonal of Σ are related to the eigenvalues λ_j by $\sigma_j^2 = \lambda_j$. Conveniently, the modes are automatically ordered by their corresponding eigenvalues, with the largest eigenvalue occupying the first index of Σ.

Chapter 4: Results

As noted previously, all of the rotor hubs were run for at least 20 revolutions before flow-field data was recorded. Surface forces were recorded throughout the simulations. To reduce the computational cost of post-processing, planes of data in the wake with normals oriented parallel to the free stream were exported instead of the entire wake. These planes were positioned at $x = D_{hub}$, $x = 1.5D_{hub}$, ..., $x = 3.5D_{hub}$. These results have been extended from results previously published in Mobley et al. [93] or from those which have been accepted for publication in the Journal of the American Helicopter Society [94].

4.1 Instantaneous Wake Capture and Surface Forces

Examples of the instantaneous wake captured by the nearest off-body grid are shown in Fig. 28, with flow going from left to right. Vertical lines have been added to the figures to indicate the near ($x = D_{hub}$) and far ($x = 3.5D_{hub}$) wake coordinates. Throughout the wake eddies of various sizes can be seen, indicating that turbulent structures have been captured throughout the wake. When comparing these against those in Potsdam and Cross [62], it is apparent that the vertical extent of the wakes is different. This is due to the presence of the water tunnel pylon, which was included to coincide with the experimental portion of the ongoing work mentioned previously [68–70].

Time-averaged surface forces of all of the simulated hubs in the form of effective flat plate areas D/q and L/q are summarized in Table 2, with the reference area $A_{ref} = 1\text{in}^2$. The data for the simulated hubs were recorded at every 2.5 degrees of rotor hub rotation and averaged over 16 rotor hub revolutions. The D/q for the experimental tests that the Phase III hub was based on is also reported for comparison and is from Wall [11]. The Baseline and Phase III hubs have the highest D/q values, which is expected considering their increased projected frontal area compared to the other hubs. The Defeatured and Low Drag hubs have lower D/q values, and interestingly the Low Drag hub has a much lower D/q value despite having the same projected frontal area as the Defeatured hub [11]. The hubs also produce a download as seen in the L/q values, with the Low Drag hub having the most substantial

effect. The increase in magnitude for the Low Drag hub is due to the more aerodynamic geometry, particularly when comparing the hubs' blade stubs. There is a discrepancy in the L/q values between the Baseline and Phase III hubs, and the reason for these is not apparent from the data. However, due to the relatively low values of L/q compared to the D/q values for these hubs, the discrepancy is most likely statistically insignificant. Phase-averaged effective flat plate areas are shown in Fig. 29, and correspond to similar figures shown in Wall [11]. The phase-averaged D/q values shown in Fig. 29a show a clear 4/rev frequency, corresponding to the overall symmetry of the hubs, with peaks occurring at the positions of greatest projected frontal area ($\Psi = 90°$, $\Psi = 180°$, and $\Psi = 270°$). Of note are the results for the Low Drag hub, whose peaks seem to occur slightly after these points of greatest frontal area. The phase-averaged L/q behavior illustrated in Fig. 29b is more complex, particularly for the Baseline and Phase III hubs which do not show a clear 4/rev frequency. The Defeatured and Low Drag hubs do show an apparent 4/rev frequency, with peaks lagging the $\Psi = 90°$, $\Psi = 180°$, and $\Psi = 270°$ azimuthal positions.

A spectral analysis of the effective flat plate areas of the four hubs was performed, and results are shown in Fig. 30. The FFT was performed using 16 revolutions of data, starting from the beginning of revolution 9. Starting with the drag results plotted in Fig. 30a, the most dominant frequency is the 4/rev, due to the symmetry of the blade stubs on the rotor hubs. The 2/rev frequency also has a strong presence in the case of the Baseline hub and Phase III hub, and this is from the additional 2/rev symmetry of the scissor arms shown in Fig. 22. For these two cases, there is an unexpectedly large difference between the magnitudes of the 2/rev frequency content. Unsurprisingly, beyond the 4/rev frequency, frequency content is diminished for all of the rotor hubs. For the lifting forces depicted in Fig. 30b, the 4/rev frequency again dominates. However, the Low Drag hub case shows increased frequency content for this frequency as well as for 8/rev and 12/rev. The increased content in the higher frequencies is most likely a result of the Low Drag hub's blade stubs, which had a greater effect on the rotor hub's lift due to their shape. The magnitudes shown for the 4/rev frequency are shown in Table 2 and match well with the lift trends shown in the time-averaged flat plate areas. A similar analysis is included in Wall [11]. The significant differences in magnitudes between the Baseline and Phase III hubs in the 2/rev frequency

in both the D/q and L/q could be an indication that these data are not yet converged (as these hubs are nearly identical geometrically), however this could also be an indication of noise present in the data.

4.2 Time-Averaged Velocity Profiles

Six constant-x planes of the domain, positioned at $x = D_{hub}$, $1.5D_{hub}$, $\ldots, 3.5D_{hub}$, were exported at every time-step for 5 revolutions of rotor hub rotation, starting from revolution 20. Time-averaged velocity components were computed using the Phase III hub for comparison against experimental results at the $x = D_{hub}$ coordinate, and are shown in Fig. 31. Experimental results were provided by PSU-ARL using the Phase III hub geometry based on the hub shown in Fig. 22. All plots are shown with the hub upstream, advancing side on the right, and free-stream flow coming out of the page. Stream-wise (u) velocity contours show a bias towards the advancing side, for both experimental and CFD cases. This was also observed in Reich et al. [61], which performed similar experiments at $Re_{hub} = 1.8 \times 10^6$, where the lateral bias in the wake was explained to be due to the Magnus effect. In the CFD results, a loose association between the stream-wise velocity deficit and the geometry can be seen, with the strongest areas being concentrated near the upper and lower spiders and the scissor arms. A similar deficit can be seen in the experimental results, however it is more concentrated in one area and is positioned lower towards the scissor arms and swash plate. A comparable result was noted in Reich et al. [61], and the overall discrepancy between the CFD and experimental results is most likely due to the simulated rotor hubs being in free air rather than installed in a tunnel with a mounting pylon. The vertical (w) velocity contours show some differences as well, with the experimental results displaying a moderate downwash above the hub and an upwash on the retreating side near the top spider. The CFD results plotted in Fig. 31d show a strong upwash nearly centered with the hub. The strong upwash in the CFD results is again most likely due to the lack of the pylon holding the hub in place, as well as the -5° angle of attack of the hub.

The mean velocity profiles in each constant-x plane at the $y = 0$ coordinate for each rotor hub simulated in this study are shown in Figs. 32-34. Horizontal dashed lines are also

included to indicate the vertical limits of the tip path plane of the blade arms. A portion of the Baseline hub's mean velocity profile data was used and presented in Schmitz et al. [70] for comparison against experimental results. The stream-wise velocity profiles are shown in Fig. 32, and every case shows an upward movement of the wake centerline. For the Baseline hub and Phase III hub, this correlates with the vertical velocity contours shown in Fig. 31d. This trend is consistent with the vertical velocity profiles shown in Fig. 34, which show a positive vertical velocity for every hub. Experimental stream-wise velocity results from Schmitz et al. [68] are shown in Fig. 32d, which show a large deficit positioned below the projected tip path plane. By isolating the rotor hub from the water tunnel and pylon, the velocity deficit has been significantly reduced, as well as shifted up vertically. This holds true up to the far wake ($x = 3.5D_{hub}$) coordinate. The Low Drag hub velocity profiles plotted in Fig. 32c show a substantially smaller stream-wise velocity deficit, which is an indication of the improved aerodynamic design compared to the other hubs.

The mean span-wise velocity profiles are shown in Fig. 33. Due to the dominant stream-wise component of the free-stream velocity, variations in the mean span-wise velocity are much smaller, and each case reaches a steady state within the profiles by the $x = 2D_{hub}$ or $x = 2.5D_{hub}$ coordinate. All of the profiles show a varying degree of skew symmetry with the coordinate closest to the hub showing the most prominent. This is an expected behavior given the -5° angle of attack.

The mean vertical velocity profiles for the hubs are shown in Fig. 34, which all have the upwash seen in the corresponding contours for the Baseline hub shown in Fig. 31d. The Baseline and Phase III hubs have the strongest upwash, and overall their profiles appear nearly equivalent. Surprisingly, the Defeatured and Low Drag hub profiles are similar in shape and magnitude, as opposed to the frequency content of these hubs plotted in Figs. 29-30. The Defeatured hub's weaker profiles indicate the effect that the swashplate and the scissor arms have on the vertical velocity, which are only present in the Baseline and Phase III hubs' geometries.

4.3 Frequency Content of Velocity Profiles

Frequency content of the velocity field was also computed using discrete Fourier transforms (DFT). Data was collected at several points in the $x = D_{hub}$ and $x = 3.5D_{hub}$ planes at $y = 0$ (Fig. 35) for comparison against particle image velocimetry (PIV) results as documented in Reich et al. [60]. In the near wake ($x = D_{hub}$), the CFD results show significantly greater 2/rev content than the experimental results, and this is also the case for the far wake ($x = 3.5D_{hub}$). The 4/rev content in general seems to be better predicted, and in some points matches closely to the experimental results. The overall frequency profiles show the same trends in the near wake, however the far wake results in general are stronger.

Amplitude contours for all rotor hub geometries at $x = D_{hub}$ for the u- and w-velocity components are shown in Figs. 36-37. Outlines of the rotor hubs are overlaid to show the positions of particular features in relation to the hubs' geometric features. All figures are shown with the hub upstream, with flow coming out of the page, and the advancing side on the right. Shown in Fig. 36, 2/rev fluctuations are present in the Baseline hub (Fig. 36a) and the Phase III hub (Fig. 36d) results. These fluctuations are near the spiders on the retreating side and near the swashplate on the advancing side. These same fluctuations are noticeably damped from the Defeatured hub (Fig. 36b) and the Low Drag hub (Fig. 36c). Fluctuations of the same frequency in the w-velocity, depicted in Fig. 37, are relatively low in amplitude for all rotor hub geometries. These results match well with results found in Wall and Coder [67], which found higher 2/rev content in the frequency content of the rotor hub drag results for the Baseline hub than for the Defeatured and Low Drag hubs. Similar trends in the stream-wise velocity fluctuations were also detailed in Reich et al. [61]. Since the scissors are the only geometric feature on the hubs that have a 2/rev symmetry, it is logical to conclude that this feature is the source of this frequency content. This was also found in Wall and Coder [67], and higher amplitudes of content at this frequency were found to be attributed to the scissor arms and swashplate in Potsdam and Cross [62] and Potsdam and Sitaraman [64].

Strong 4/rev fluctuations can be seen for both velocity components in every hubs' results, as expected with the 4/rev symmetry inherent in the geometries. A general bias towards the

retreating side can be seen in most results, with the exception of the w-velocity fluctuations of the Low Drag hub (Fig. 37c). For the Baseline and Phase III hubs, distinct areas of large u-velocity fluctuations can be seen near the scissor arms and swashplate, and similar regions are apparent near the spiders and blades for all hub geometries. Higher frequency content overall is lacking, with no distinct patterns or large amplitude areas. The only noticeable exception to this is the 8/rev fluctuations of the w-velocity component for the Low Drag Hub (Fig. 37c). This is also consistent with the results reported in Wall and Coder [67]. The 6/rev fluctuations present in rotor hub wake flow have been hypothesized to be a consequence of either Strouhal shedding from the junction between the spiders and blade stubs, or from a non-linear interaction between 2/rev and 4/rev fluctuations [61]. The increased 6/rev content in the Baseline and Phase III hubs' results is an indication that the latter hypothesis is correct, due to the lack of scissor arms seeming to lead to reduced 6/rev fluctuations. The CFD results in general seem to have under-predicted higher frequency harmonic content than that reported in experimental work, such as in Berry [52] and Reich et al. [61]. Similar under-predictions were found in Potsdam and Cross [62], and were attributed to the seemingly excessive diffusivity of the off-body grid and/or the solver settings used to capture wake behavior between the near ($x = D_{hub}$) and far ($x = 3.5D_{hub}$) coordinates.

Another noteworthy aspect of these results is the general bias of larger magnitude harmonics previously mentioned, with areas of high magnitudes being concentrated on the retreating side of the rotor hubs. This feature in the data, as discussed in Reich et al. [61], seems to be associated with the higher apparent velocity on the advancing side of the hub. Although this bias is apparent in the frequency analysis results for most of the hubs, the Low Drag hub results show a bias slightly less overwhelming in the u-velocity harmonics and much less apparent in the w-velocity harmonics. This suggests that this bias is affected by geometry as well. Due to the aerodynamic geometry of the blade arms of the Low Drag hub, the lifting forces produced by the hub (Table 2) likely had a greater effect on the w-velocity in the flow field. This hypothesis is also supported by the results in Wall and Coder [67], which showed higher lift fluctuation amplitude content from the Low Drag hub in the 4/rev and 8/rev harmonics than those of the Baseline and Defeatured hubs.

4.4 Turbulent Kinetic Energy

4.4.1 Reynolds Stresses

Due to the low Mach number of the simulations, near-incompressibility was assumed and density variations were ignored in the Reynolds stress and TKE budget terms. Reynolds stresses were computed by first building $\overline{u_i u_j}$ then subtracting the quantity $\overline{u_i}\ \overline{u_j}$, using data recorded at every time-step for rotor hub revolutions. To confirm that the turbulence model used and the off-body grid resolution were adequate to resolve the Reynolds stresses, the power spectral density (PSD) of the stream-wise momentum was estimated using a fast Fourier transform (FFT) algorithm. This was estimated at a point on the advancing side within the tip path plane of the rotor hub, at the $x = D_{hub}$, $x = 2D_{hub}$, and $x = 3D_{hub}$ coordinates in the Baseline hub wake, using data recorded at every time step for 5 rotor revolutions. The PSD for this data is plotted in Fig. 38, and a line with a slope of $f^{-5/3}$ is provided as a reference. At every coordinate where it was calculated, the estimated PSD shows an energy cascade with the appropriate slope before the higher frequencies are damped out. As the other rotor hubs were simulated using the same turbulence modeling and off-body grids, the same behavior can be expected to be present in the other rotor hub wakes. Peaks at the expected frequencies such as 2/rev and 4/rev are not clearly distinguishable in this data, which is most likely an indication of noise in the data.

Reynolds stress components were also computed using several different bins of data of the Baseline hub. These bins corresponded to 1, 2, 3, 4, and 5 revolutions worth of data, and were used to check for convergence (these are referred to as bins 1, 2, 3, 4, and 5, respectively). Vertical profiles of two Reynold stress components located at $y = 0$ and $x = D_{hub}$ are shown in Fig. 39. The normal component $\overline{u'u'}$, shown in Fig. 39a, shows very little variation between the profiles overall. Unsurprisingly, the largest variations between the profiles for this component occur within the projected confines of the tip path plane, as shown by the black dotted lines. The profiles created using bins 4 and 5 are difficult to distinguish, indicating that very little is changing between the profiles with this amount of data. The shear component $\overline{u'v'}$, shown in Fig. 39b, shows similar amounts of variation

between the profiles as the normal component. The variations also extend outside of the projected confines of the tip path plane. Overall, general trends within the data can be seen and are mostly consistent.

Contours of the Reynolds stresses $\overline{u'u'}$, $\overline{v'v'}$, and $\overline{w'w'}$ at the $x = D_{hub}$ are shown in Figs. 40-42, and are normalized with respect to the free-stream velocity. Vertical profiles at several y/D_{hub} values situated behind the advancing side are also included for comparison. The $\overline{u'u'}$ component of the Reynolds stress tensor, shown in Fig. 40, shows the production of TKE due to the gradient of the mean velocity $\overline{u}$ in the stream-wise direction. For the Baseline and Phase III hubs, there is a strong resemblance between the TKE production contours and the mean stream-wise velocity contours shown in Fig. 31b. This resemblance is logical because the gradient of the mean velocity, and in this case the momentum deficit, is the driving force of this component of the tensor. Thus, there are high concentrations near the scissor arms and swashplate, as well as the top spider. There is a noticeable bias in this data as well towards the advancing side, directly matching with the mean stream-wise velocity contours. A vertical profile of the magnitude of the Reynolds stress directly behind the advancing blade stub may be compared with similar profiles of Reynolds stresses in the wakes of bluff bodies such as circular or square cylinders. Khalighi et al. [95] and Narasimhamurthy and Andersson [96] performed experimental and numerical analyses of the wakes of simple bluff bodies, and local maxima were found at the extremities of the bluff bodies' geometries corresponding to the shear layers found at those locations, with a local minimum in between which creates two peaks. A similar pattern can be seen in the vertical profiles at $y/D_{hub} = 0.125$ and $y/D_{hub} = 0.25$ for the Baseline and Phase III hubs. As the y/D_{hub} coordinate is moved outward, the profiles only have a single peak value, with the outermost profile being significantly diminished. The Defeatured and Low Drag hubs have comparatively smaller profiles in this case, which is an indication of the effect the scissor arms and swashplate have on turbulent flow in the wake. For the Defeatured hub, the greatest concentration of $\overline{u'u'}$ is positioned just below the bottom spider on the retreating side, and a bias towards the advancing side is still visible. In the Low Drag hub results, lower concentrations are shown scattered throughout, being positioned mostly within the vicinity of the lower spider. Notably, the advancing-side bias is not obvious in the Low Drag

hub's results. The vertical profiles of the Defeatured and Low Drag hubs have maximum values notably shifted above or below the center of the tip path plane and the Low Drag hub profiles are smaller than those of the Baseline and Defeatured hubs.

The $\overline{v'v'}$ component of the Reynolds stresses is shown in Fig. 41. These results take on a similar form to that of the $\overline{u'u'}$ results, but are noticeably weaker in intensity. This is likely due to the expected smaller gradients in the mean span-wise velocity. The Baseline and Phase III hubs again have the largest profiles in the wake, but the fluctuations are more evenly distributed around the approximate center of the hubs. Large concentrations near the scissor arms and swashplate are much less apparent than in the $\overline{u'u'}$ results. However, the distinct difference between the Baseline / Phase III hub cases and the Defeatured hub case seems to be an indication that the scissor arms and swashplate still significantly contribute to this portion of the Reynolds stress tensor. The Low Drag hub case shows very low levels of $\overline{v'v'}$, with small concentrations nears the lower spider on the advancing side and near the blade root on the retreating side. Unlike the vertical profiles of the stream-wise component, the profiles of this component are more clearly centered on the tip path plane. The Baseline and Phase III hub profiles have a greater vertical span than those of the Defeatured and Low Drag hubs, due to the increased projected frontal area.

The $\overline{w'w'}$ component of the Reynolds stresses is shown in Fig. 42, and the concentrations also take comparable forms to that of the $\overline{u'u'}$ Reynolds stresses. The contours of the Baseline and Phase III hubs are similar to the mean stream-wise velocity contours for the corresponding hubs in Fig. 31b. This is most likely due to the dominant nature of the stream-wise component of the mean velocity in these cases. The Low Drag hub again has the lowest levels, with a small concentration positioned just above the center of the rotor hub. The vertical profiles for this Reynolds stress component are again mostly centered on the tip path plane, however the vertical locations of the maximums for the Low Drag hub's profiles tend to vary significantly.

The $\overline{u'v'}$ shear Reynolds stress term reflects the turbulent shear along a plane in constant z, and is associated with the TKE production in the wake due to the stream-wise velocity gradient in the span-wise direction. Physically, this shear term is important due to the span-wise velocity induced by the spinning rotor hub and the natural coupling from the

stream-wise velocity. The contours of this stress terms are shown in Fig. 43, and in this data there is a skew symmetry seen in every hub case. With the Baseline and Phase III hubs, the stresses alternate several times across the span; this is also seen to a lesser extent with the Defeatured and Low Drag hubs. There is a general tendency of the stresses to be negative on the advancing side and positive on the retreating side, and this is driven by the geometry and coordinate system of the data. The Baseline and Phase III hubs also have an additional skew symmetry near the scissor arms and swashplate, which is resultant from the mean u-velocity contours found in Fig. 31b. A very similar skew symmetry has been found in past work studying the wakes behind various bluff bodies such as in Wang and Tan [97], Singha and Balachandar [98], and Rinoshika and Omori [99]. The pattern in this component of the Reynolds stresses, particularly seen in the Baseline and Phase III hub results, is associated with vortex shedding off of a circular cylinder. As the pattern is roughly centered on the rotor hubs, this is most likely due to the presence of the drive shaft and the swashplate. Interestingly, this Reynolds stress component does not seem to be strongly affected by the rotation of the hub and the Magnus effect. The Defeatured and Low Drag hub contours less-distinct patterns but are still roughly centered on the hubs. The vertical profiles reflect the skew symmetry by changing between positive and negative profiles as the coordinate is moved across the advancing side.

The $\overline{u'w'}$ component of the Reynolds stress tensor, which is associated with the TKE production in the wake due to the stream-wise velocity gradient in the vertical direction, is shown in Fig. 44. This shear term is of interest due to the effect the rotor hubs have on the vertical velocity. This is particularly true for the Low Drag Hub, which produced the greatest average vertical force (Table 2). In every case, a horizontal symmetry can be seen spanning the rotor hubs. This line of symmetry is closely aligned with the rotor plane of the hubs, with predominantly negative values in the upper half of the space and positive values in the bottom half. These values seem to be in opposition to the general trend of the vertical gradient of the stream-wise velocity, which have positive values in the upper half of the plane and negative values in the lower half, due to the momentum deficit of the hubs. Strong positive concentrations can still be seen in the Baseline and Phase III hub cases near the scissor arms. The vertical profiles for the Baseline, Defeatured, and Phase IIII hubs

show the expected skew symmetry (cf. Narasimhamurthy and Andersson [96]). The vertical profiles of the Low Drag hub do exhibit this skew symmetry but to a lesser degree, with greater concentrations positioned towards the lower side of the hub. The $y/D_{hub} = 0.25$ profile shows this most clearly, with maximum being approximately twice in magnitude as the minimum. Similar features were found in Reynolds shear stress component profiles shown in Tulapurkara et al. [100], where this shift was found to be due to a combination of effects from the stream-wise pressure gradient and streamline curvature. For the Low Drag hub, evidence of these effects can be seen in its increased lift shown in Table 2.

4.4.2 Third-Order Moments

Third-order moments of velocity fluctuations in the wake, associated with the transport of TKE through turbulent fluctuations, were computed using 5 rotor revolutions of data and are shown in Figs. 45-50. These values were normalized with respect to the free-stream Mach number as well. In the wake of the rotor hubs, the components of transport of TKE due to pressure-velocity fluctuations and molecular viscosity are expected to be negligible, leaving the transport due to turbulent fluctuations to be the primary component of the total TKE transport. The third-order moment of the stream-wise velocity fluctuations both at $x = D_{hub}$ and the full wake profile spanning $x = D_{hub}$ to $x = 3.5D_{hub}$ is shown in Figs. 45-46. For the Baseline and Phase III hubs' results (Figs. 45a & 45d), large negative portions of the wake cross-section at $x = D_{hub}$ are concentrated around the swashplate, scissor arms, and above the main body of the hubs. Positive values show a bias towards the advancing side, similar to what was seen in the Reynolds stresses shown in Figs. 40-42. The Defeatured and Low Drag hubs show predominantly negative values throughout the wake cross-section.

Transport of TKE due to these velocity fluctuations is better understood by observing how these values change through the wake through stream-wise gradients, as these are what govern the transport of TKE according to the TKE budget in Eq. 3.23. A negative stream-wise gradient in the stream-wise third-order moment terms indicates transport of TKE downstream. This is illustrated in Fig. 46. Throughout the wake in each case, a general trend towards an equilibrium can be seen as the wake convects downstream. For large concentrations of negative values, such as the areas circled in red, positive gradients

in the stream-wise direction are clear from one coordinate to the next. In the cases of the Baseline hub and by extension the Phase III hub, negative gradients can be seen such as in the areas circled in green. Similar gradients can be seen in the Defeatured and Low Drag hub cases, however the gradients are predominantly positive. Likewise, comparable positive and negative gradient trends are seen in the contours of $\overline{u'v'v'}$, shown in Figs. 47-48, with smaller magnitudes, similar to what is seen in the $\overline{v'v'}$ results in Fig. 41. The third-order moment $\overline{u'w'w'}$ is shown in Figs. 49-50, and a horizontal symmetry can be seen resembling that of the $\overline{u'w'}$ component of the Reynolds stress tensor shown in Fig. 44. Positive and negative gradients can be seen in every rotor hub case, and in every case the negative gradients are concentrated near the rotor plane and are biased towards the advancing side. Also of note is the negatively-valued concentration near the swashplate on the retreating side in the Baseline Phase III hub case, as well as below the bottom spider in the Defeatured hub case. This feature of the wake is not as prominent in the Low Drag hub case, and a positive gradient is seen in this area.

4.4.3 Turbulent Kinetic Energy Fluxes

The mean convective flux of the TKE through the wake was also calculated by integrating $\overline{u}k$ over the off-body grid slices, and these values for each hub case are shown in Fig. 51. As expected, a negative slope in the flux is shown as the coordinate in the wake increases. The Baseline Phase III hubs show the highest levels of TKE convective flux. This result is logical with the overall increased Reynolds stress content in these hubs as compared with the Defeatured and Low Drag hubs. The percent difference between the Baseline / Phase III hubs and the Defeatured hub TKE fluxes, which varies from approximately 27% at $x = D_{hub}$ to 37% at $x = 3.5D_{hub}$, is a strong indication that the scissor arms are one of the largest single sources of TKE in the rotor hubs' wakes. There appears to be a relation between rotor hub geometry and TKE, indicating that rotor hubs designed to reduce drag correlate with lower overall TKE. As the Low Drag hub has the lowest drag force recorded in Table 2, it subsequently has the lowest levels of TKE. The overall nearly-identical behavior of the TKE flux levels is also an indication that geometry does not have a strong effect on TKE behavior in the wake, and just affects the magnitude.

Integrating $\overline{u'u'u'}$ over each slice, shown in Fig. 52, shows a trend towards zero, similar to the trend seen in Fig. 51. This shows a positive gradient in the stream-wise direction, indicating that TKE is being transported downstream at progressively lower rates as energy is dissipated. The differences in magnitudes between the Baseline / Phase III hubs and the Defeatured hub, which vary from approximately 18.7% at $x = D_{hub}$ to 46.3% at $X = 3.5D_{hub}$, again show the discrepancy between rotor hubs with the scissor arms and swashplate and those without.

4.4.4 Modal Decomposition of Reynolds Stresses

Proper orthogonal decomposition (POD) was used as a tool to understand the study the evolution of a dominant Reynolds stress component through the wake, and specifically to discover spatial coherence between solution snapshots. POD was performed on the instantaneous Reynolds stress $u'u'$ data for five revolutions of rotor hub rotation, which consisted of 7200 time-steps and thus 7200 modes, for each rotor hub. The first 20 modal energies are plotted in Fig. 53. The first mode for each case has a much higher energy than the subsequent modes, indicating that a large portion of the information within the dataset is captured in the first mode. Differences between the Baseline, the Phase III, and the Defeatured hub geometries' modal energy profiles are minor, with the largest difference between the cases appearing with the first mode. The Low Drag hub geometry's energy profile is different from the other three, but maintains the same trend and becomes indistinguishable from the rest by the seventh mode. The first mode of this hub has a significantly lower energy than the other hubs, and the Low Drag hub has more energy distributed throughout the higher-ranked modes than the other hubs. This is an indication that the modes associated with blade arm passage are much more dominant for the Baseline, the Defeatured, and the Phase III hubs. The percentage of modal energy captures within the first 12 modes is shown in Fig. 54 for $x = D_{hub}$ up to $x = 3.5D_{hub}$. For every case, at least 12 modes were needed to capture approximately 50% of the total modal energy. The remaining 50% of the modal energy is contained within the subsequent 7188 modes. This shows that recovery is relatively slow, suggesting a strong influence by seemingly random fluctuations. The energy captured in the lower modes is then effectively broadband noise. The Baseline,

Defeatured, and Phase III hubs' energies seem to plateau quickly, having less than a 1% variation between coordinates within $1.5D_{hub}$ or $2D_{hub}$. The Low Drag hub case does not reach the same level of consistency between the coordinates until the last coordinate, again indicating a more distributed energy profile in the wake.

Contours of the first POD mode of $u'u'$ are shown in Figs. 55-56. Patches of high intensity can be seen scattered throughout the plane at $x = D_{hub}$, shown in Fig. 55. The contours follow the same trends have similar shapes as seen in the Reynolds stress results seen previously shown in Fig. 40, although the relative apparent magnitudes of the concentrations in each geometries' results have changed; for example, the concentration near the retreating side blade arm in the Low Drag hub results appears to be greater than the concentration near the scissor arms and swash plate on the retreating side in the Baseline hub results. The advancing side of the Baseline and Phase III hubs near the blade arms is noticeably different in the first mode contours, with values approaching zero. This highlights again the retreating side bias seen in the velocity frequency analysis in Figs. 36-37. This is also visible to a lesser extent in the Defeatured and Low Drag hub results. This highlights the fact that the Reynolds stresses captured in this mode, which are the most energetic, are biased towards the retreating side, similar to what was seen in the velocity frequency analysis in Figs. 36-37. The Reynolds stresses on the advancing side, which are concentrated in the mean data and plotted in Fig. 40a, have noticeably low energy in the first POD mode. This indicates that the Reynolds stress data on the advancing side has been captured in a set of lower modes; due to the rapidity with which the modal energy levels approach very small percentages, this set of lower modes is most likely very large. The relatively high energy level of the first mode illustrated in Fig. 53 shows that a large portion of the Reynolds stresses, which is mostly concentrated on the retreating side of the hub, evolves with a single characteristic mode. This suggests that the Reynolds stress average acts as a good metric for quantifying turbulent behavior in rotor hub wakes.

The behavior of the first mode throughout the wake is plotted in Fig. 56), and the POD energy diffuses and spreads, behaving similarly to the Reynolds stress data as was inferred in the plots shown in Figs. 51 and 52. Despite the differences between the first POD mode and averaged Reynolds stress contours in terms of relative magnitude, the overall behavior

within both sets of results is very similar. This suggests that the Reynolds stress average offers a fair approximation of the behavior of the rotor hub wakes. Qualitatively, the level of coherence and detail seen in these POD results is higher than the contours of the POD modes of the stream-wise momentum in Wall and Coder [67]. This seems to further strengthen the Reynolds stress's position as a metric of turbulent wake behavior in the case of these rotor hubs over other variables such as the stream-wise momentum.

Chapter 5: Conclusions

Four rotor hub geometries were simulated in identical flow conditions to study Reynolds stresses and the evolution of turbulent kinetic energy in the wakes. Surface forces exhibited expected behaviors, such as the dominant 4/rev frequency present in the phase-averaged effective flat plate areas, and the spectral content of the same. A significant difference in the 2/rev content of the nearly-identical Baseline and Phase III rotor hubs was an indication that more data was needed to obtain converged spectral content. Time-averaged stream-wise and vertical velocity contours were compared to current and past experimental data and showed good agreement in magnitude and behavior. A bias in the stream-wise velocity towards the advancing side, seen in experimental data and due to the Magnus effect, was also seen in the time-averaged velocity contours. Velocity profiles at several x-coordinates in the wake showed discrepancies compared with experimental results due to the lack of the mounting pylon.

A frequency analysis of stream-wise and vertical velocity profiles was applied to the rotor hubs using the fast Fourier transform. For the stream-wise velocity component, the Baseline and Phase III hubs showed significantly higher 2/rev content than the Defeatured and Low Drag hubs due to the presence of the scissor arms, which matches well with results seen in previous studies. Every hub displayed significant 4/rev content, both in the stream-wise and vertical velocity profiles, which was expected due to the dominant 4/rev symmetry of each geometry. Significantly, higher frequency content was seemingly under-predicted for the rotor hubs, with exception to the Low Drag hub. The increased level of higher frequency content for the Low Drag hub was also seen in the results in Wall and Coder [67], and seems to be related to the produced lift behavior from the geometry of the blade arms. The Baseline and Phase III hubs showed increased levels of 6/rev content, albeit still noticeably lower than that of experimental results, than the other hubs. This suggested that the 6/rev content in the wake, which has been seen in previous work such as Reich et al. [61], could be attributed to a non-linear interaction between 2/rev and 4/rev frequency content produced by the scissor arms and blade stubs, respectively. A general spatial bias towards the retreating side in the

frequency data was also seen. This bias has been seen in experimental work [61], and is likely due to the same reason for the physical bias in the time-averaged stream-wise velocity. Although frequency content in the far wake was not shown or discussed in this work, the spatial placement of the frequency content in the wake is not likely to change much in the far wake if disregarding the effects of interactional aerodynamics from the helicopter fuselage or the helicopter rotor. As the sources of substantial frequency content in the wake as well as the spatial placement of this content in the wake have been identified, future rotorcraft vehicles in development which incorporate similar rotor hub designs could be expected to experience similar behaviors in the wake and likely vibrational loads on the empennage and tail rotor.

Reynolds stresses were also computed and compared between the rotor hubs, with an emphasis on their relation to turbulent kinetic energy production using 5 revolutions of data. It was found through a study of the convergence of these time-averaged terms that general trends within the data seemed to be consistent, and convergence seemed to be achieved by 5 revolutions of hub rotation. The Baseline and Phase III hubs showed the highest levels of perturbations in the normal components of the Reynolds stress tensor and the largest profiles in the wake, with concentrations notably positioned near the scissor arms as well as the blade arms and top spider in the $\overline{u'u'}$ and $\overline{w'w'}$ results. Perturbations behaved similarly between the rotor hubs in the shear components $\overline{u'v'}$ and $\overline{u'w'}$, with smaller magnitudes overall. The $\overline{u'v'}$ results displayed a skew symmetry in the sign of the values, which was from the geometry and coordinate system used in the simulations. The Baseline and Phase III hubs displayed additional alternating values in the vicinity of the scissor arms which correlated to the mean stream-wise velocity span-wise gradients. Vertical profiles of the Reynolds stresses at several y/D_{hub} coordinates on the advancing side showed similar behaviors as what has been seen in the wakes of simple bluff bodies such as a circular cylinder. The Baseline and Phase III hubs' profiles were similar to those of a circular cylinder, particularly for the y/D_{hub} coordinates closest to the center of the rotor hub. The $\overline{u'w'}$ vertical profiles of the Low Drag hub showed signs of effects from the streamline curvature and stream-wise pressure gradient.

Third-order moments of velocity perturbations were also computed to study TKE transport in the rotor hub wakes. Both positive and negative gradients were found in the

stream-wise direction for every rotor hub. As positive gradients are an indication of TKE transport downstream, the presence of negative gradients was surprising. In every third-order moment result, the negative gradients were shaped similarly to the time-averaged stream-wise velocity contours, including a bias towards the advancing side. Because of the consistency of this bias in the results, it is most likely caused by the increased shear caused by the increased relative velocity on the advancing side. This leads to and subsequent increased mixing in the wake on the advancing side which more quickly diffuses the perturbations in this area of the wake. As previously mentioned, this is also the likely cause for the retreating-side bias found in the frequency content analysis and POD of the instantaneous Reynolds stresses. As the perturbations in the wake are diffused more quickly on the advancing side, the perturbations on the retreating side are relatively stronger and more energetic.

Additionally, the TKE flux was computed and its trend through the wake showed higher magnitudes of TKE flux in the wake for the Baseline and Phase III hubs compared to that of the Defeatured and Low Drag hubs, and a relation between drag-reducing geometry and TKE flux seemed to be present. These results again indicated the significant effect the scissor arms had on the wake behavior and structures found therein. Integrating $\overline{u'u'u'}$ over each plane exported was also computed and displayed a similar trend to that found in the TKE flux through the wake. This further indicates a relation between rotor hub geometry intended to reduce drag and the TKE magnitude in the wake. Values of the integrated TKE flux and $\overline{u'u'u'}$ in the wake for the Baseline and Phase III hubs were also nearly identical, showing that these quantities exhibit less sensitivity and could therefore be beneficial for similar comparison studies than the quantities such as the magnitudes of the Fourier-transformed surface forces.

Lastly, proper orthogonal decomposition was performed on the instantaneous Reynolds stress component $u'u'$. In every rotor hub case, the first POD mode had significantly higher modal energy than subsequent modes, attaining 25%-33% of the total modal energy depending on the rotor hub. The first 12 (of 7200) POD modes encompassed approximately 50% of the total modal energy at each coordinate within the wake. The first POD mode contours also showed much of the same behavior captured in the averaged Reynolds stress contours, indicating that the averaged values produce a fair approximation of the data. The

qualitative coherence shown by the POD results also strengthens the Reynolds stress average as a metric of turbulent wake behavior for rotor hubs. The first POD mode contours showed that much of the highest-energy Reynolds stresses were concentrated on the retreating side of the rotor hub. This indicated that the Reynolds stress data on the advancing side was captured in a large set of lower POD modes, meaning that these perturbations occurred more frequently but were weaker than those on the retreating side. This corresponds with the frequency content results, and physically this indicates that any loads felt by the empennage and tail rotor of a given helicopter will most likely have a harmonic behavior on the retreating side and a more turbulent behavior on the advancing side. Qualitatively, coherence in the first POD mode appeared higher than that of POD modes of stream-wise momentum computed in past work.

Continued work on this subject has included a similar study of a coaxial rotor hub, which corresponded to experimental work recorded in Tierney et al. [101], and is published in Mobley and Coder [102]. Due to differences in the free stream Reynolds number and hub advance ratio used, it was not included in this document. Future analyses of rotor hubs should include a more-thorough analysis of the frequency content and Reynolds stresses in the far wake, where the wake may interact with the empennage and/or the tail rotor. As these hubs were completely isolated, the effects of interactional aerodynamics were also not present in this work. Therefore, how the spectral content and the velocity perturbations behave when the helicopter fuselage is present, and how this affects the possible interactions with the empennage, is also a future topic of study. With regards to the turbulence analysis, quantification of the unresolved scales is another topic which would be beneficial.

References

[1] Stepniewski, W., and Keys, C., Rotary-Wing Aerodynamics, Dover Books on Aeronautical Engineering, Dover Publications, 2013.

[2] Leishman, J. G., Principles of Helicopter Aerodynamics, 2nd ed., Cambridge University Press, Cambridge, 2006.

[3] Gablehouse, C., Helicopters and Autogiros: A History of Rotating-wing and V/STOL Aviation, Lippincott, 1969.

[4] Harris, F. D., Introduction To Autogyros, Helicopters, and Other V/STOL Aircraft, Vol. 2, National Air and Space Association, 2012.

[5] U.S. Department of Transportation, "FAA Helicopter Flying Handbook," Tech. Rep. FAA-H-8083-21B, 2019. URL https://www.faa.gov/.

[6] Churchill, G. B., and Harrington, R. D., "Parasite-Drag Measurements of Five Helicopter Rotor Hubs," NASA Memo 1-31-59L, Feb. 1959.

[7] Keys, C. N., and Wiesner, R., "Guidelines for Reducing Helicopter Parasite Drag," Journal of the American Helicopter Society, Vol. 20, No. 1, 1975.

[8] Sheehy, T. W., "A General Review of Helicopter Rotor Hub Drag Data," Journal of the American Helicopter Society, Vol. 22, No. 2, 1977.

[9] Reich, D., Shenoy, R., Smith, M., and Schmitz, S., "A Review of 60 Years of Rotor Hub Drag and Wake Physics: 1954–2014," Journal of the American Helicopter Society, Vol. 61, No. 2, 2016, pp. 1–17. https://doi.org/10.4050/JAHS.61.022007.

[10] Sheridan, P. F., and Smith, R. P., "Interactional Aerodynamics - A New Challenge to Helicopter Technology," Journal of the American Helicopter Society, Vol. 25, No. 1, 1980, pp. 3–21. https://doi.org/doi:10.4050/JAHS.25.1.3.

[11] Wall, T. D., "Investigation of Predicted Helicopter Rotor Hub Drag and Wake Flow With Reduced Order Modeling," Master's of Science, The University of Tennessee, Knoxville, TN, 2020.

[12] Prouty, R. W., and Jr., H. C. C., "Helicopter Control Systems: A History," Journal of Guidance, Control, and Dynamics, Vol. 26, No. 1, 2003. https://doi.org/10.2514/25039.

[13] Seddon, J. M., and Newman, S., "[4.3] Rotor Control," Basic Helicopter Aerodynamics, Blackwell Science, 2002, 2nd ed.

[14] Roesch, P., "Aerodynamic Design of the Aerospatiale SA 365N Dauphin 2 Helicopter," Journal of the American Helicopter Society, Vol. 27, No. 2, 1982.

[15] Coleman, R. P., and Feingold, A. M., "Theory of Self-Excited Mechanical Oscillations of Heliocpter Rotors With Hinged Blades," NACA Report 1351, National Advisory Committee for Aeronautics, 1958.

[16] Reddick, H. K., Jr., "Army Helicopter Cost Drivers," Technical Memorandum USAAMRDL-TM-7, United States Army Air Mobility Research and Development Laboratory, Fort Eustis, Virginia, Aug. 1975.

[17] Levenetz, B., "Composite-Material Helicopter Rotor Hubs," Technical Report USAAMRDL-TR-73-14, United States Army Air Mobility Research and Development Laboratory, Fort Eustis, Virginia, Jul. 1973.

[18] Weiland, E. F., "Development and Test of the BO 105 Rigid Rotor Helicopter," 24th Annual National Forum of the American Helicopter Society, American Helicopter Society, Washinton, D.C., 1968.

[19] Cardinale, S. V., "Soft In-Plane Matched-Stiffness/Flexure-Root-Blade Rotor System Summary Report," Technical Report USAAVLABS-TR-68-72, United States Army Aviation Material Laboratories, Fort Eustis, Virginia, Aug. 1969.

[20] Dixon, P. G. C., "Design, Development, and Flight Demonstration of the Loads and Stability Characteristics of a Bearingless Main Rotor," Technical Report USAAVRADCOM-TR-80-D-3, United States Army Research and Technology Laboratories, Philidelphia, PA, Jun. 1980.

[21] Bousman, W. G., Ormiston, R. A., and Mirick, P. H., "Design Considerations for Bearingless Rotor Hubs," 39th Annual Forum, American Helicopter Society, St. Louis, MO, 1983.

[22] Harrington, R. D., "Reduction of Helicopter Parasite Drag," Technical Note NACA TN 3234, National Advisory Committee for Aeronautics, Langley Field, VA., Aug. 1954.

[23] Sweet, G. E., and Jenkins, J. L., Jr., "Wind-Tunnel Investigation of the Drag and Static Stability Characteristics of Four Helicopter Fuselage Models," Technical Note NASA TN D-1363, National Air and Space Association, Langley Station, Hampton, VA., Jul. 1962.

[24] Linville, J. C., "An Experimental Investigation of High-Speed Rotorcraft Drag," Technical Report USAAMRDL-TR-71-46, United States Army Air Mobility Research and Development Laboratory, Fort Eustis, Virginia, Feb. 1972.

[25] Sheehy, T. M., and Clark, D. R., "A Method for Predicting Helicopter Hub Drag," Technical Report USAAMRDL-TR-75-48, United States Army Air Mobility Research and Development Laboratory, Fort Eustis, Virginia, Jan. 1976.

[26] Logan, A. H., Prouty, R. W., and Clark, D. R., "Wind Tunnel Tests of Large- and Small-Scale Rotor Hubs and Pylons," Technical Report USAAVRADCOM-TR-80-D-21, United States Army Research and Technology Laboratories, Fort Eustis, Virginia, Apr. 1981.

[27] Felker, F. F., "An Experimental Investigation of Hub Drag on the XH-59A," Proceedings of the 3rd AIAA Applied Aerodynamics Conference, AIAA, Colorado Springs, CO, 1985.

[28] Young, L. A., Graham, D. R., and Stroub, R. H., "Experimental Investigation of Rotorcraft Hub and Shaft Fairing Drag Reduction," AIAA Journal of Aircraft, Vol. 24, No. 12, 1987.

[29] Stroub, R. H., Young, L. A., Graham, D. R., and Louie, A. W., "Investigation of Generic Hub Fairing and Pylon Shapes to Reduce Hub Drag," Technical Memorandum NASA TM-10008, Sep. 1987.

[30] Graham, D. R., Sung, D. Y., Young, L. A., Louie, A. W., and Stroub, R. H., "Helicopter Hub Fairing and Pylon Interference Drag," Technical Memorandum NASA-TM-101052, NASA Ames Research Center, Moffett Field, CA, Jan. 1989.

[31] Sung, D. Y., Lance, M. B., Young, L. A., and Stroub, R. H., "An Experimental Investigation of Helicopter Rotor Hub Fairing Characteristics," Technical Memorandum NASA-TM-102182, NASA Ames Research Center, Moffett Field, CA, Sep. 1989.

[32] Martin, D. M., Mort, R. W., Young, L. A., and Squires, P. K., "Experimental Investigation of Advanced Hub and Pylon Fairing Configurations to Reduce Helicopter Drag," Technical Memorandum NASA-TM-4540, NASA Ames Research Center, Moffett Field, CA, Sep. 1993.

[33] Potsdam, M., and le Pape, A. L., "CFD Investigations on a NACA0036 Airfoil with Active Flow Control," AIAA 4th Flow Control Conference, AIAA, Seattle, WA, 2008.

[34] Renaud, T., O'Brien, D., Smith, M., and Potsdam, M., "Evaluation of Isolated Fuselage and Rotor–Fuselage Interaction Using Computational Fluid Dynamics," Journal of the American Helicopter Society, Vol. 53, No. 1, 2008.

[35] Smith, M. J., Shenoy, R., Kenyon, A. R., and Brown, R. E., "Vorticity-Transport and Unstructured RANS Investigation of Rotor-Fuselage Interactions," 35th European Rotorcraft Forum, Hamburg, Germany, 2009.

[36] Fletcher, T. M., and Brown, R. E., "Main Rotor-Tail Rotor Wake Interaction and Its Implications for Helicopter Directional Control," Journal of the American Helicopter Society, Vol. 53, No. 2, 2008, pp. 125–138. https://doi.org/10.4050/JAHS.53.125.

[37] Kenyon, A. R., and Brown, R. E., "Wake Dynamics and Rotor-Fuselage Aerodynamic Interactions," Journal of the American Helicopter Society, Vol. 54, No. 1, 2009. https://doi.org/10.4050/JAHS.54.012003.

[38] Antoniadis, A. F., Drikakis, D., Zhong, B., Barakos, G., Steijl, R., Biava, M., Vigevano, L., Brocklehurst, A., Boelens, O., Dietz, M., Embacher, M., and Khier, W., "Assessment of CFD Methods Against Experimental Flow Measurements for Helicopter Flows," Aerospace Science and Technology, Vol. 19, No. 1, 2012, pp. 86–100.

[39] Shenoy, R., Holmes, M., Smith, M. J., and Komerath, N., "Computational Investigation of Hub Drag Deconstruction from Model to Full Scale," 37th European Rotorcraft Forum, Vergiate and Gallarate, Italy, 2011.

[40] Shenoy, R., Holmes, M., Smith, M. J., and Komerath, N., "Scaling Evaluations on the Drag of a Hub System," Journal of the American Helicopter Society, Vol. 58, No. 1, 2013.

[41] Shenoy, R., and Smith, M. J., "Deconstructing Hub Drag Part II: Computational Development and Analysis," Final Technical Report to the Office of Naval Research N0001409-1-1019, Georgia Institute of Technology, Atlanta, GA, Sep. 2013.

[42] Shenoy, R., Smith, M. J., and Park, M. A., "Unstructured Overset Mesh Adaptation with Turbulence Modeling for Unsteady Aerodynamic Interactions," Journal of Aircraft, Vol. 51, No. 1, 2014.

[43] Forbes, A., Raghav, V., Mayo, M., and Komerath, N., "Rotation Effects on Hub Drag," IMECE2013, San Diego, CA, 2013.

[44] Khier, W., "Computational Investigation of Advanced Hub Fairing Configurations to Reduce Helicopter Drag," 40th European Rotorcraft Forum, Southampton, UK, 2014.

[45] Sheridan, P., "Interactional Aerodynamics of the Single Rotor Helicopter Configuration," USARTL Technical Report 78-23, United States Army Research and Technology Laboratories, Fort Eustis, Virginia, Sep. 1978.

[46] Blake, B., and Alansky, I., "Stability and Control of the YUH-61A," Journal of the American Helicopter Society, Vol. 22, 1977, pp. 2–10. https://doi.org/10.4050/JAHS.22.1.2.

[47] Roesch, P., and Dequin, A., "Experimental Research on Helicopter Fuselage and Rotor Hub Wake Turbulence," Journal of the American Helicopter Society, Vol. 30, No. 1, 1985, pp. 43–51. https://doi.org/10.4050/JAHS.30.1.43.

[48] Gorton, S. A., Meyers, J. F., and Berry, J. B., "Velocity Measurements Near the Empennage of a Small-Scale Helicopter," American Helicopter Society 52nd Annual Forum, Washinton, D.C., 1996.

[49] Gorton, S. A., Berry, J. D., Hodges, W. T., and Reis, D. G., "Flow Environment Study Near the Empennage of a 15-Percent Scale Helicopter Model," Technical Paper TP-2000-210085, NASA Langley Research Center, Hampton, Virginia, Mar. 2000.

[50] Gorton, S. A., Berry, J. D., Hodges, W. T., and Reis, D. G., "Rotor Wake Study Near the Horizontal Tail of a T-Tail Configuration," Journal of Aircraft, Vol. 39, No. 4, 2002, pp. 645–653.

[51] Mason, P. H., "Identification of Random Loads Impinging on the RAH-66 Comanche Helicopter Empennage Using Spectral Analysis," Master's thesis, U.S. Navy Naval Postgraduate School, Monterey, California, 1998.

[52] Berry, J. D., "Unsteady Velocity Measurements Taken Behind a Model Helicopter Rotor Hub in Forward Flight," Technical Memorandum NASA-TM-4738, NASA, Langley Research Center, Mar. 1997.

[53] Yin, J. P., and Ahmed, S. R., "Helicopter Main-Rotor/Tail-Rotor Interaction," Journal of the American Helicopter Society, Vol. 45, No. 4, 2000, pp. 293–302.

[54] Ruffin, S. M., O'Brien, D., Smith, M. J., Hariharan, N., Lee, J.-D., and Sankar, L., "Comparison of Rotor-Airframe Interaction Utilizing Overset and Unstructured Grid Techniques," AIAA 42nd Aerospace Sciences Meeting, Reno, NV, 2004.

[55] Chen, H.-n., Brentner, K. S., Ananthan, S., and Leishman, J. G., "A Computational Study of Helicopter Rotor Wakes and Noise Generated During Transient Maneuvers," Journal of the American Helicopter Society, Vol. 53, No. 1, 2008, pp. 37–55.

[56] Yang, C., Aoyama, T., Kondo, N., and Saito, S., "Numerical Analysis for Main-Rotor/Tail-Rotor Interaction of Helicopter," JAXA Research and Development Report JAXA-RR-08-006E, Japan Aerospace Exploration Agency, Mar. 2009.

[57] Jain, R. K., and Potsdam, M. A., "Hover Predictions on the Sikorsky S-76 Rotor Using Helios," 52nd Annual Science and Technology Forum and Exhibition, AIAA, National Harbor, Maryland, 2014.

[58] Hariharan, N., Egolf, A., and Sankar, L., "Simulation of Rotor in Hover: Current State and Challenges," 52nd Annual Science and Technology Forum and Exposition, AIAA, National Harbor, Maryland, 2014.

[59] Raghav, V., Shenoy, R., Smith, M., and Komerath, N., "Investigation of Drag and Wake Turbulence of a Rotor Hub," Aerospace Science and Technology, Vol. 28, No. 1, 2013, pp. 164–175. https://doi.org/10.1016/J.AST.2012.10.012.

[60] Reich, D. B., Elbing, B. R., Berezin, C. R., and Schmitz, S., "Water Tunnel Flow Diagnostics of Wake Structures Downstream of a Model Helicopter Rotor Hub," Journal of the American Helicopter Society, Vol. 59, No. 3, 2014, pp. 1–12. https://doi.org/10.4050/JAHS.59.032001.

[61] Reich, D., Sinding, K., and Schmitz, S., "Visualization of a Helicopter Rotor Hub Wake," Experiments in Fluids, Vol. 59, No. 7, 2018. https://doi.org/10.1007/s00348-018-2571-7.

[62] Potsdam, M., and Cross, P., "Assessment of CREATE-AV Helios for Complex Rotating Hub Wakes," AHS International 73rd Annual Forum & Technology Display, American Helicopter Society, Fort Worth, TX, 2017.

[63] Wissink, A., Sitaraman, J., Jayaraman, B., Roget, B., Lakshminarayan, V., Potsdam, M., Jain, R., Leffel, J., Forsythe, J., and Bauer, A., "Recent Advancements in the Helios Rotorcraft Simulation Code," 54th Annual Science and Technology Forum and Exposition, AIAA, San Diego, CA, 2016.

[64] Potsdam, M., and Sitaraman, J., "Assessment of HPCMP CREATE-AV Helios for Interactional Aerodynamics of Hub Wakes Impinging on a Horizontal Stabilizer," Vertical Flight Society's 75th Annual Forum & Technology Display, Vertical Flight Society, Philidelphia, PA, 2019.

[65] Metkowski, L., Reich, D., Sinding, K., Jaffa, N., and Schmitz, S., "Full-Scale Reynolds Number Experiment on Interactional Aerodynamics Between Two Model Rotor Hubs and Horizontal Stabilizer," 74th Annual Forum of the American Helicopter Society, Phoenix, AZ, 2018.

[66] Coder, J. G., "Effects of Transition Modeling on the Simulation of Helicopter Rotor Hubs," Vertical Flight Society's 75 Annual Forum & Technology Display, Philadelphia, PA, 2019.

[67] Wall, T., and Coder, J. G., "Reduced-Order Modeling and Analysis of Unsteady Rotor Hub Flows," Vertical Flight Society's 76th Annual Forum Proceedings, Virtual, 2020.

[68] Schmitz, S., Reich, D., Smith, M. J., and Centolanza, L. R., "First Rotor Hub Flow Prediction Workshop Experimental Data Campaigns and Computational Analyses," AHS International 73rd Annual Forum Proceedings, Fort Worth, Texas, 2017.

[69] Schmitz, S., Tierney, C., Metkowski, L., Reich, D., Jaffa, N., Centolanza, L. R., and Thomas, M. L., "2nd Rotor Hub Flow Prediction Workshop Experimental Data Campaigns & Computational Analyses," Vertical Flight Society's 75 Annual Forum Proceedings, Philadelphia, PA, 2019.

[70] Schmitz, S., Tierney, C., Reich, D., Jaffa, N., Centolanza, L. R., and Thomas, M. L., "Three Rotor Hub Flow Prediction Workshops (2016-2020) - What Did We Learn & What's Next?" Vertical Flight Society's 77th Annual Forum Proceedings, Virtual, 2021.

[71] Nichols, R. H., and Buning, P. G., "User's Manual for OVERFLOW 2.2," , 2010.

[72] Pulliam, T. H., and Steger, J. L., "Implicit Finite-Difference Simulations of Three-Dimensional Compressible Flow," AIAA Journal, Vol. 18, No. 2, 1980, pp. 159–167. https://doi.org/10.2514/3.50745.

[73] Nichols, R. H., Tramel, R. W., and Buning, P. G., "Evaluation of Two High-Order Weighted Essentailly Nonoscillatory Schemes," AIAA Journal, Vol. 46, No. 12, 2008, pp. 3090–3102. https://doi.org/10.2514/1.36849.

[74] Roe, P. L., "Approximate Riemann Solvers, Parameter, Vectors, and Difference Schemes," Journal of Computational Physics, Vol. 43, No. 2, 1981, pp. 357–372. https://doi.org/10.1.1.457.5978.

[75] Nichols, R., Tramel, R., and Buning, P., "Solver and Turbulence Model Upgrades to OVERFLOW 2 for Unsteady and High-Speed Applications," 24th AIAA Applied Aerodynamics Conference, American Institute of Aeronautics and Astronautics, 2006. https://doi.org/10.2514/6.2006-2824.

[76] Jameson, A., "Time Dependent Calculations Using Multigrid, with Applications to Unsteady Flows Past Airfoils and Wings," 10th Computational Fluid Dynamics Conference, American Institute of Aeronautics and Astronautics, 1991. https://doi.org/10.2514/6.1991-1596.

[77] Klopfer, G. H., Wijngaart, R. F. V. D., Hung, C. M., and Onufer, J. T., "A Diagonalized Diagonal Dominant Alternating Direction Implicit (D3ADI) Scheme and Subiteration Correction," 29th AIAA Fluid Dynamics Conference, Albuquerque, NM, 1998. https://doi.org/10.2514/6.1998-2824.

[78] Pulliam, T., and Chaussee, D., "A Diagonal Form of an Implicit Approximate-Factorization Algorithm," Journal of Computational Physics, Vol. 39, No. 2, 1981, pp. 347–363. https://doi.org/10.1016/0021-9991(81)90156-X.

[79] Spalart, P. R., and Allmaras, S. R., "A One-Equation Turbulence Model for Aerodynamic Flows," 30th AIAA Aerospace Sciences Meeting, Reno, NV, 1992. https://doi.org/10.2514/6.1992-439.

[80] Allmaras, S. R., Johnson, F. T., and Spalart, P. R., "Modifications and Clarifications for the Implementation of the Spalart-Allmaras Turbulence Model," ICCFD7, Big Island, HI, 2012.

[81] Spalart, P. R., Deck, S., Shur, M. L., Squires, K. D., Strelets, M. K., and Travin, A., "A New Version of Detached-eddy Simulation, Resistant to Ambiguous Grid Densities," Theoretical and Computational Fluid Dynamics, Vol. 20, No. 3, 2006, p. 181. https://doi.org/10.1007/s00162-006-0015-0.

[82] Shur, M. L., Strelets, M. K., Travin, A. K., and Spalart, P. R., "Turbulence Modeling in Rotating and Curved Channels: Assessing the Spalart-Shur Correction," AIAA Journal, Vol. 38, No. 5, 2000, pp. 784–792. https://doi.org/10.2514/2.1058.

[83] Chan, W. M., Nash, S. M., Buning, P. G., Meakin, R. L., Boger, D. A., and Pandya, S. A., "Chimera Grid Tools User's Manual, Version 2.0," , 2007.

[84] Meakin, R. L., "Object X-Rays for Cutting Holes in Composite Overset Structured Grids," 15th AIAA Computational Fluid Dynamics Conference, Anaheim, CA, 2001. https://doi.org/6.2001-2537.

[85] Spalart, P. R., and Rumsey, C. L., "Effective Inflow Conditions for Turbulence Models in Aerodynamic Calculations," AIAA Journal, Vol. 45, No. 10, 2007, pp. 2544–2553. https://doi.org/10.2514/1.29373.

[86] Boger, D., and Dreyer, J., "Prediction of Hydrodynamic Forces and Moments for Underwater Vehicles Using Overset Grids," 44th AIAA Aerospace Sciences Meeting and Exhibit, Aerospace Sciences Meetings, American Institute of Aeronautics and Astronautics, 2006. https://doi.org/10.2514/6.2006-1148.

[87] MATLAB, Version 9.9.0 (R2020b), The MathWorks Inc., Natick, Massachusetts, 2020.

[88] Vela Software International, FieldView 21, 2021. URL https://www.fieldviewcfd.com.

[89] Reynolds, O., "IV. On the Dynamical Theory of Incompressible Viscous Fluids and the Determination of the Criterion," Philosophical Transactions of the Royal Society of London. (A.), Vol. 186, 1895, pp. 123–164. https://doi.org/10.1098/rsta.1895.0004.

[90] Pope, S., Turbulent Flows, Cambridge University Press, 2000.

[91] Furbo, E., "Evaluation of RANS Turbulence Models for Flow Problems with Significant Impact of Boundary Layers," Master's thesis, Uppsala University, Uppsala, Sweden, 2010.

[92] Taira, K., Brunton, S. L., Dawson, S. T. M., Rowley, C. W., Colonius, T., McKeon, B. J., Schmidt, O. T., Gordeyev, S., Theofilis, V., and Ukeiley, L. S., "Modal Analysis of Fluid Flows: An Overview," AIAA Journal, Vol. 55, No. 12, 2017, pp. 4013–4041. https://doi.org/10.2514/1.J056060.

[93] Mobley, F. J., Wall, T., and Coder, J. G., "Computational Characterization of Unsteady Rotor Hub Wakes," Vertical Flight Society's 77th Annual Forum Proceedings, Virtual, 2021.

[94] Mobley, F. J., and Coder, J. G., "Computational Characterization of Unsteadiness and Turbulence in Rotor Hub Wakes," Journal of the American Helicopter Society, (accepted for publication).

[95] Khalighi, B., Zhang, S., Koromilas, C., Balkanyi, S. R., Bernal, L. P., Iaccarino, G., and Moin, P., "Experimental and Computational Study of Unsteady Wake Flow Behind a Bluff Body with a Drag Reduction Device," SAE Transactions, Vol. 110, 2001, pp. 1209–1222. URL http://www.jstor.org/stable/44730974.

[96] Narasimhamurthy, V. D., and Andersson, H. I., "Numerical Simulation of the Turbulent Wake behind a Normal Flat Plate," International Journal of Heat and Fluid Flow, Vol. 30, No. 6, 2009, pp. 1037–1043. https://doi.org/10.1016/j.ijheatfluidflow.2009.09.002.

[97] Wang, X., and Tan, S., "Near-Wake Flow Characteristics of a Circular Cylinder Close to a Wall," Journal of Fluids and Structures, Vol. 24, No. 5, 2008, pp. 605–627. https://doi.org/10.1016/j.jfluidstructs.2007.11.001.

[98] Singha, A., and Balachandar, R., "Structure of Wake of a Sharp-Edged Bluff Body in a Shallow Channel Flow," Journal of Fluids and Structures, Vol. 27, No. 2, 2011, pp. 233–249. https://doi.org/10.1016/j.jfluidstructs.2010.11.001.

[99] Rinoshika, A., and Omori, H., "Orthogonal Wavelet Analysis of Turbulent Wakes behind Various Bluff Bodies," Experimental Thermal and Fluid Science, Vol. 35, No. 7, 2011, pp. 1231–1238. https://doi.org/10.1016/j.expthermflusci.2011.04.010.

[100] Tulapurkara, E. G., Ramjee, V., and George, J., "Development of a Bluff Body Wake under the Combined Influence of Curvature and Pressure Gradient," Experiments in Fluids, Vol. 18, No. 5, 1995, pp. 311–318. https://doi.org/10.1007/BF00211386.

[101] Tierney, C., Reich, D., Jaffa, N., and Schmitz, S., "Scaled Model Testing of Coaxial Rotor Hub Flows," Vertical Flight Society's 77th Annual Forum Proceedings, Virtual, 2021.

[102] Mobley, F. J., and Coder, J. G., "Computational Analysis of a Model Coaxial Rotor Hub Wake," 78th Annual Forum and Technology Display, Vertical Flight Society, Fort Worth, TX, 2022.

[103] Brittanica, "Bell Jet Ranger 206-B," , 1998. URL https://www.britannica.com/technology/helicopter/images-videos#/media, retreived January 2022.

[104] Boeing, "SB>1 Defiant," , 2021. URL https://www.boeing.com/defense/future-long-range-assault-aircraft/index.page#/gallery, retrieved April 2022.

[105] Boeing, "Boeing CH-47 Chinook," , 2021. URL https://www.boeing.com/defense/ch-47-chinook/#/gallery, retrieved April 2022.

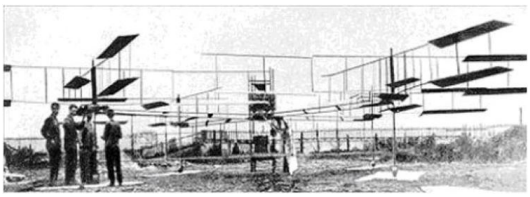
[106] Boeing, "Boeing MH-139A," , 2021. URL https://www.boeing.com/defense/mh-139a/index.page#/gallery, retrieved April 2022.

Appendix

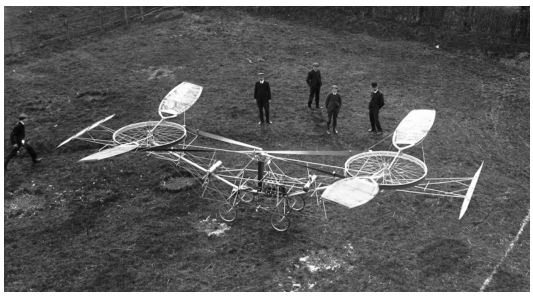
Appendix A: Chapter 1 Figures and Tables



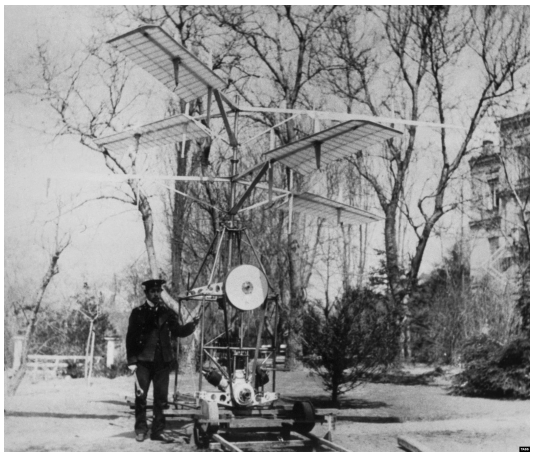
Figure 1: Helicopter with single rotor and tail rotor configuration [103]



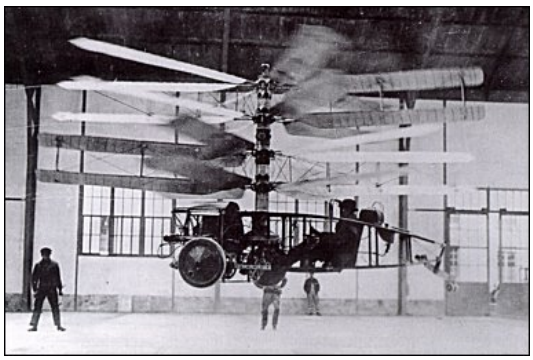
(a) Bréguet-Richet Gyroplane No. 1, Aug. 1907 [3]



(b) Paul Cornu's tandem helicopter, Nov. 1907 [3]



(c) Igor I. Sikorsky's coaxial helicopter, 1910 [3]



(d) Marquis Pescara's coaxial helicopter, 1924 [2]

Figure 2: Early designs of aircraft capable of vertical flight

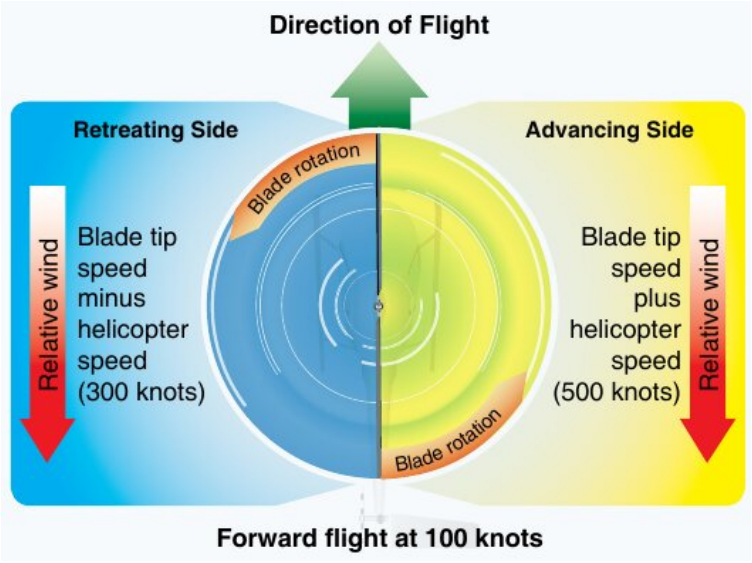


Figure 3: Helicopter lift dissymmetry [5]

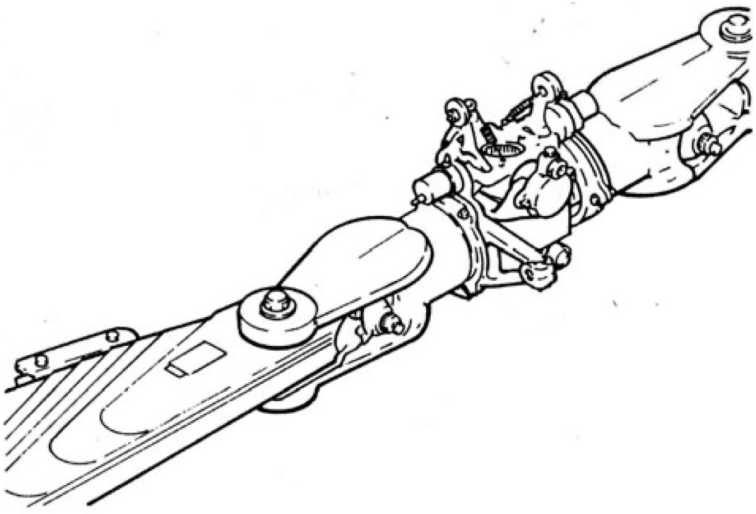


Figure 4: Bell Model 206 teetering rotor hub [4]

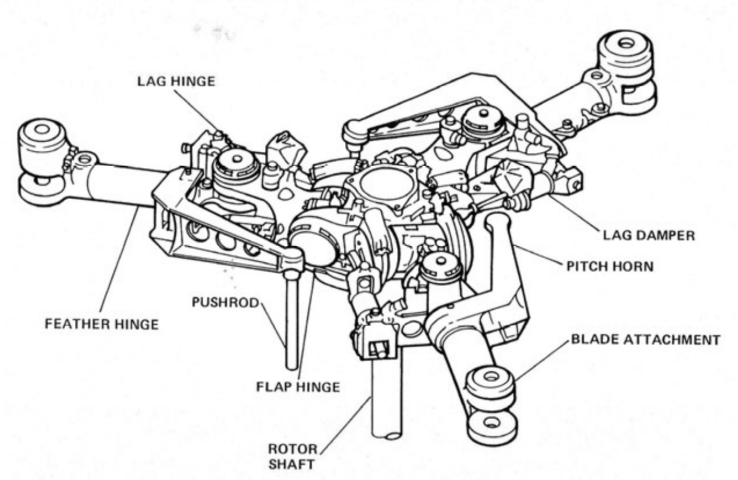


Figure 5: Boeing Rotorcraft Systems CH-46 fully-articulated rotor hub [4]

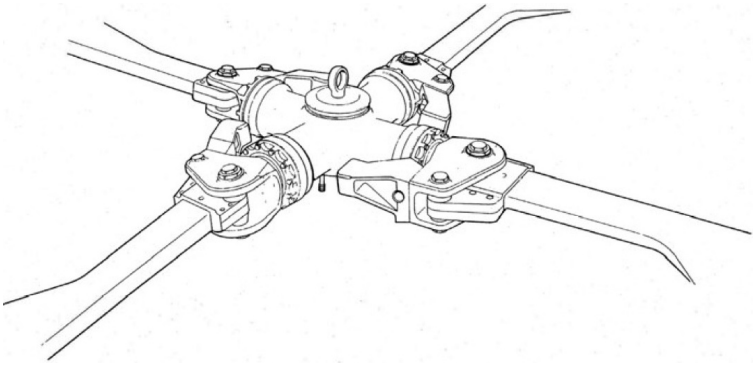


Figure 6: Messerschmitt-Bölkow-Blohn BO-105 hingeless rotor hub [4]

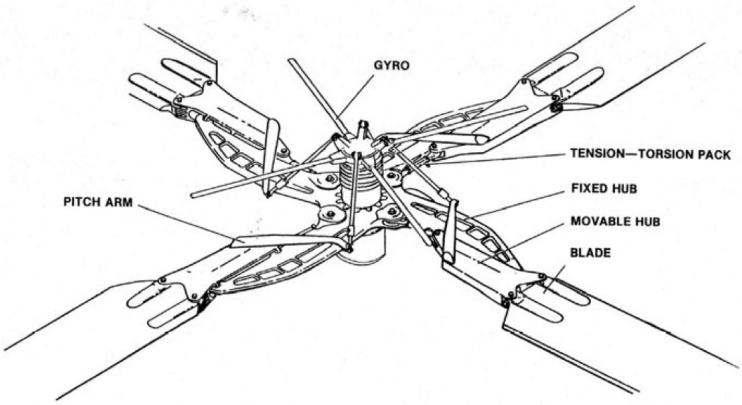


Figure 7: Lockheed AH-56 bearingless rotor hub [4]

Appendix B: Chapter 2 Figures and Tables



Figure 8: Boeing-Sikorsky SB>1 Defiant coaxial rotor helicopter [104]



Figure 9: Boeing CH-47 Chinook tandem rotor helicopter [105]



Figure 10: Kaman K-MAX intermeshing rotor helicopter [5]

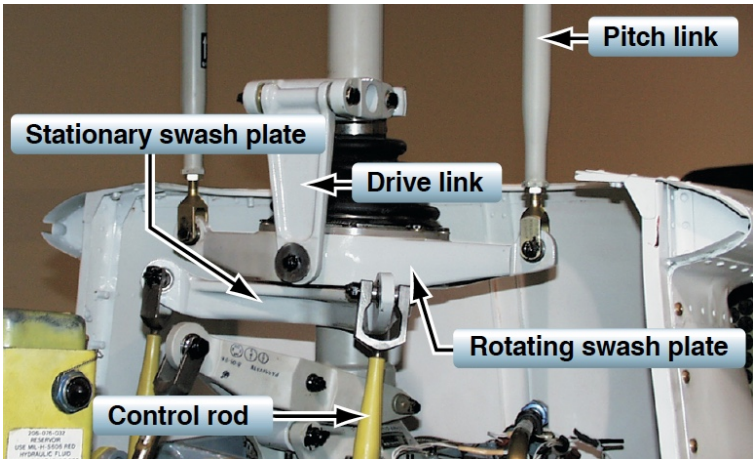


Figure 11: Helicopter swashplate geometry [5]

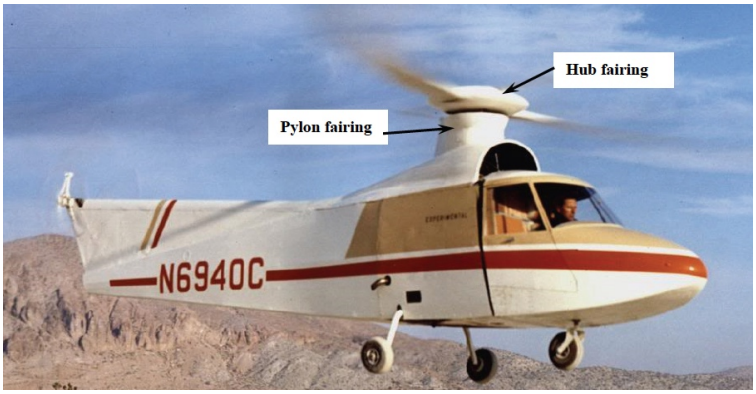


Figure 12: Lockheed CL-475 with pylon and hub fairing [4]



Figure 13: Boeing MH-139A with "beanie" hub fairing [106]

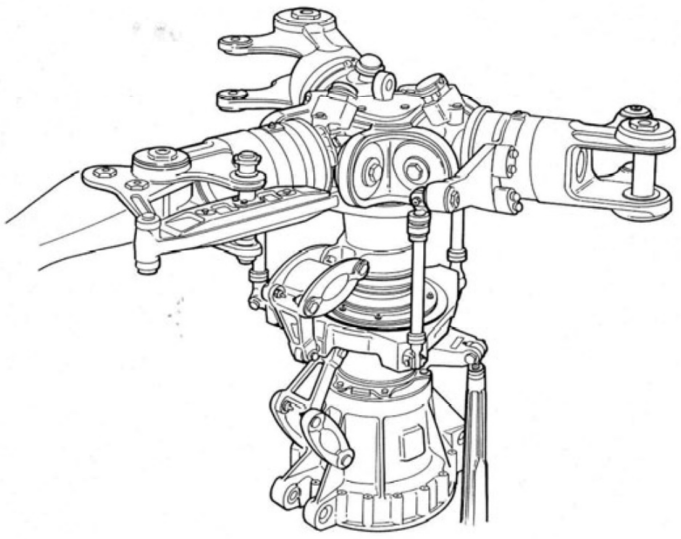


Figure 14: Aerospatiale SA 342 fully-articulated rotor hub [4]

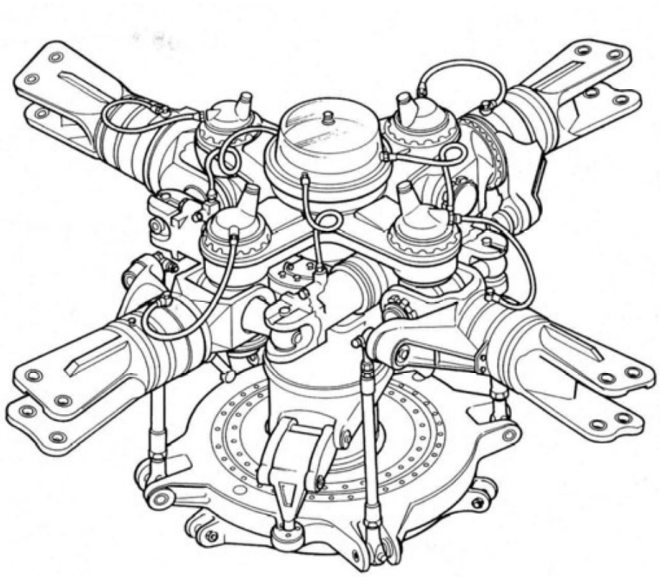


Figure 15: Aerospatiale SA 330 fully-articulated rotor hub [4]

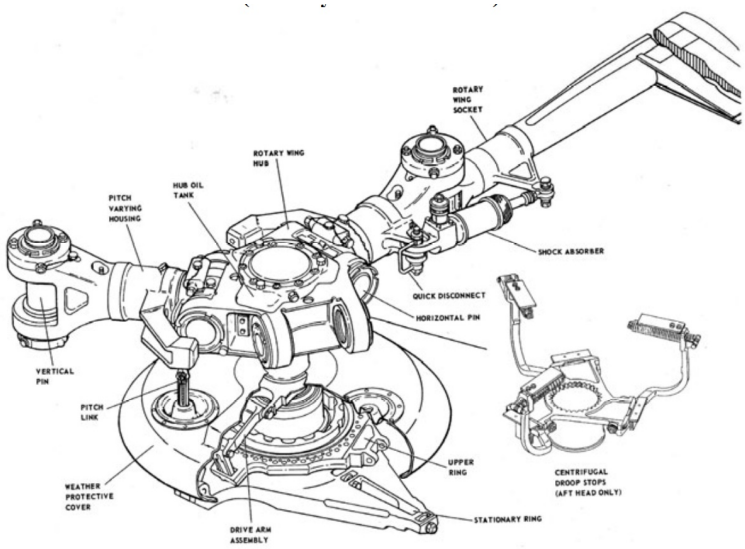


Figure 16: Boeing CH-47 fully-articulated rotor hub [4]



Figure 17: Bell Model 47 [4]

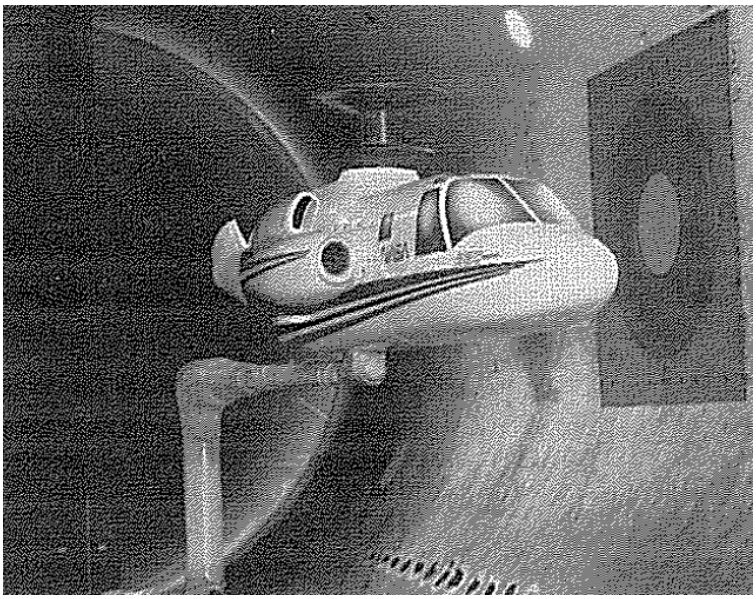
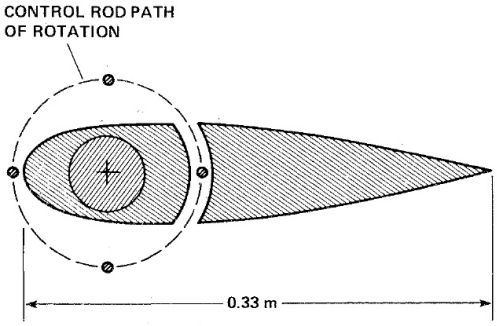
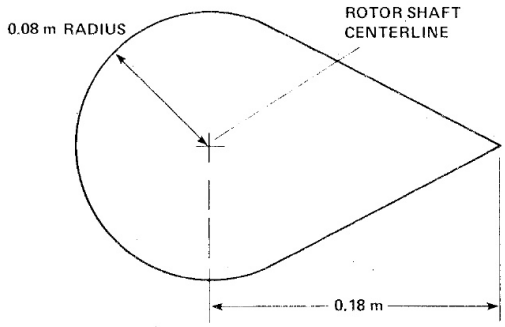


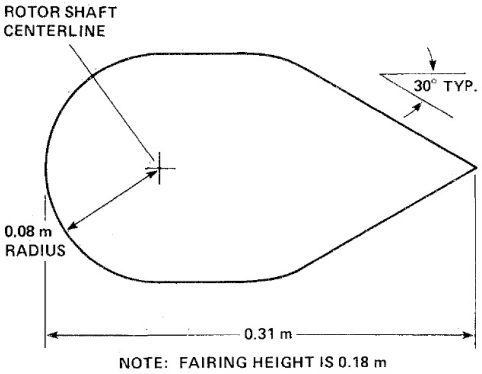
Figure 18: XH-59A Advancing Blade Concept helicopter [27]



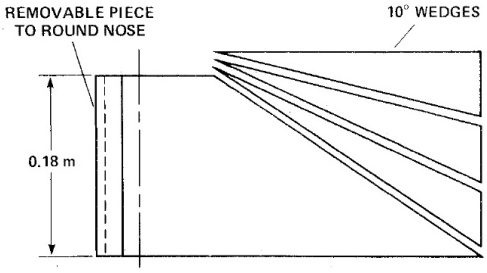
(a) NACA 0012 dual-component shaft fairing



(b) Baseline shaft fairing



(c) Teardrop shaft fairing



(d) Tested shaft fairing planform modifications

Figure 19: Shaft fairings tested on the XH-59A [28]

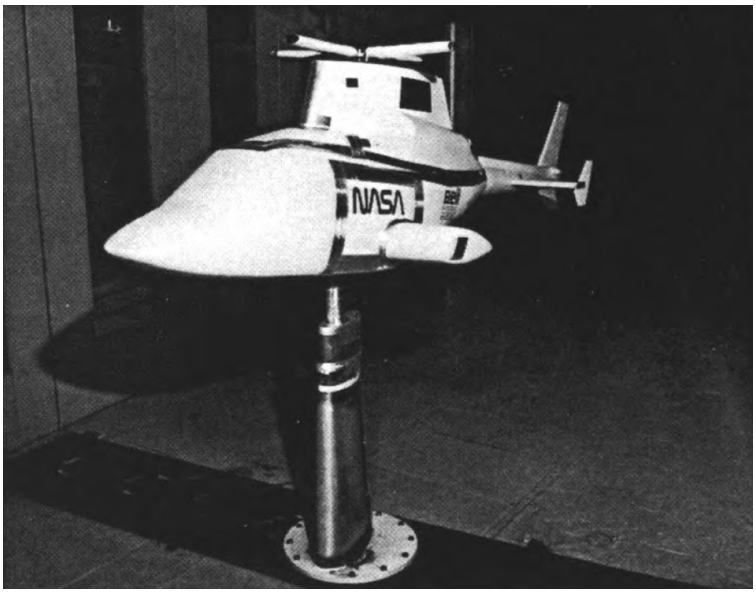


Figure 20: Bell Helicopter Textron Model 222 helicopter [32]

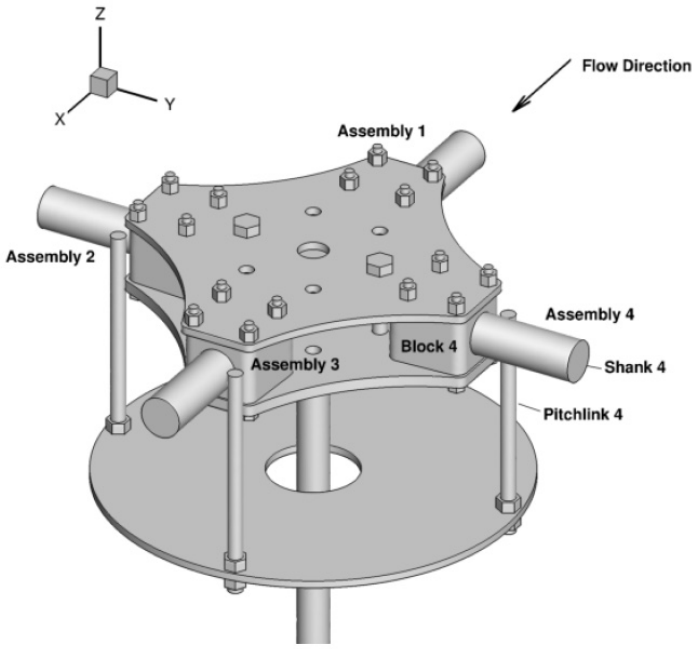


Figure 21: GIT rotor hub model [39]

Appendix C: Chapter 3 Figures and Tables

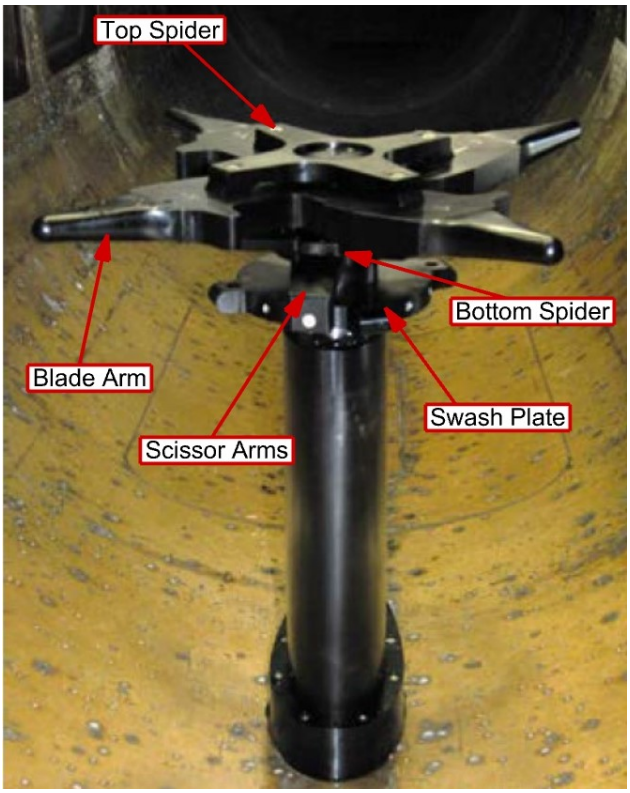
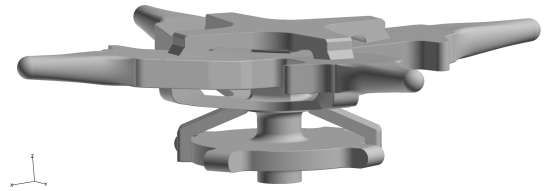


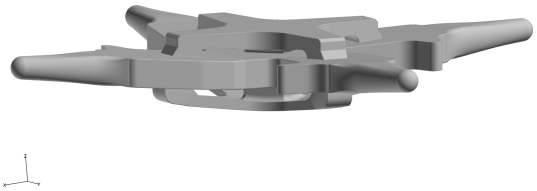
Figure 22: Phase III hub experimental model, modified from Ref. [68]

Table 1: Rotor Hub Grid Cell Count

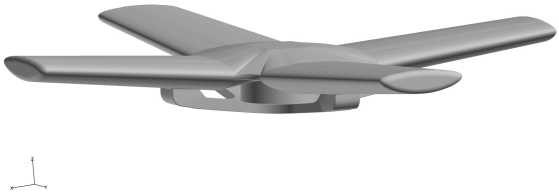
Hub	Grid Points
Baseline	53.7×10^6
Defeatured	35.7×10^6
Low Drag	28.5×10^6
Phase III	55.9×10^6



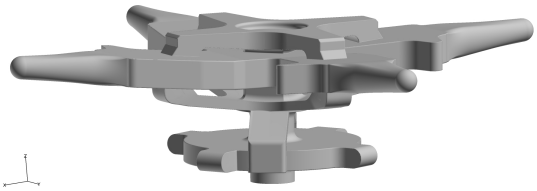
(a) Baseline hub



(b) Defeatured hub

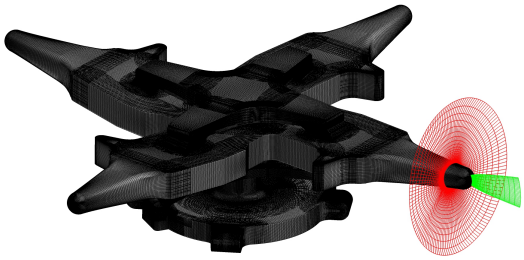


(c) Low Drag hub

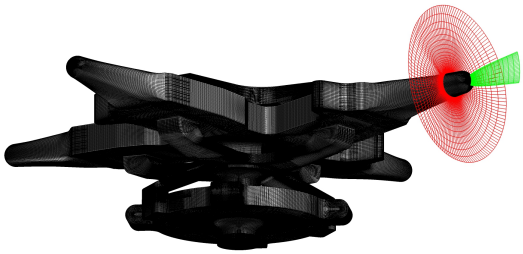


(d) Phase III hub

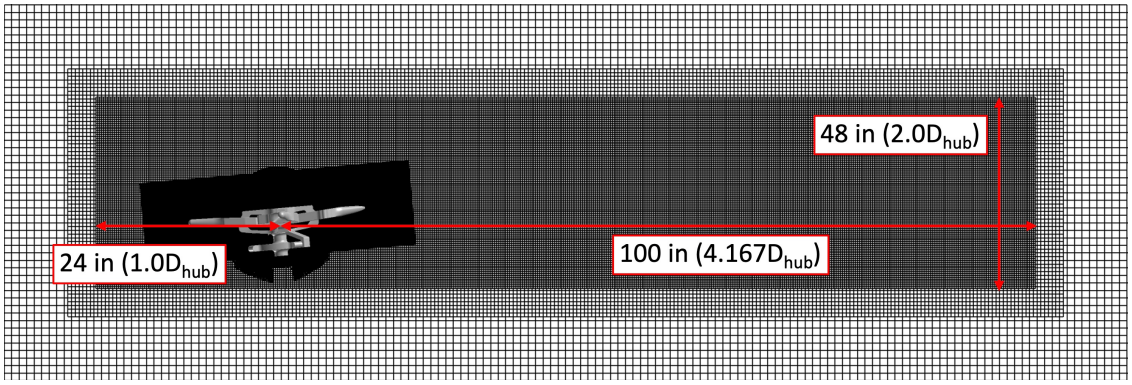
Figure 23: Rotor hub geometries



(a) Surface grid, upper side

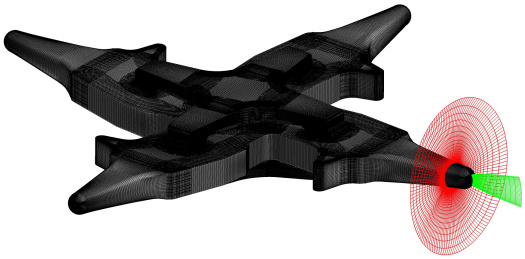


(b) Surface grid, lower side

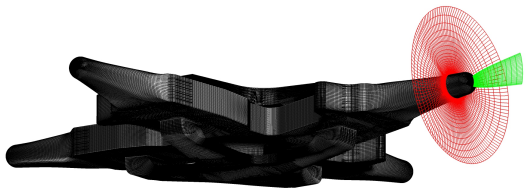


(c) Off-body grid

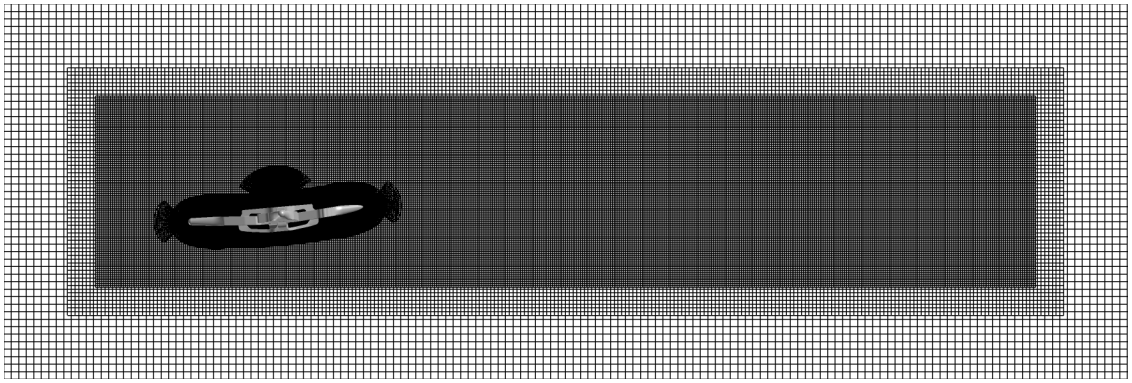
Figure 24: Baseline hub grid



(a) Surface grid, upper side

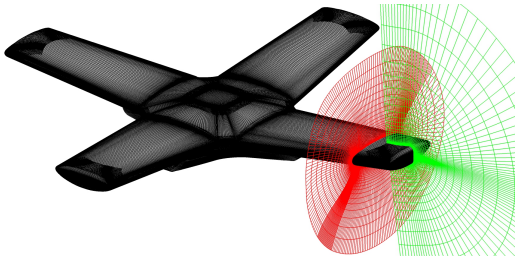


(b) Surface grid, lower side

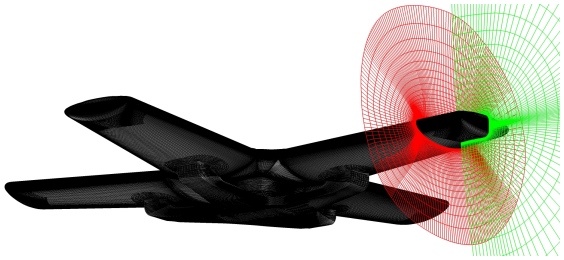


(c) Off-body grid

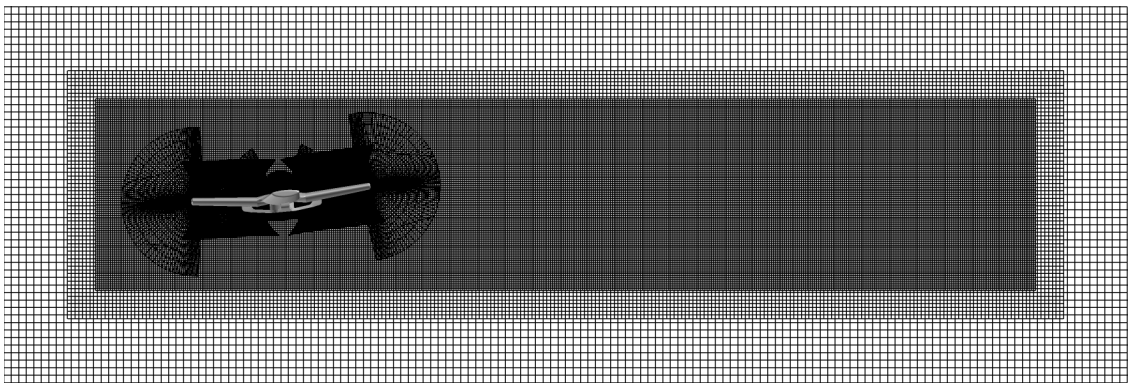
Figure 25: Defeatured hub grid



(a) Surface grid, upper side

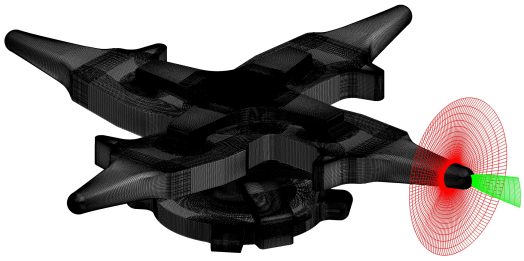


(b) Surface grid, lower side

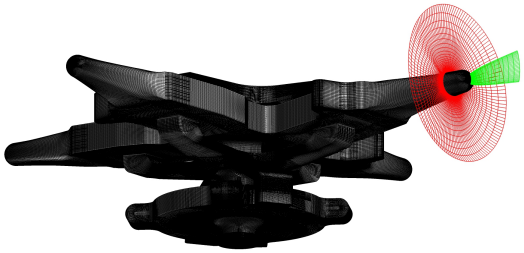


(c) Off-body grid

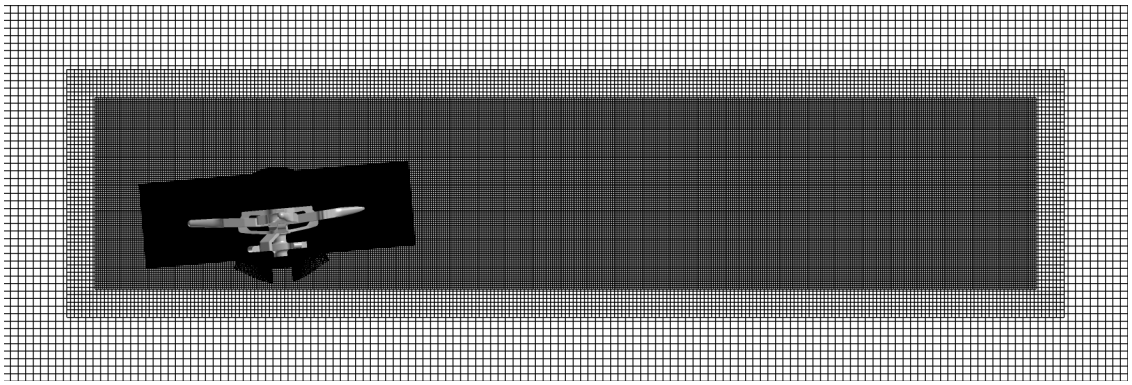
Figure 26: Low Drag hub grid



(a) Surface grid, upper side



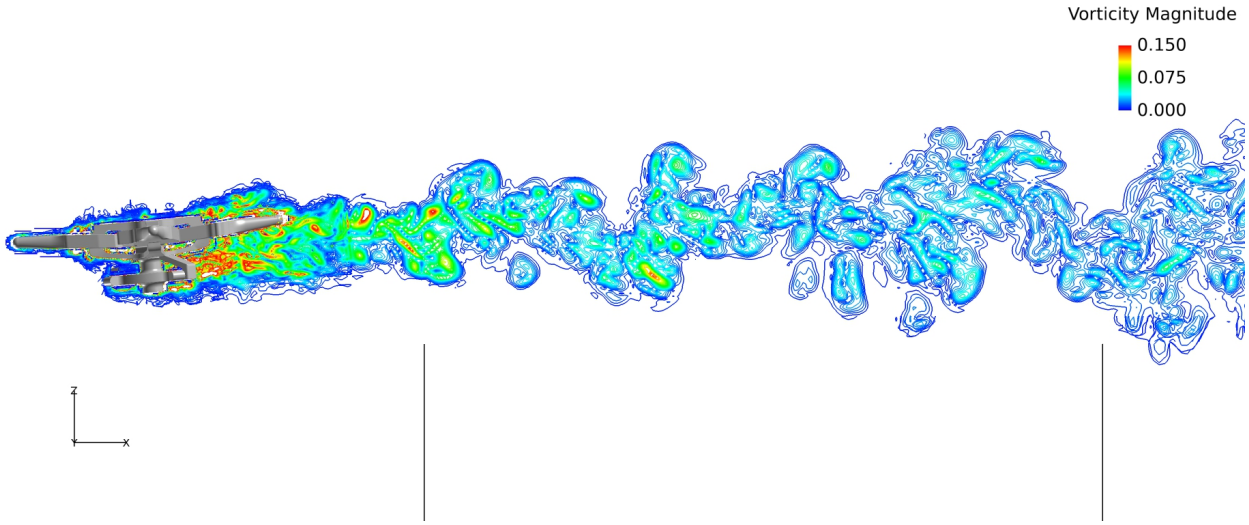
(b) Surface grid, lower side



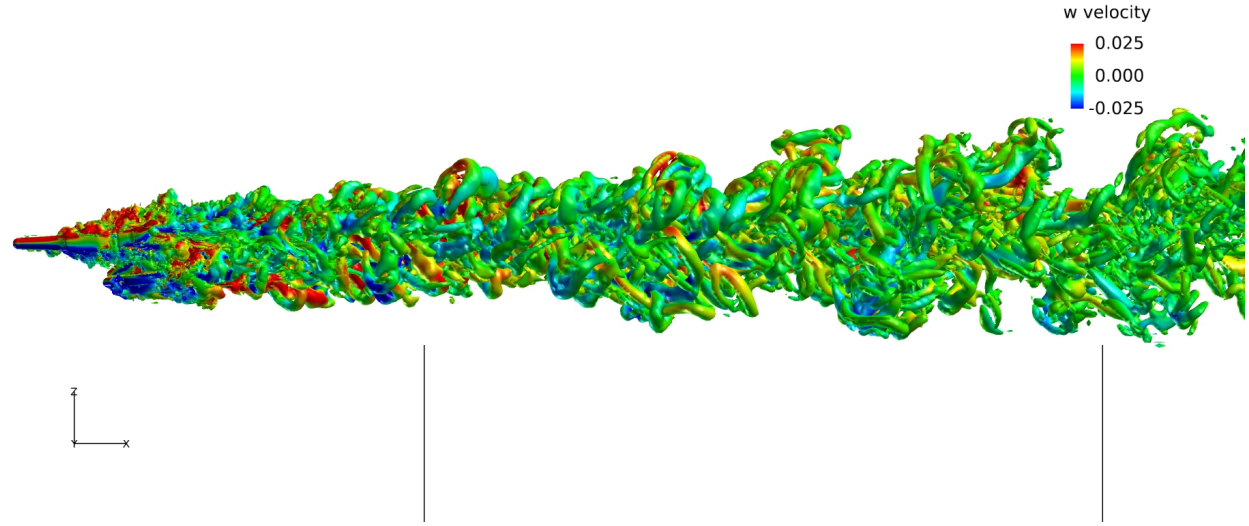
(c) Off-body grid

Figure 27: Phase III hub grid

Appendix D: Chapter 4 Figures and Tables



(a) Vorticity magnitude contours ($\omega D_{hub}/U_\infty$)

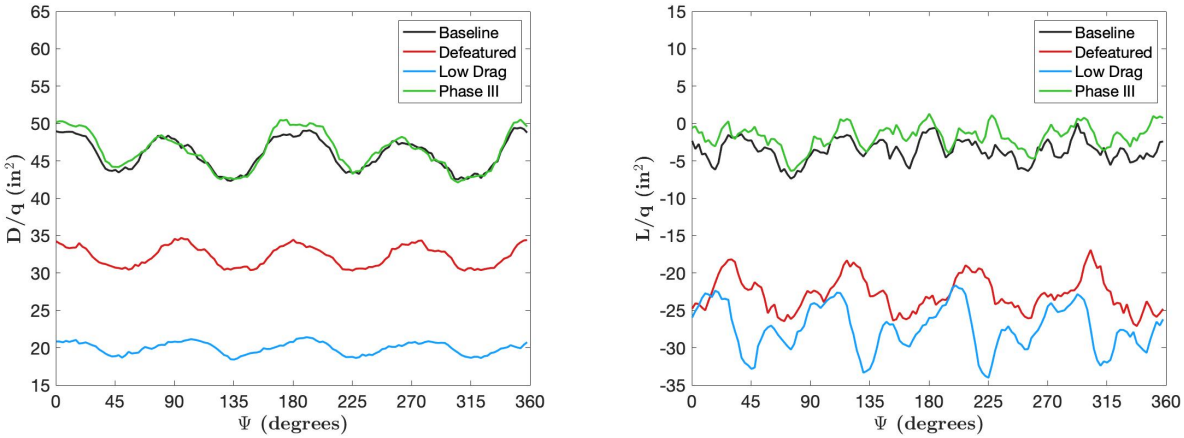


(b) Iso-surface of Q-criterion $\left(QD_{hub}^2/U_\infty^2 = 1 \times 10^{-4}\right)$

Figure 28: Instantaneous wake profiles of the Baseline hub

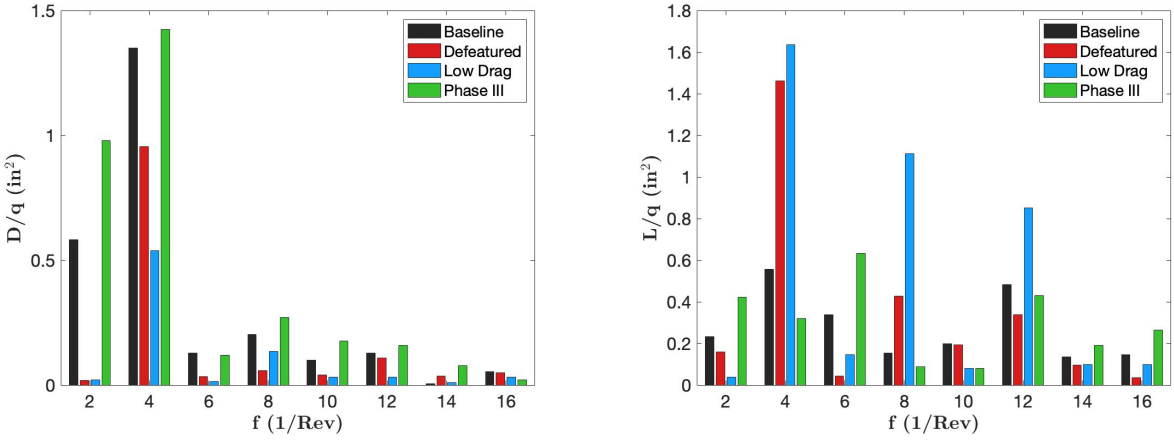
Table 2: Time-Averaged Flat Plate Areas

Rotor Hub	D/q (in^2)	L/q (in^2)
Experimental (Phase III)	52.80	-
Baseline	45.94	-3.580
Defeatured	32.25	-22.83
Low Drag	19.98	-27.33
Phase III	46.39	-1.716



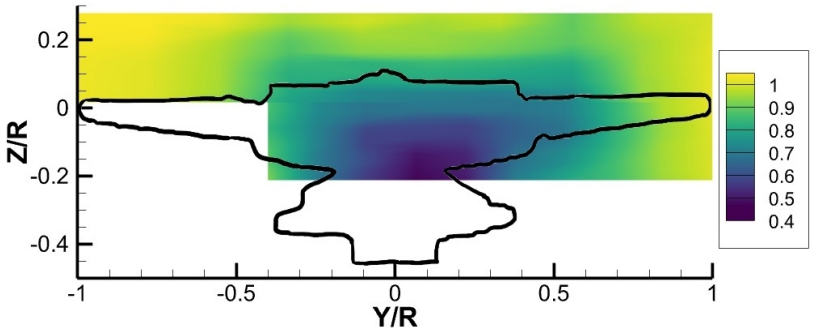
(a) Equivalent flat plate drag area (b) Equivalent flat plate lift area

Figure 29: Phase-averaged rotor hub equivalent flat plate areas

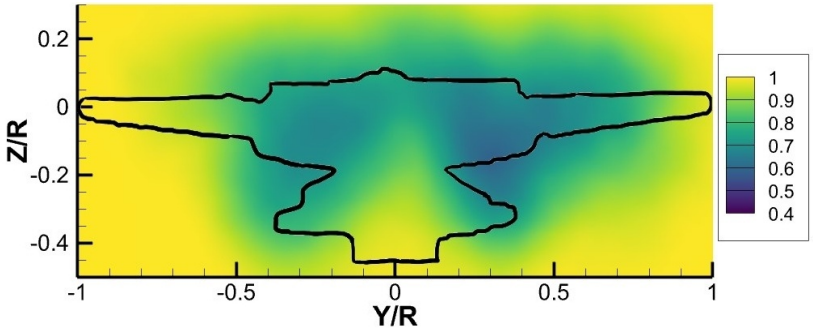


(a) Equivalent flat plate drag area (b) Equivalent flat plate lift area

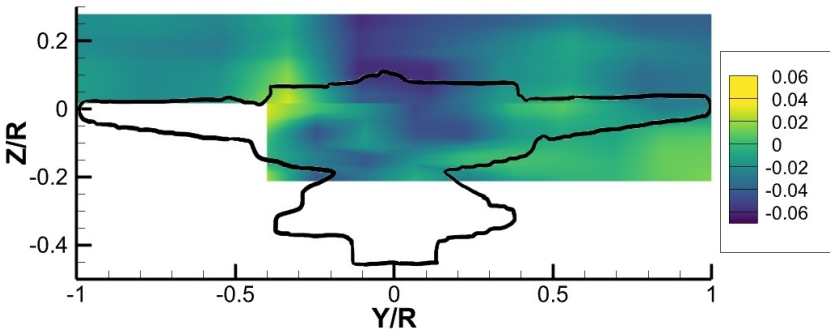
Figure 30: DFT of rotor hub equivalent flat plate areas



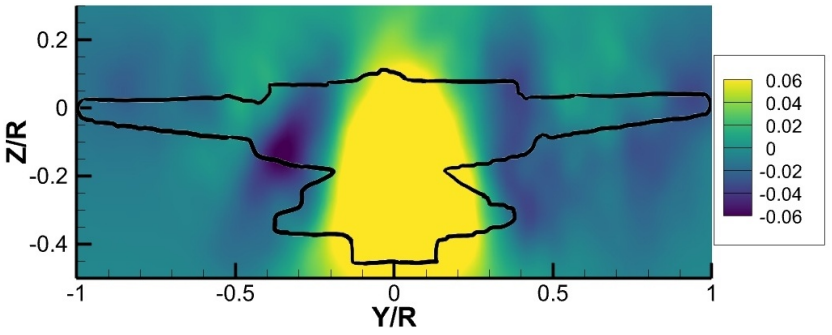
(a) Mean u-velocity, experimental



(b) Mean u-velocity, CFD

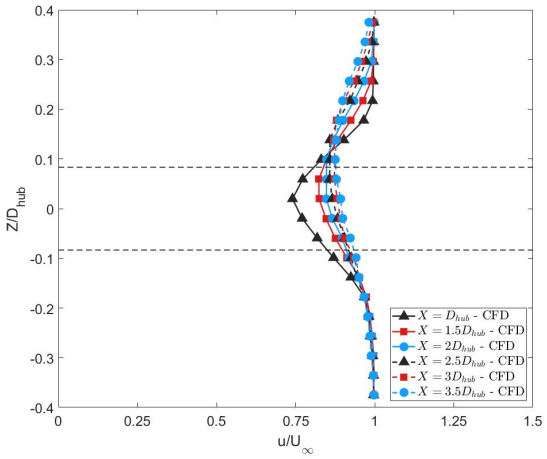


(c) Mean w-velocity, experimental

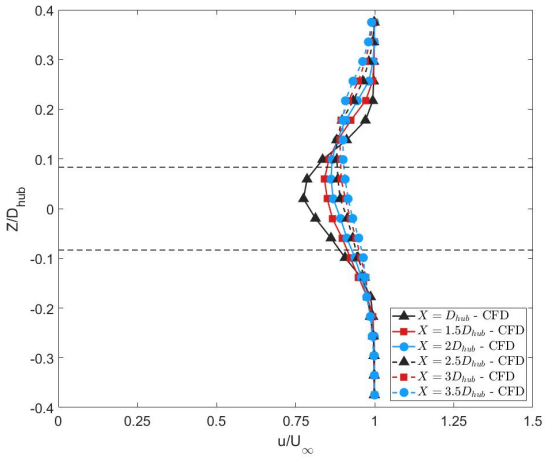


(d) Mean w-velocity, CFD

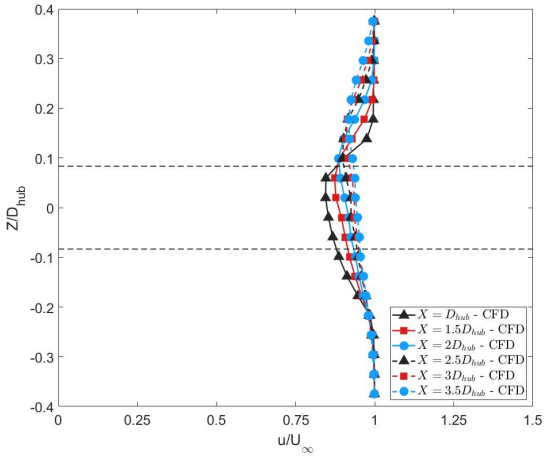
Figure 31: Time-averaged velocity contours of the Phase III hub, $x = D_{hub}$



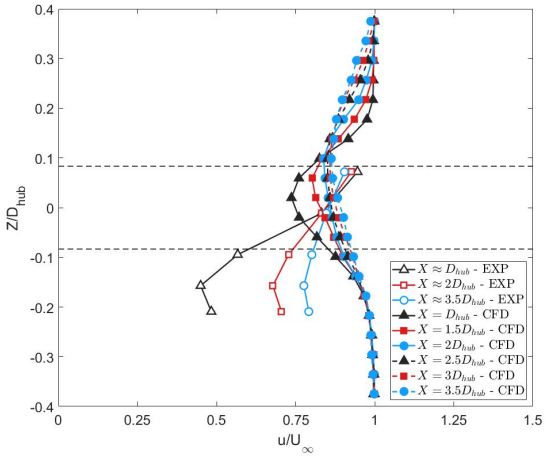
(a) Baseline hub



(b) Defeatured hub

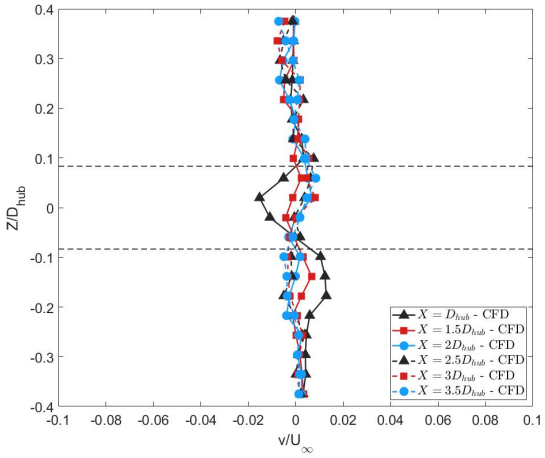


(c) Low Drag hub

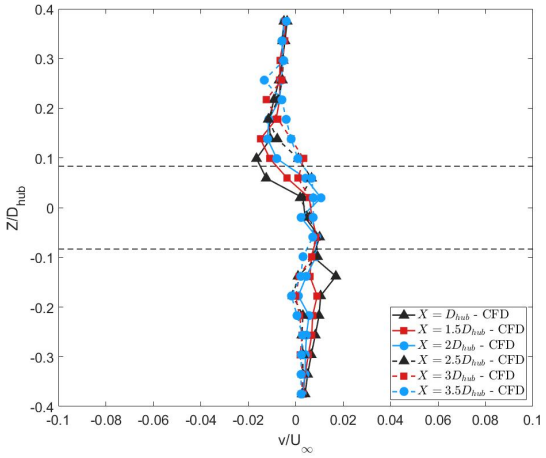


(d) Phase III hub

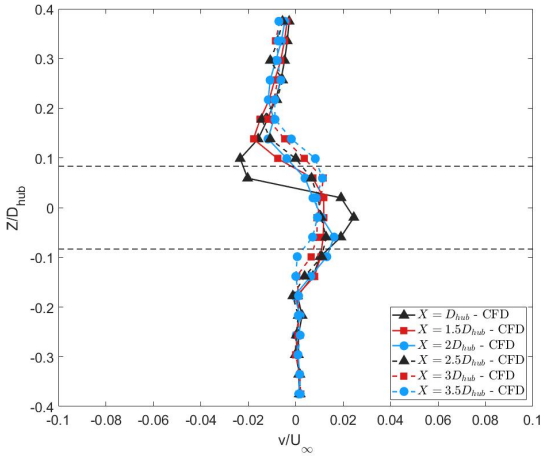
Figure 32: Time-averaged stream-wise velocity profiles, $y = 0$, experimental and CFD



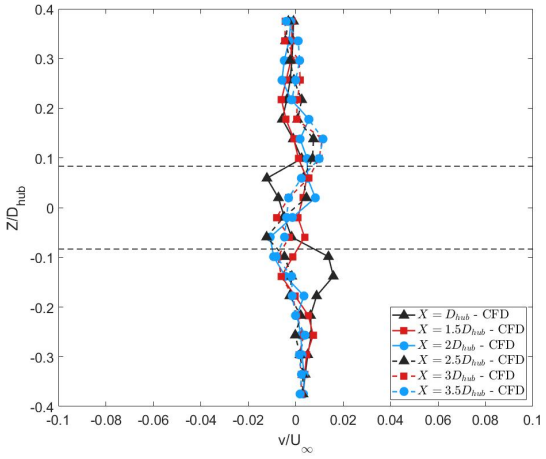
(a) Baseline hub



(b) Defeatured hub

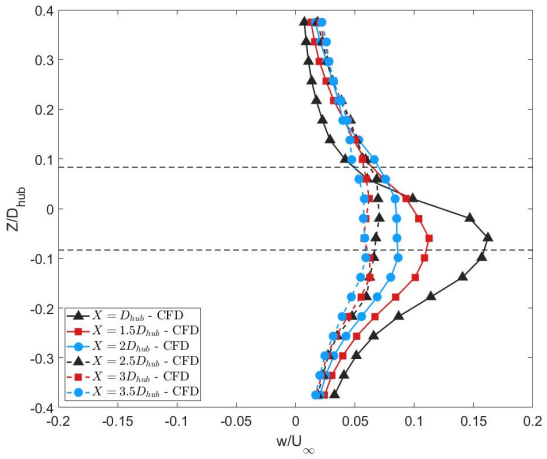


(c) Low Drag hub

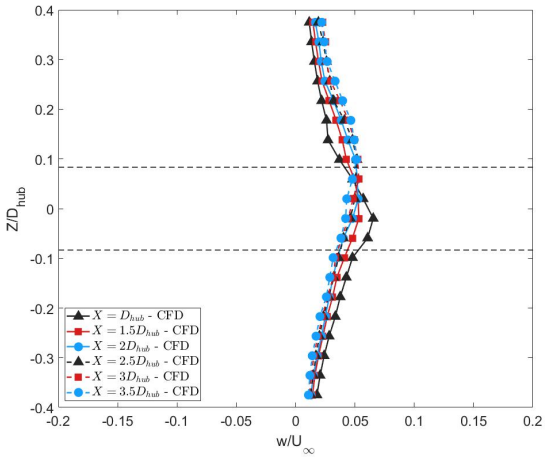


(d) Phase III hub

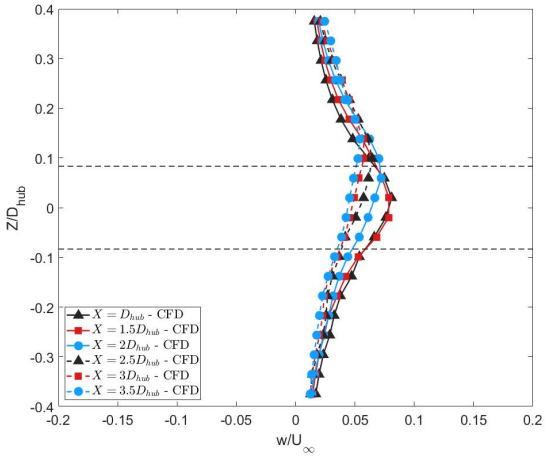
Figure 33: Time-averaged span-wise velocity profiles, $y = 0$, CFD



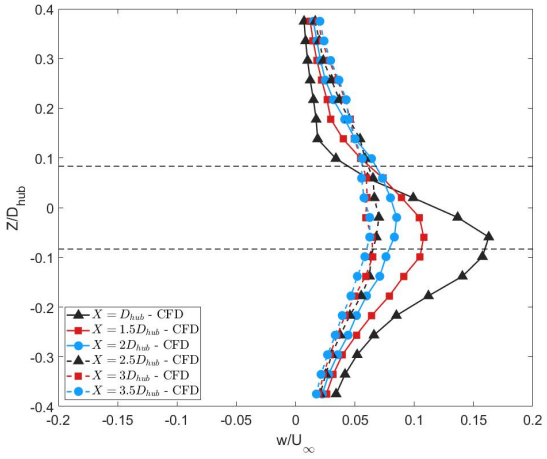
(a) Baseline hub



(b) Defeatured hub



(c) Low Drag hub



(d) Phase III hub

Figure 34: Time-averaged vertical velocity profiles, $y = 0$, CFD

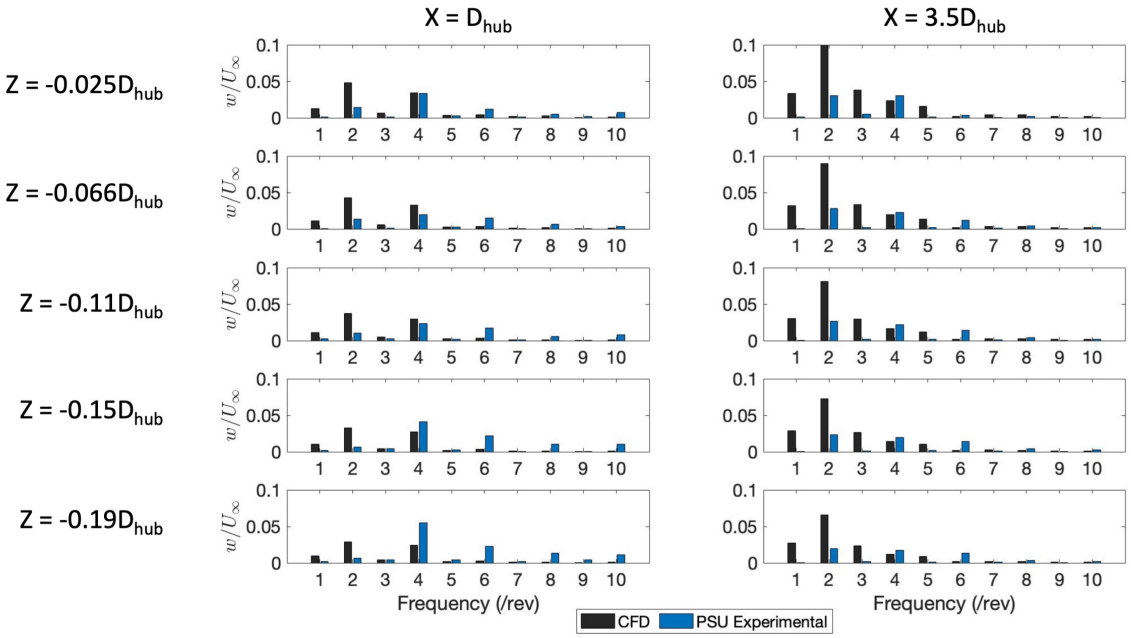
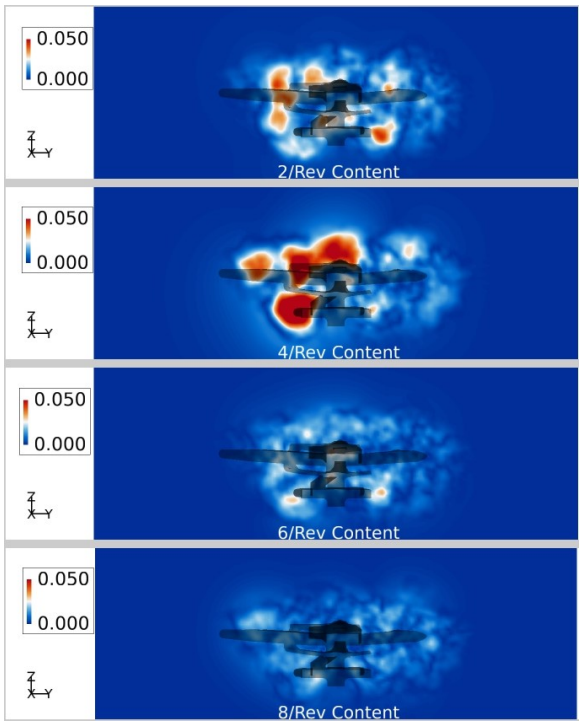
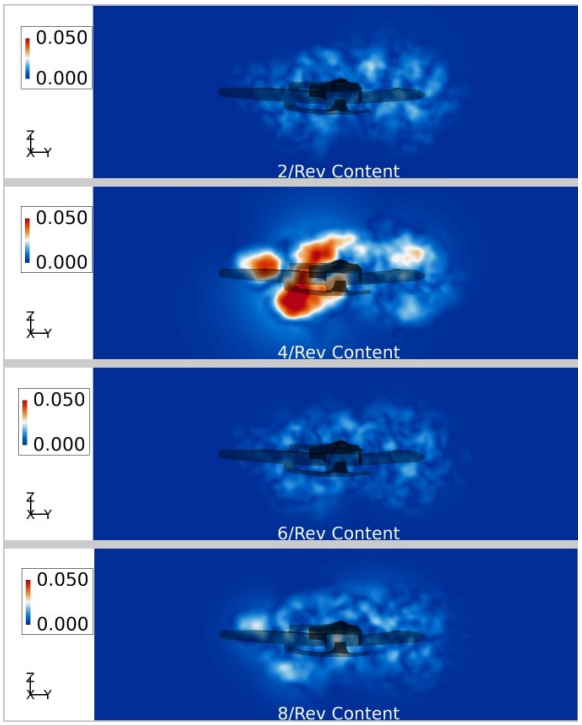


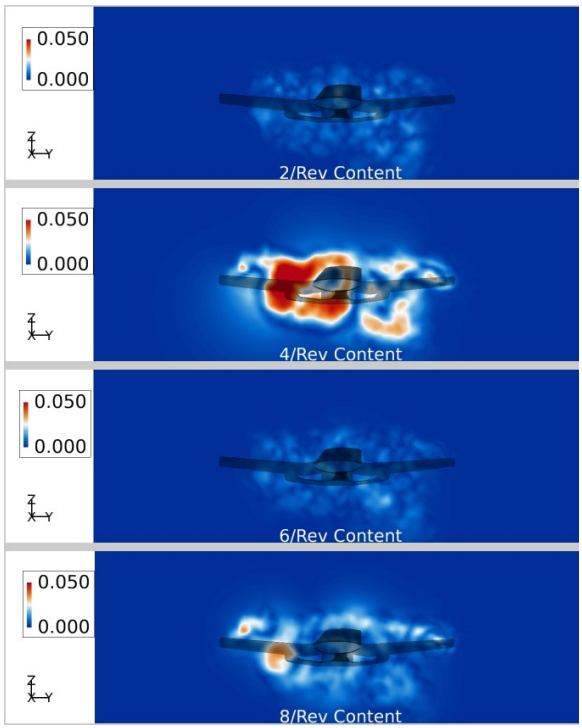
Figure 35: Vertical velocity harmonics, $y = 0$



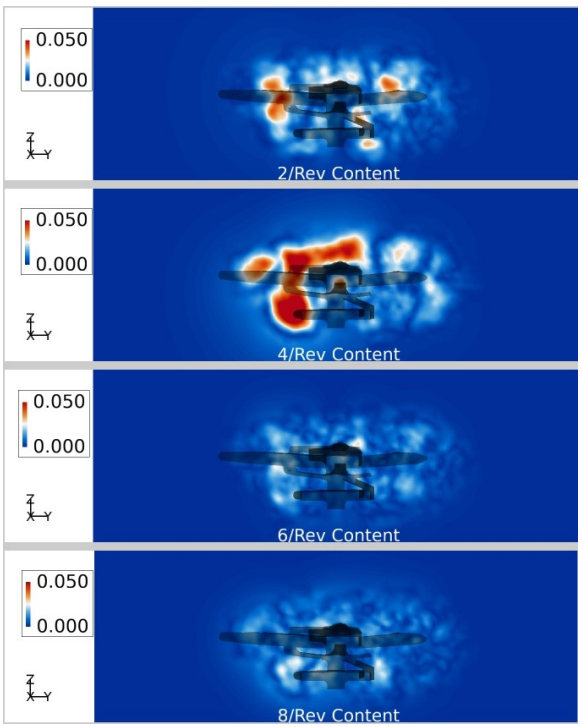
(a) Baseline hub



(b) Defeatured hub

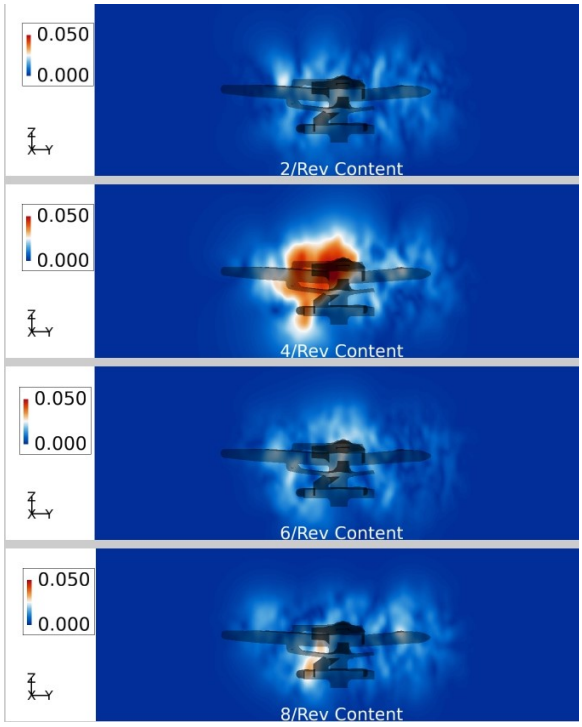


(c) Low Drag hub

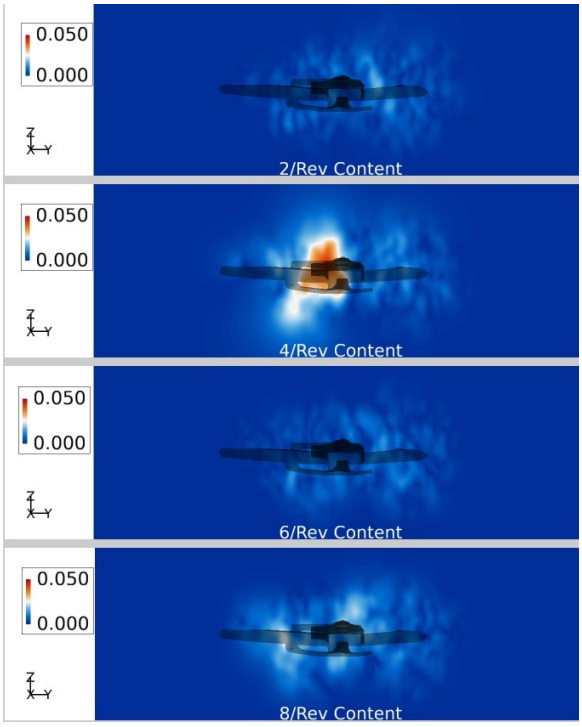


(d) Phase III hub

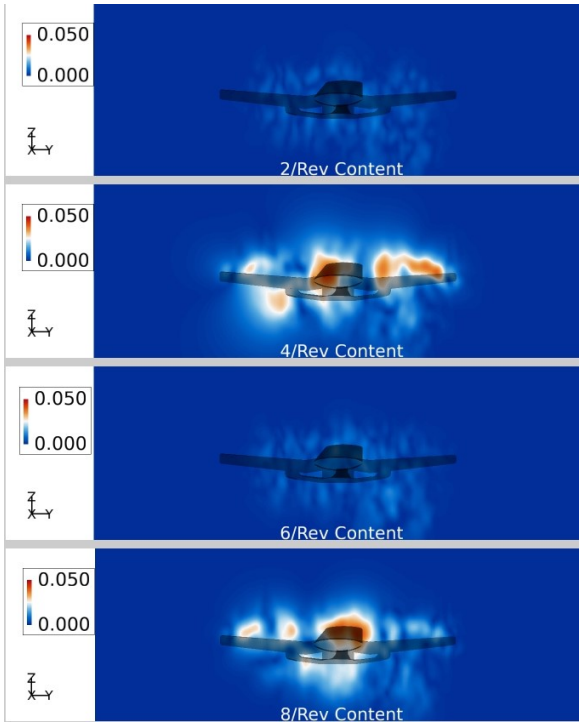
Figure 36: Streamwise velocity fluctuations, $x = D_{hub}$



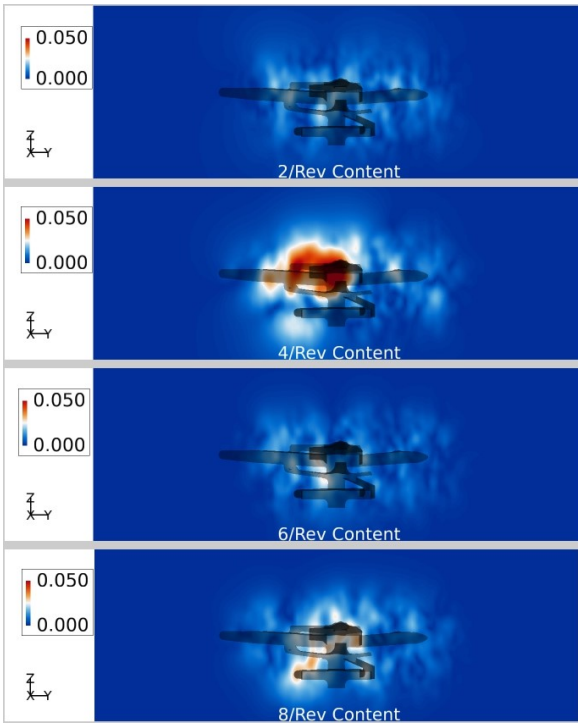
(a) Baseline hub



(b) Defeatured hub



(c) Low Drag hub



(d) Phase III hub

Figure 37: Vertical velocity fluctuations, $x = D_{hub}$

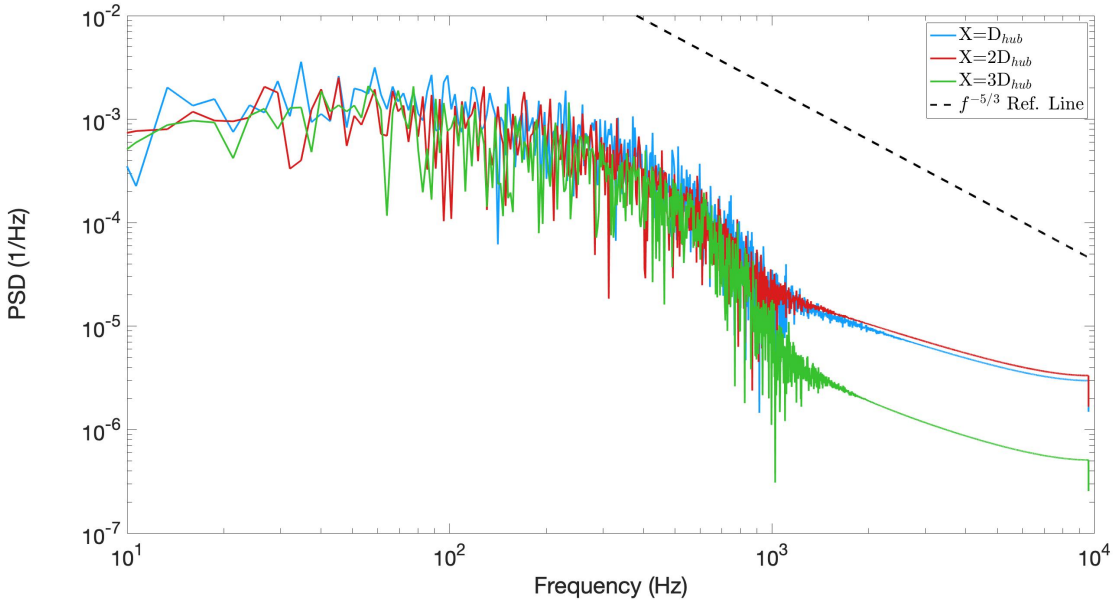
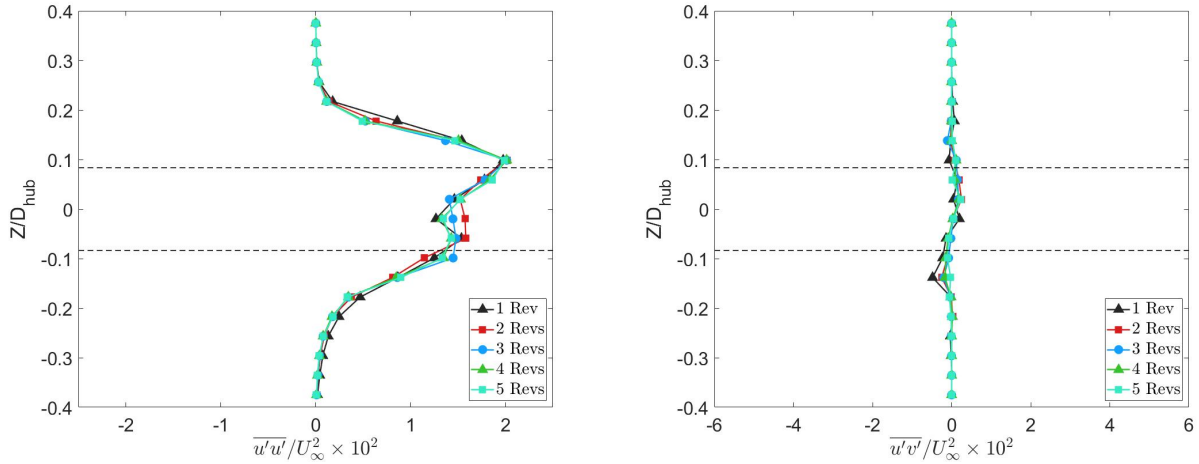
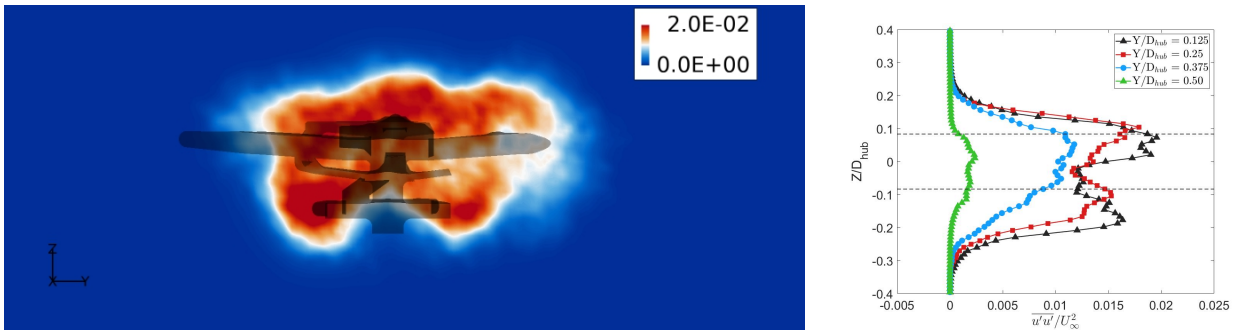


Figure 38: PSD of the stream-wise momentum in the Baseline hub wake

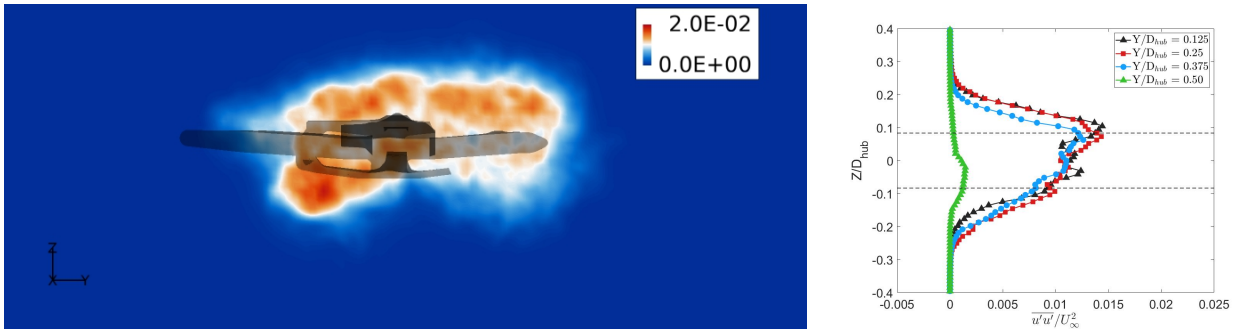


(a) $\overline{u'u'}/U_\infty^2$ profiles (b) $\overline{u'v'}/U_\infty^2$ profiles

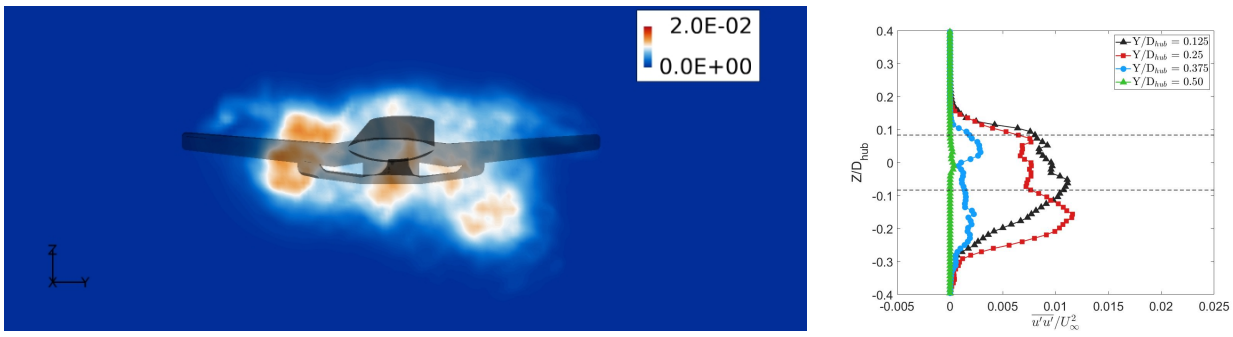
Figure 39: Reynolds stress data convergence, $y = 0$ and $x = D_{hub}$



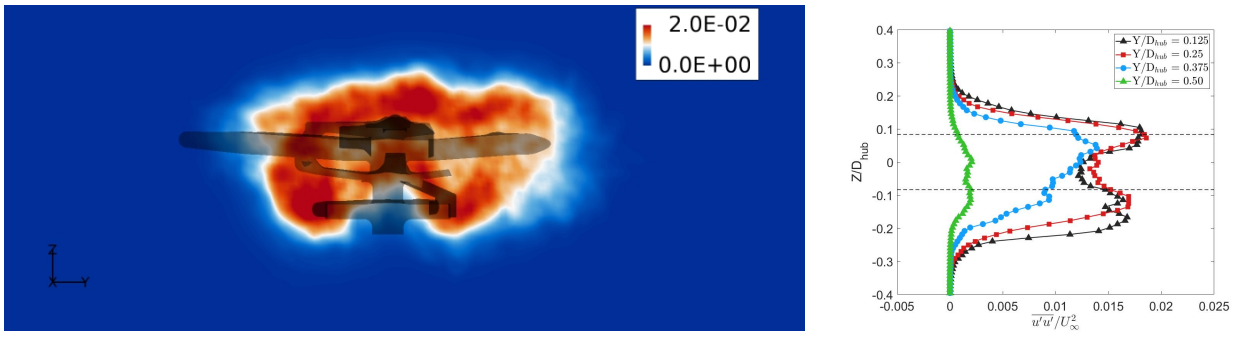
(a) Baseline hub



(b) Defeatured hub

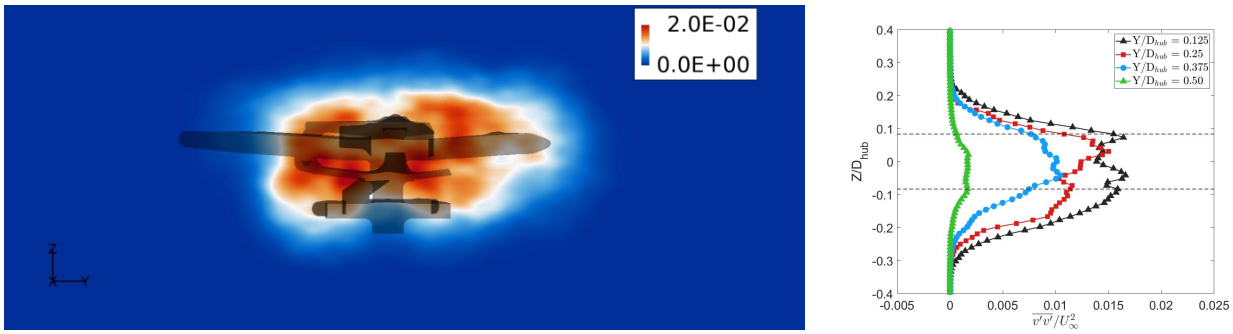


(c) Low Drag hub

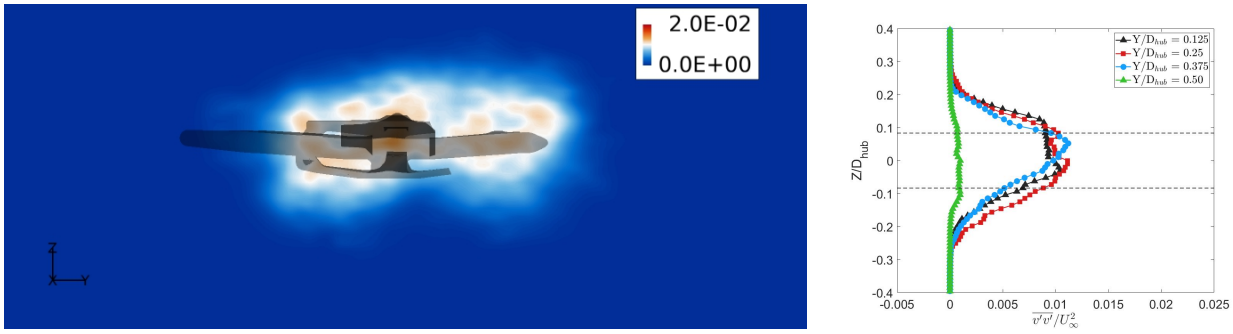


(d) Phase III hub

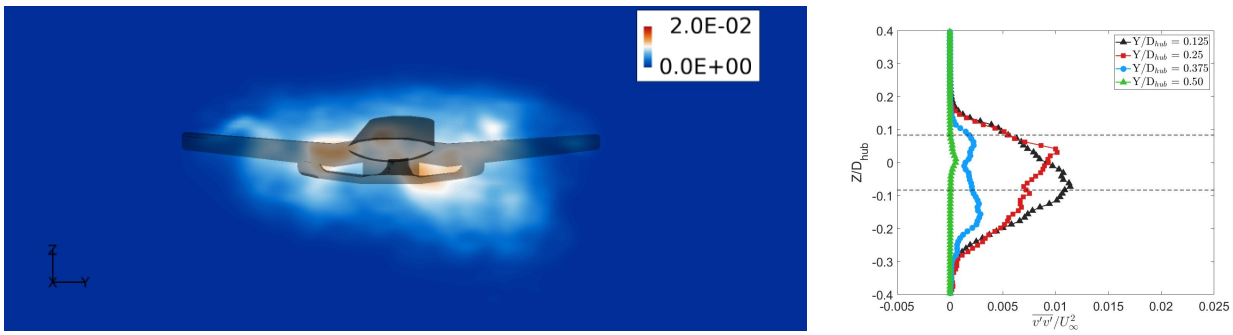
Figure 40: Normalized Reynolds stress $\overline{u'u'}/U_\infty^2$, $x = D_{hub}$



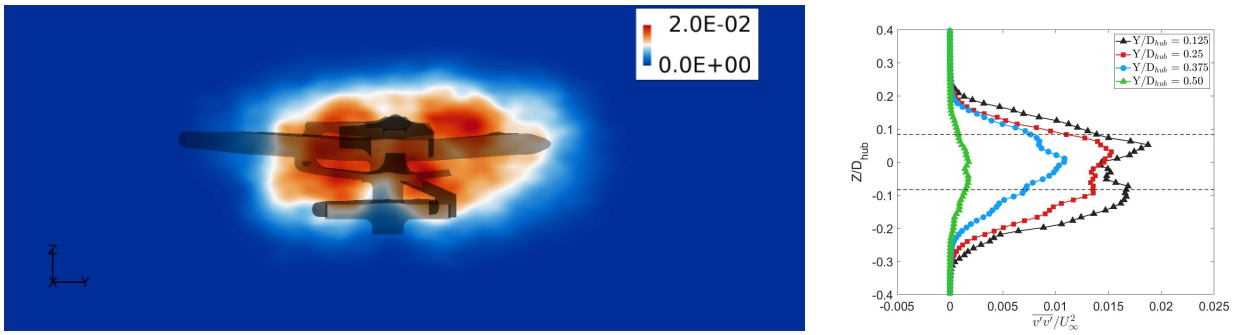
(a) Baseline hub



(b) Defeatured hub

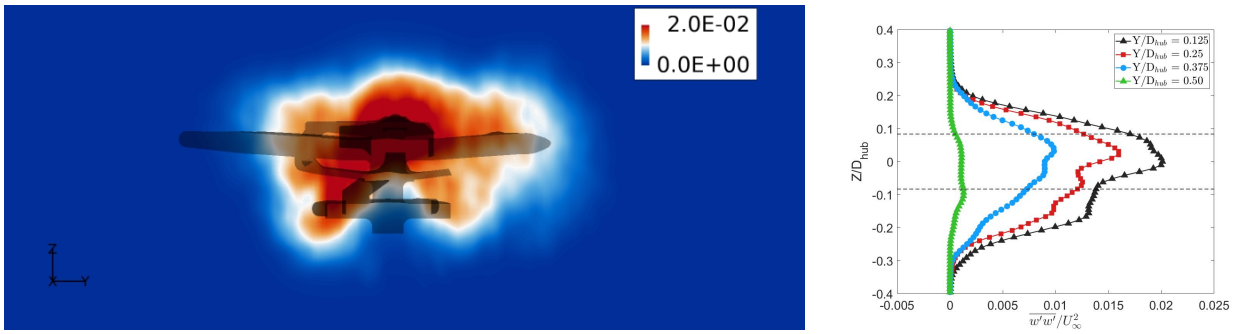


(c) Low Drag hub

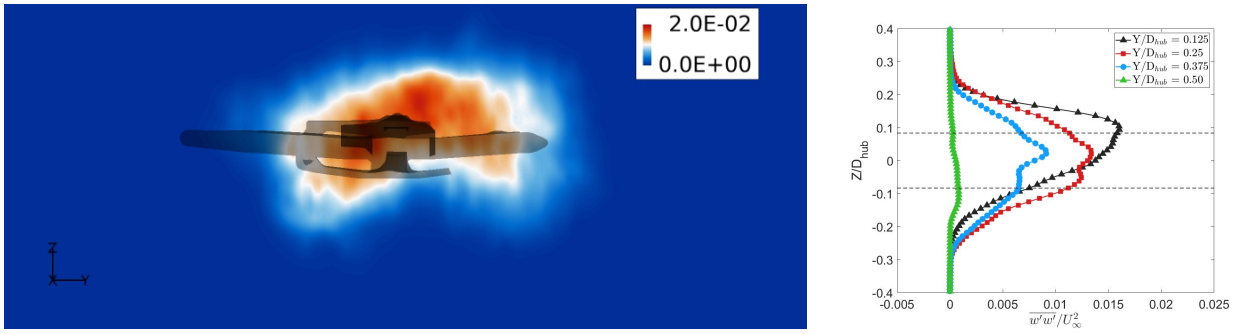


(d) Phase III hub

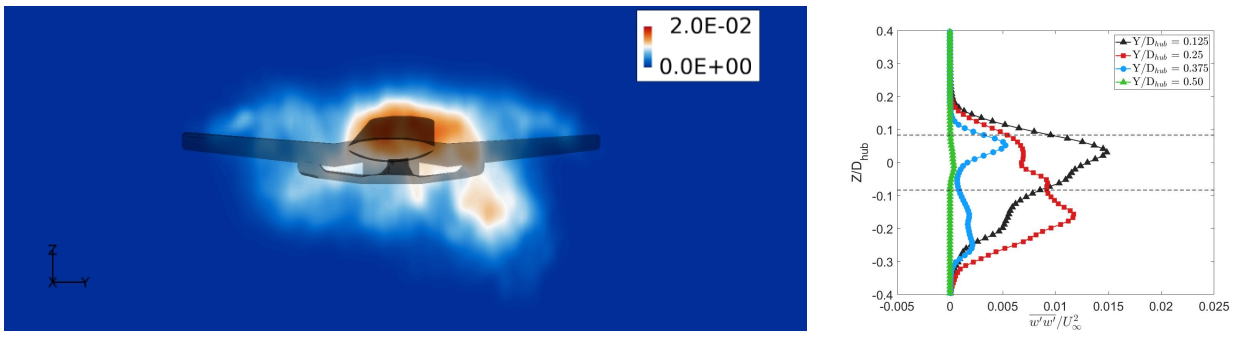
Figure 41: Normalized Reynolds stress $\overline{v'v'}/U_\infty^2$, $x = D_{hub}$



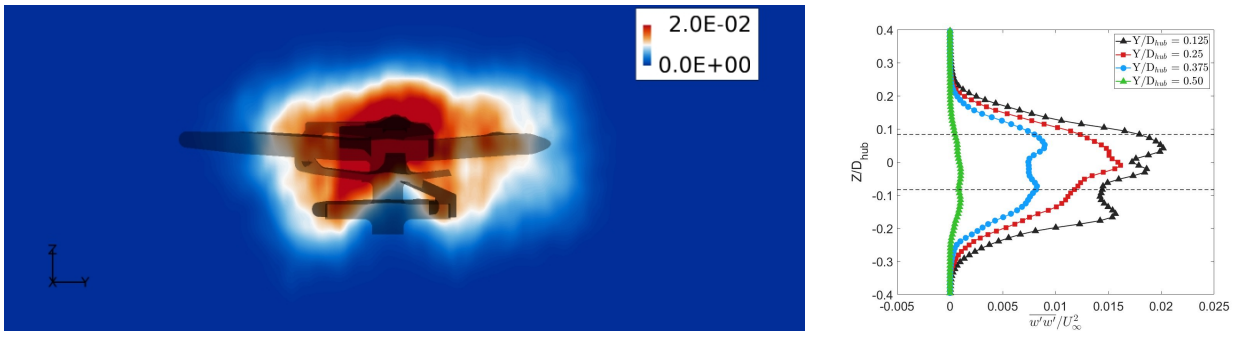
(a) Baseline hub



(b) Defeatured hub

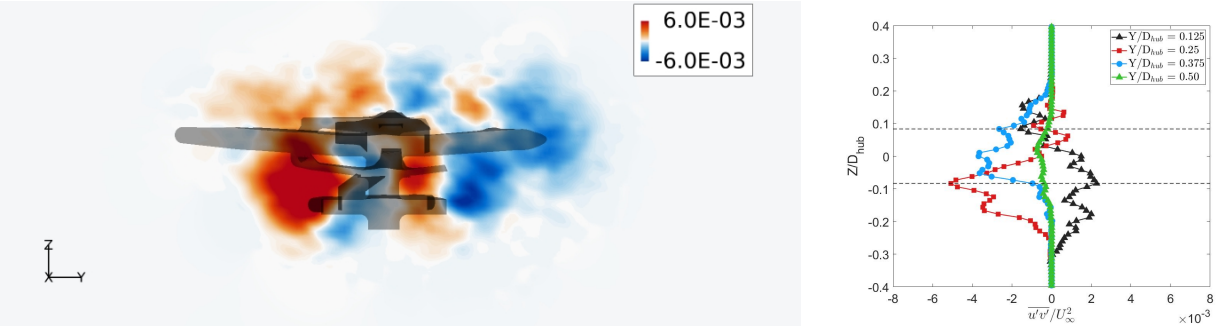


(c) Low Drag hub

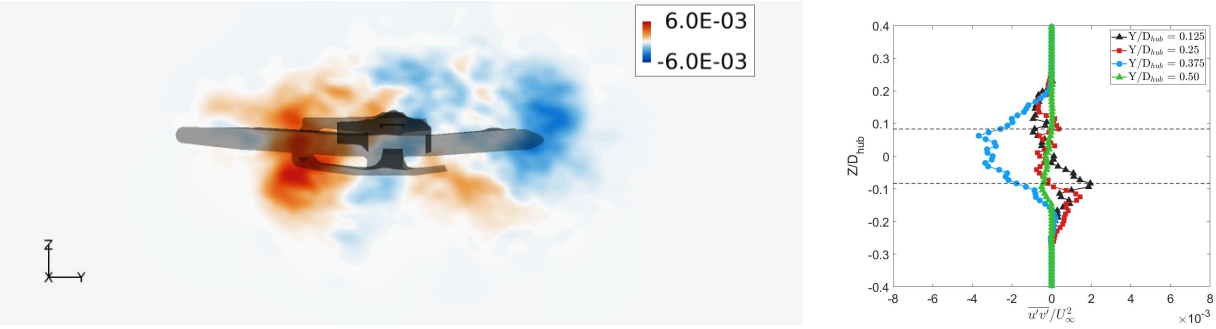


(d) Phase III hub

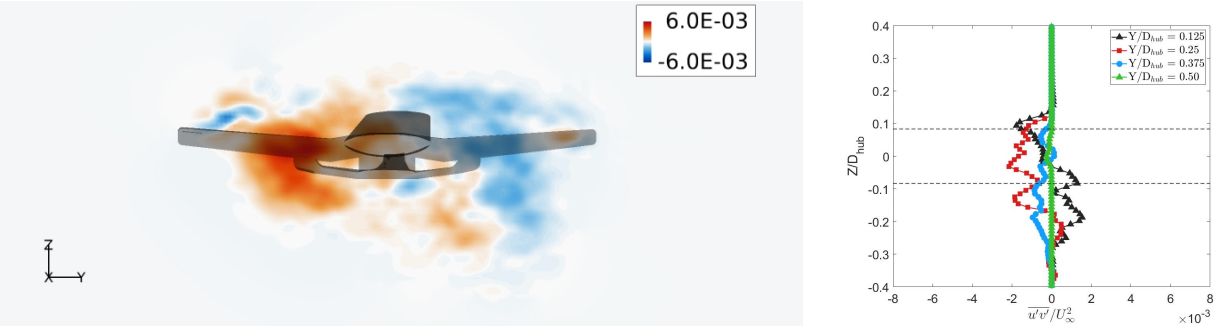
Figure 42: Normalized Reynolds stress $\overline{w'w'}/U_\infty^2$, $x = D_{hub}$



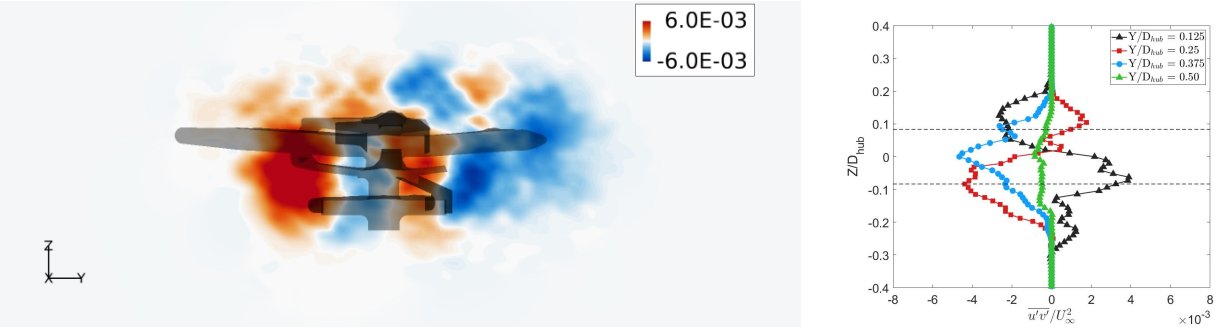
(a) Baseline hub



(b) Defeatured hub

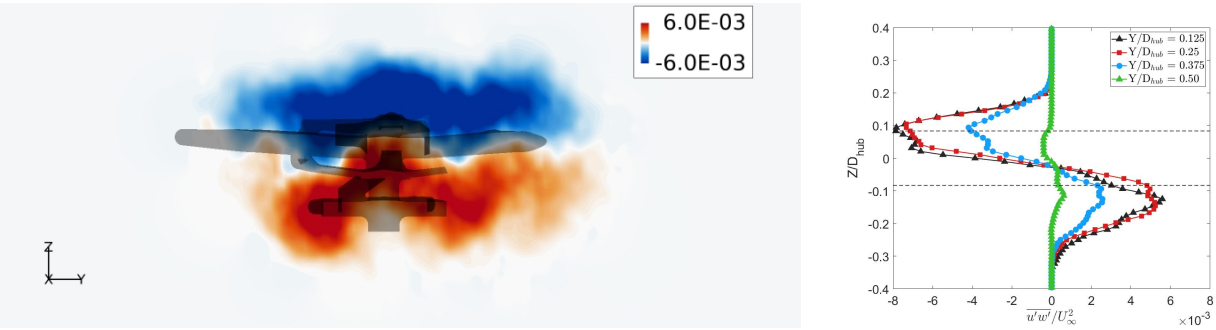


(c) Low Drag hub

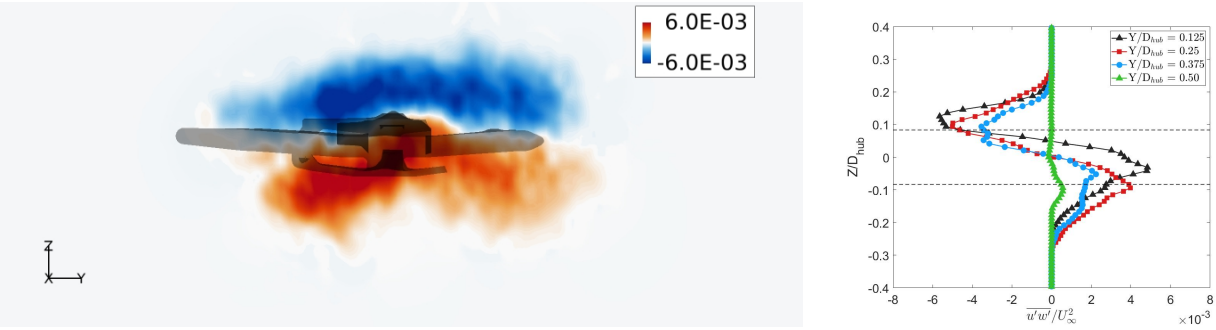


(d) Phase III hub

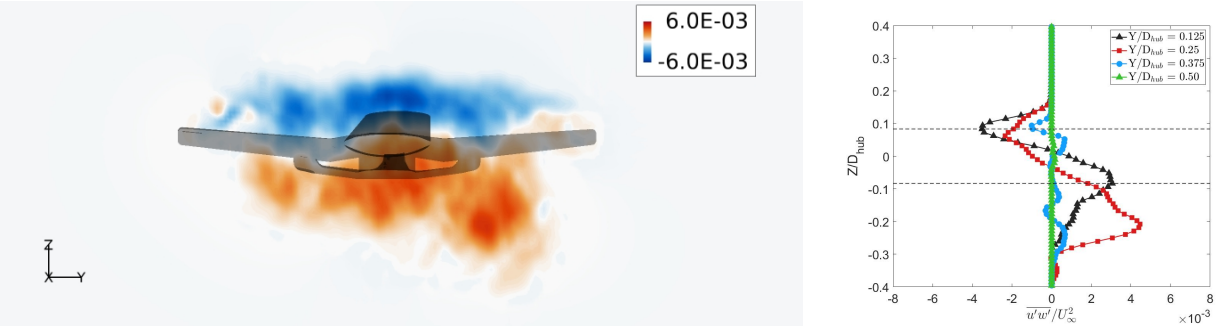
Figure 43: Normalized Reynolds stress $\overline{u'v'}/U_\infty^2$, $x = D_{hub}$



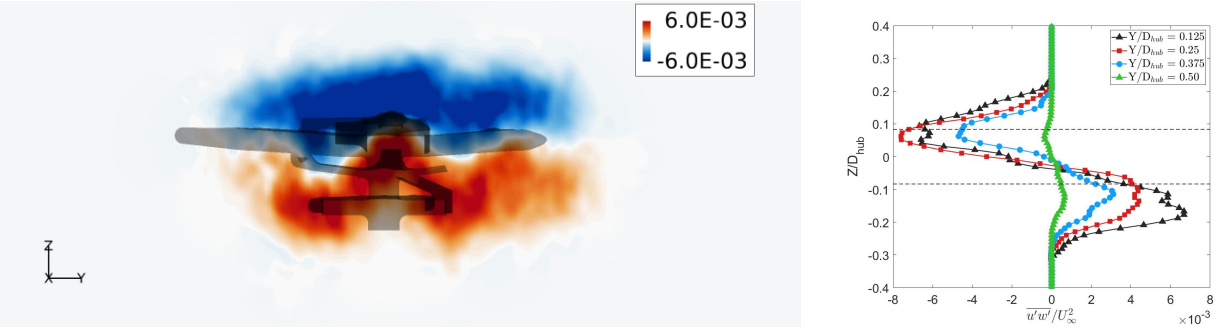
(a) Baseline hub



(b) Defeatured hub

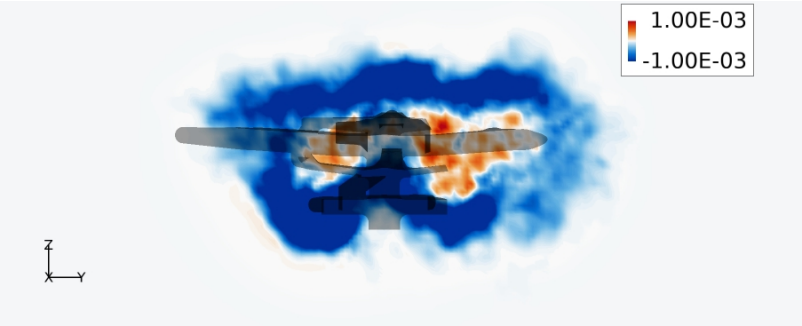


(c) Low Drag hub

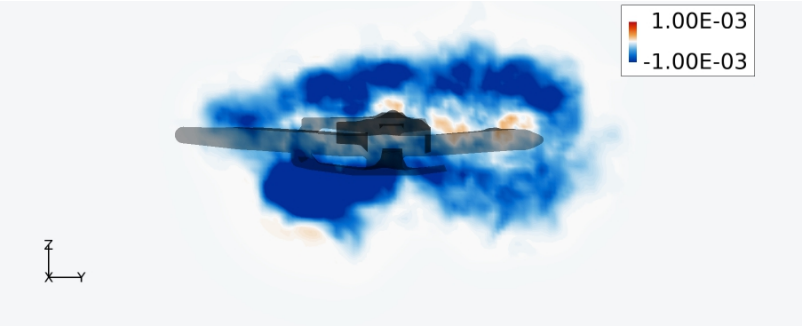


(d) Phase III hub

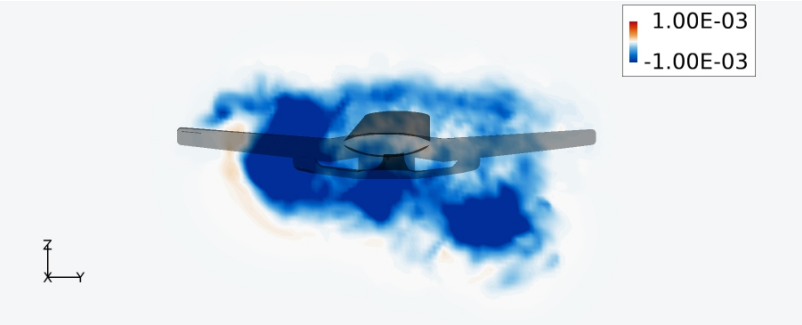
Figure 44: Normalized Reynolds stress $\overline{u'w'}/U_\infty^2$, $x = D_{hub}$



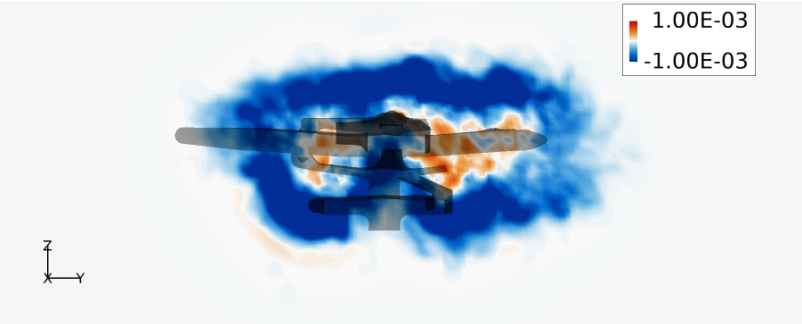
(a) Baseline hub



(b) Defeatured hub

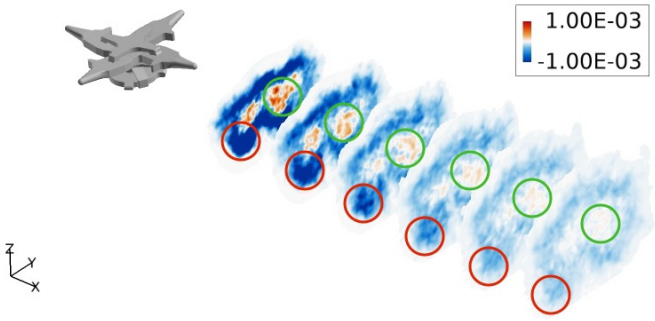


(c) Low Drag hub

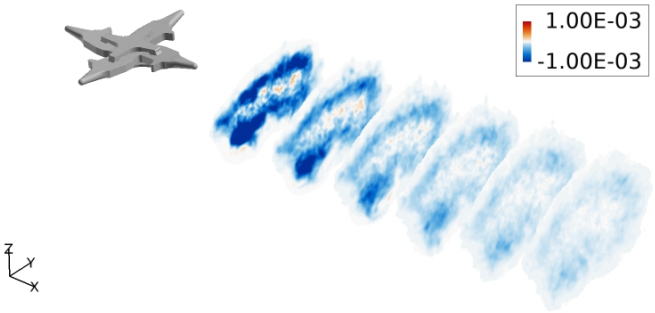


(d) Phase III hub

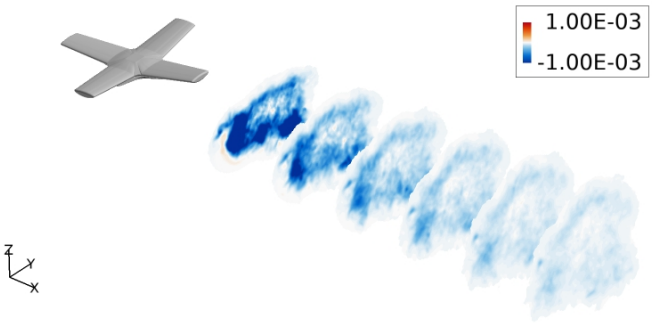
Figure 45: Third order moment $\overline{u'u'u'}/U_\infty^3$, $x = D_{hub}$



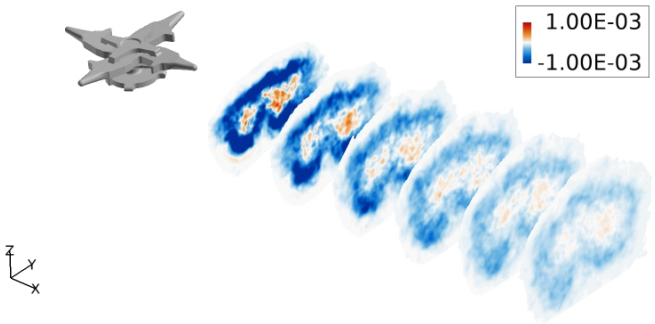
(a) Baseline hub



(b) Defeatured hub

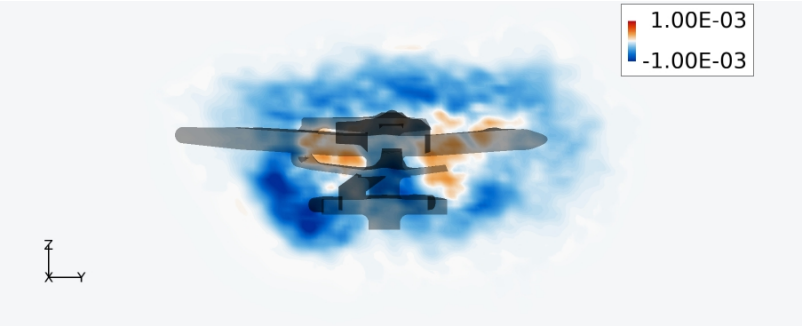


(c) Low Drag hub



(d) Phase III hub

Figure 46: Third order moment $\overline{u'u'u'}/U_\infty^3$, full wake



(a) Baseline hub



(b) Defeatured hub

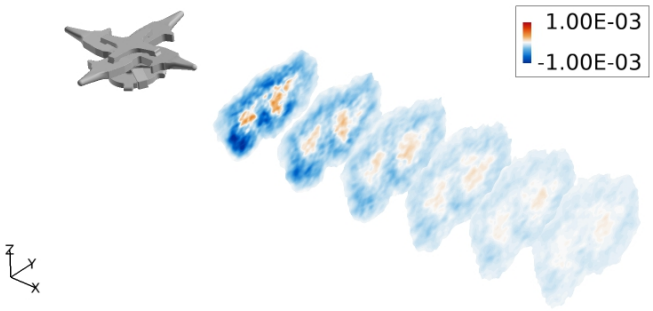


(c) Low Drag hub

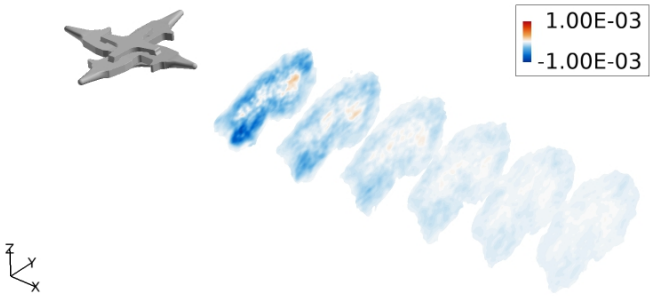


(d) Phase III hub

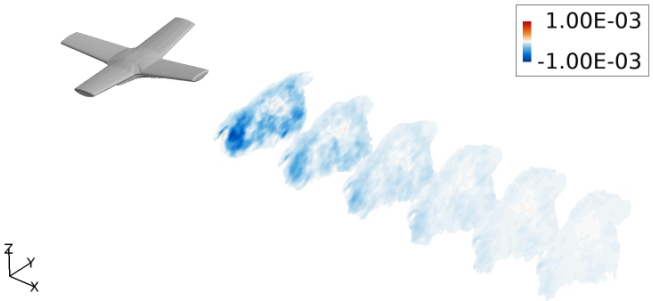
Figure 47: Third order moment $\overline{u'v'v'}/U_\infty^3$, $x = D_{hub}$



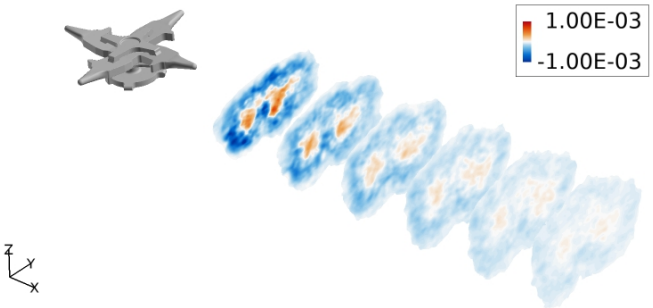
(a) Baseline hub



(b) Defeatured hub

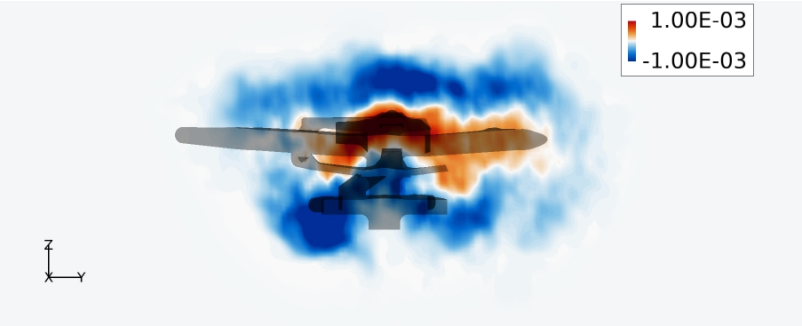


(c) Low Drag hub

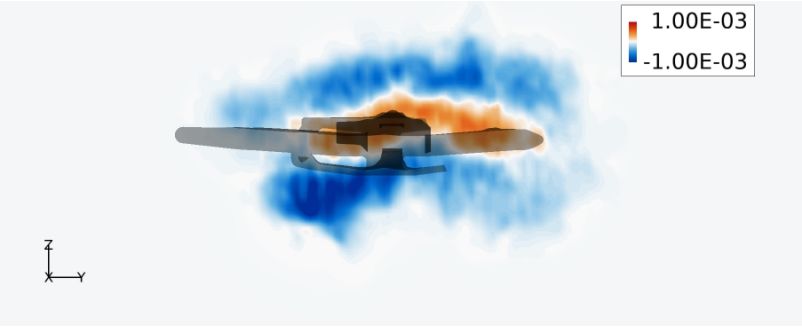


(d) Phase III hub

Figure 48: Third order moment $\overline{u'v'v'}/U_\infty^3$, full wake



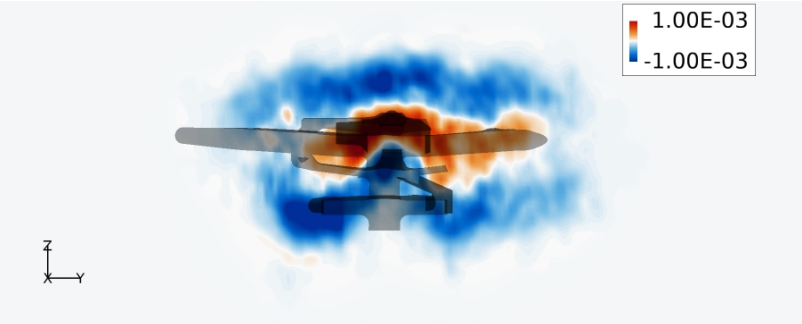
(a) Baseline hub



(b) Defeatured hub

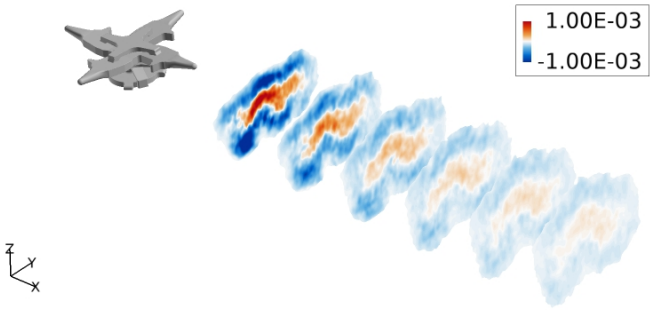


(c) Low Drag hub

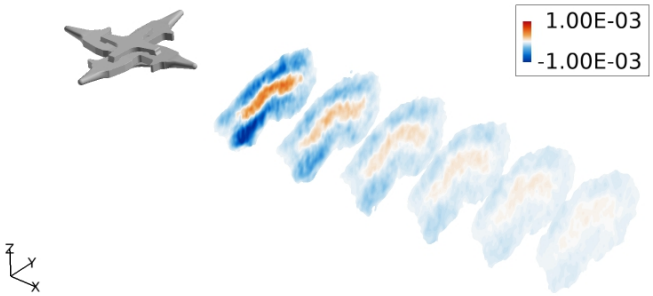


(d) Phase III hub

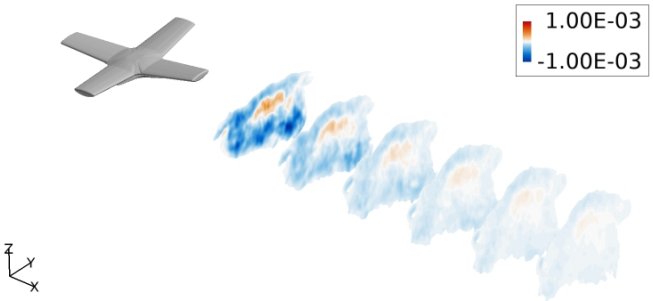
Figure 49: Third order moment $\overline{u'w'w'}/U_\infty^3$, $x = D_{hub}$



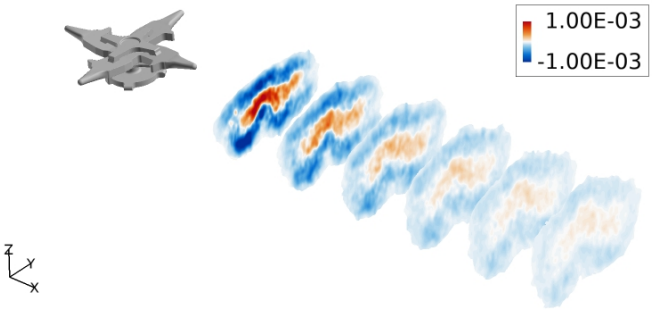
(a) Baseline hub



(b) Defeatured hub



(c) Low Drag hub



(d) Phase III hub

Figure 50: Third order moment $\overline{u'w'w'}/U_\infty^3$, full wake

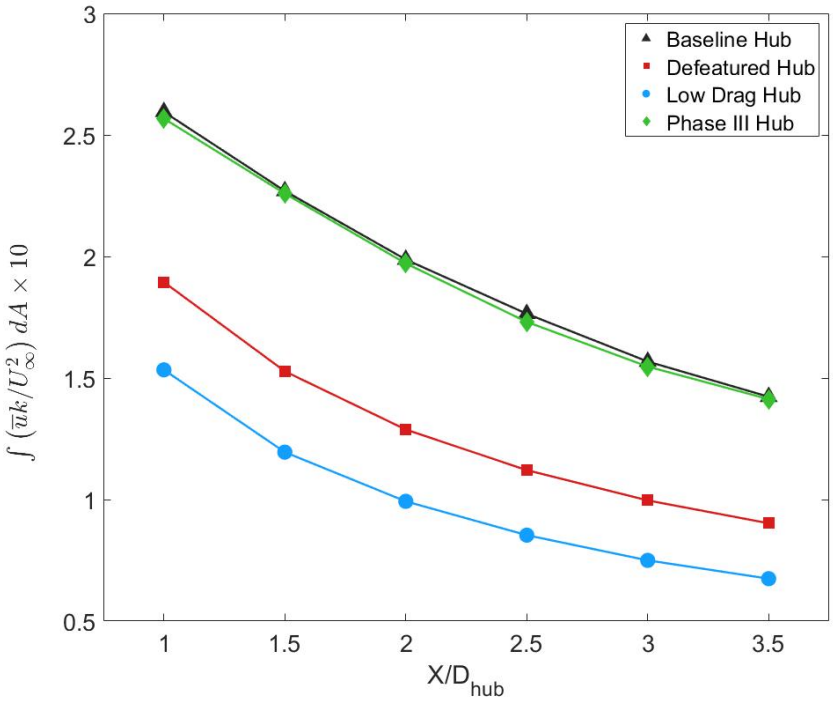


Figure 51: Normalized TKE convective flux through hub wake

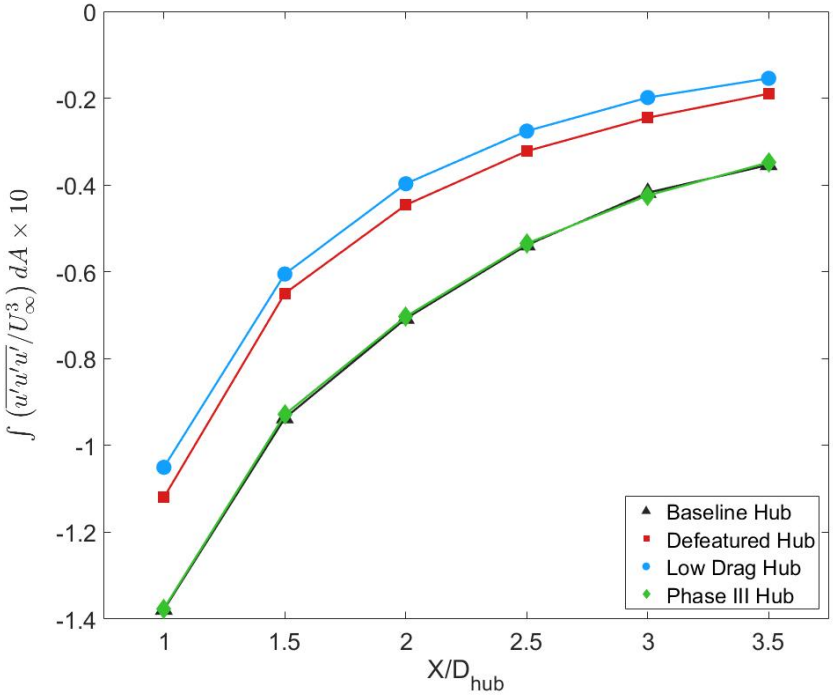


Figure 52: $\overline{u'u'u'}/U_\infty^3$ integrated through the wake

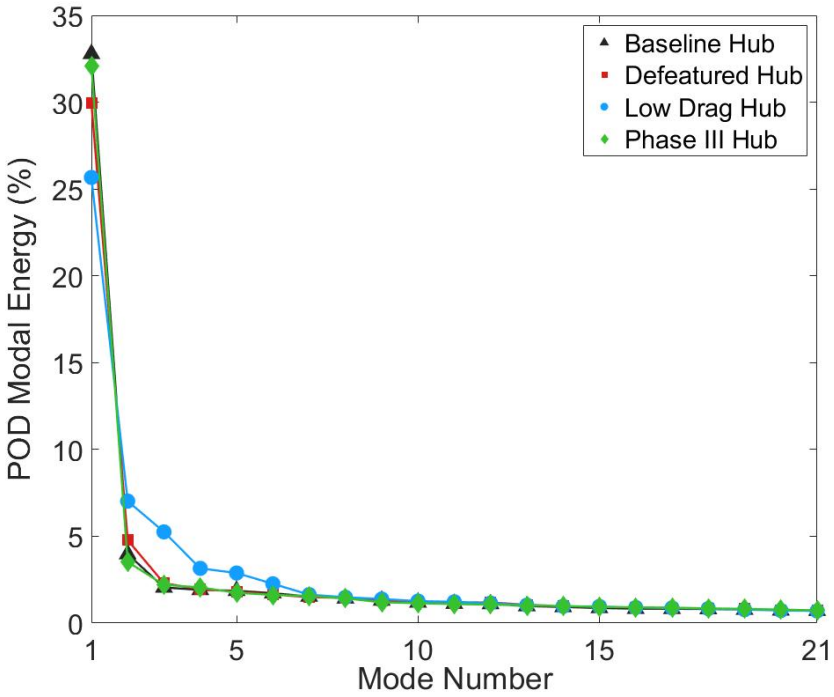


Figure 53: POD modal energy distribution, $x = D_{hub}$

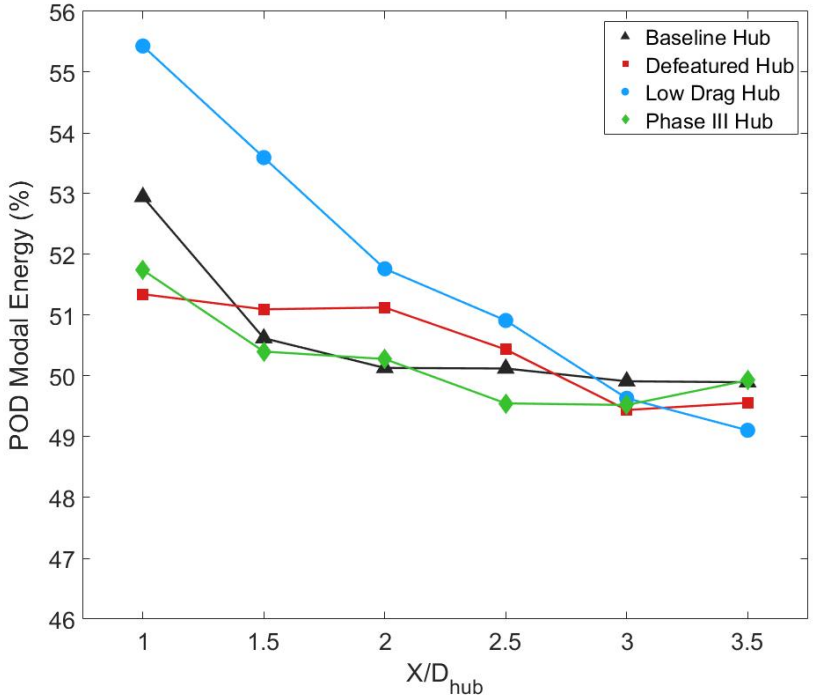
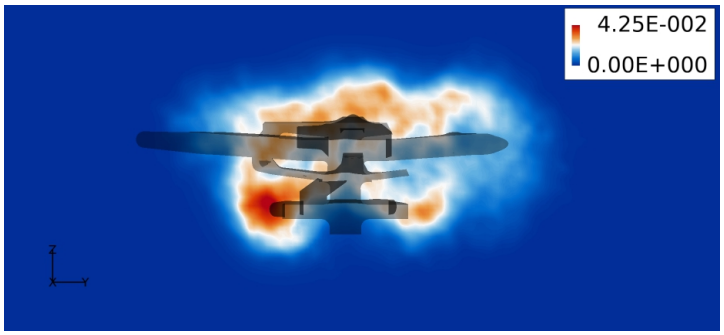
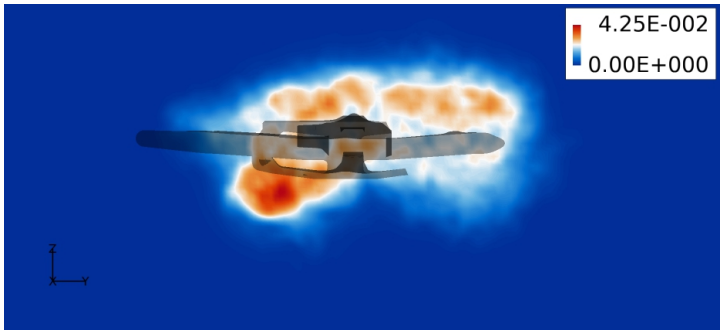


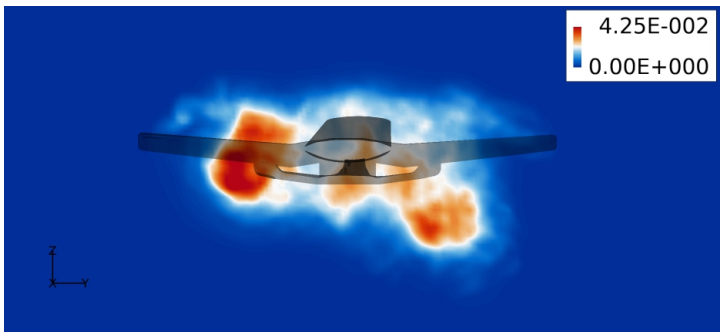
Figure 54: POD modal energy, first 12 modes



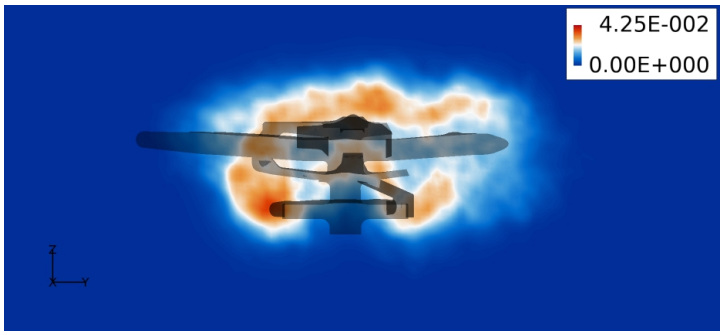
(a) Baseline hub



(b) Defeatured hub

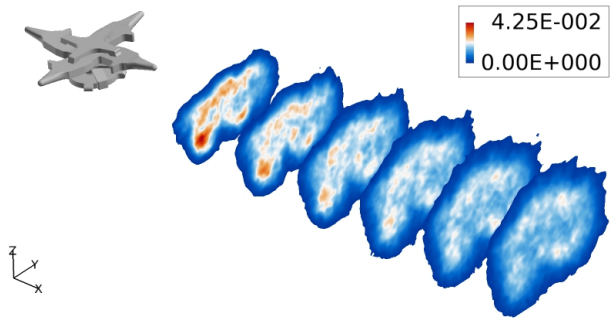


(c) Low Drag hub

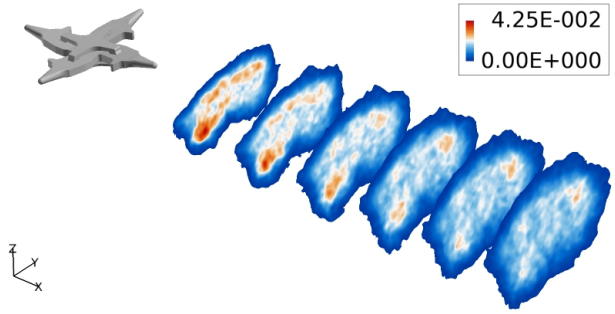


(d) Phase III hub

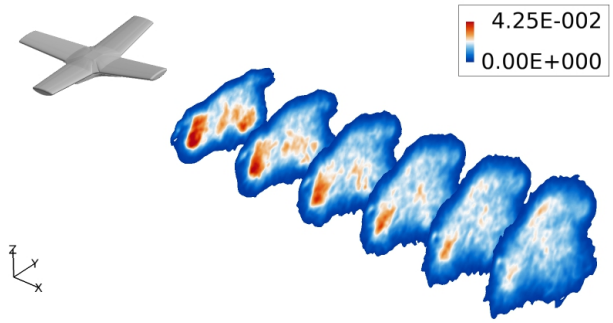
Figure 55: POD of $u'u'$, first mode, $x = D_{hub}$



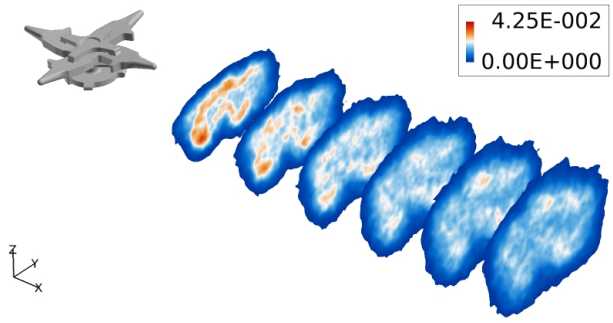
(a) Baseline hub



(b) Defeatured hub



(c) Low Drag hub



(d) Phase III hub

Figure 56: POD of $u'u'$, first mode, full wake

Vita

Forrest Mobley was born in November 1994 in Anchorage, Alaska, to parents Keith Mobley and Beth Koenigsberg. He graduated high school in 2013, then moved to Japan to serve as a missionary for the Church of Jesus Christ of Latter-Day Saints for two years. After his time in Japan, Forrest moved to Prescott, Arizona, to attend Embry-Riddle Aeronautical University and pursue a Bachelor's degree in Aerospace Engineering. Forrest met and married Geena Marsh in December 2016, during his first year at college. Once completing his undergraduate degree, Forrest continued his education at the University of Tennessee Knoxville, graduating with a Master's of Science in Aerospace Engineering in August 2022 under advisor Dr. James Coder. Outside of school, Forrest enjoys reading, backpacking, and cooking.